ELECTRIC FIELD GRADIENT AT ^{181}Ta NUCLEI IN HAFNIUM COORDINATION COMPOUNDS

ELECTRIC FIELD GRADIENT AT ^{181}Ta

NUCLEI IN HAFNIUM COORDINATION COMPOUNDS

by

LEO MICHAEL LOWE, B. Sc.

A Thesis

Submitted to the Faculty of Graduate Studies

In Partial Fulfilment of the Requirements

for the Degree

Doctor of Philosophy

McMaster University

July 1976

DOCTOR OF PHILOSOPHY   McMASTER UNIVERSITY
    (PHYSICS)   Hamilton, Ontario

TITLE: Electric Field Gradient at ^{181}Ta Nuclei
                       in Hafnium Coordination Compounds

AUTHOR: Leo Michael Lowe, B.Sc. (University of Ottawa)

SUPERVISOR: Professor W. V. Prestwich

NUMBER OF PAGES: xi,   151

ACKNOWLEDGEMENTS

ABSTRACT

The quadrupole interaction of ^{181}Ta with the electric field gradient (EFG) at Hf sites in the coordination compounds $(NH_4)_3 HfF_7$, K_3HfF_7 and $Hf(acac)_4$ has been measured by the method of differential perturbed angular correlations.

The heptafluorates which possess identical crystal structures were found to produce vastly different EFG's at the sites of the ^{181}Ta probe nuclei. Over the range from liquid nitrogen to room temperature, the EFG in $(NH_4)_3HfF_7$ was observed to change from a static to a dynamic nature due to the reorienting HfF_7^{3-} ion and the effects of the dynamic NH_4^+ ions. No comparable time-dependent effects were observed in K_3HfF_7 which required a two site static model for the Hf atoms at liquid nitrogen temperature and a one site model, with only a slight dynamic modification, at room temperature. The results were found to be in agreement with other NMR and X-ray studies of these compounds.

The measurement of the EFG at the metal site in $Hf(acac)_4$ yielded a large asymmetry value that is discussed in terms of the crystal structure and type of ligand bonding involved in this octocoordinated complex. Comparison of the results for synthetic and irradiated samples of $Hf(acac)_4$.

gave no indications of radiation produced damage to the crystal structure. Evidence for the existence of two sites with different asymmetry parameters as suggested by a previous study was not found.

A detailed investigation of instrumental effects in perturbed angular correlation measurements was also carried out. This study included the measurement and correction of system nonlinearities and background anomalies in time spectra measurements.

Finally, a precise measurement of the half-life of the 482 keV level in ^{181}Ta was performed using the delayed coincidence method.

TABLE OF CONTENTS

Page

vii

LIST OF FIGURES

x

LIST OF TABLES

CHAPTER I

INTRODUCTION

The pursuit of scientific knowledge by means of research in physics generally leads to the study of a particular field of endeavour such as nuclear or solid-state physics. The problems encountered often lie within a well-defined discipline. There are however, certain fruitful areas of research that are not so restricted in their outlook. One such case is that of perturbed angular correlations (PAC) which combines the points of view of nuclear physics, solid-state physics, atomic physics and chemistry. This is a prime reason why PAC has become a great attraction for many experimentalists. It has become known as a physical method rather than remaining as a limited branch of nuclear physics from which it originated.

The PAC method is based on the measurement of the angular distribution of radiation from nuclei whose spins tend to point in a certain preferred direction. Angular distributions of radiation from free nuclei are dependent only on the nuclear properties of the system and as such, the study of these distributions has become an important tool in nuclear research. Generally, these nuclei are not free but are located in a

1

source or target in which large internal and external magnetic or electric fields may be present. These fields interact with the magnetic or electric moments of the oriented nucleus under study and may change its degree of orientation in the time interval between its initial orientation and the subsequent emission of the nuclear radiation. This change allows one to study the interaction of the nucleus with its surroundings · and therefore can be a valuable aid in chemical and solid-state research.

There are a number of methods available to produce an assembly of nuclei that possess the same average orientation with respect to a particular axis. One way is to place the sample at very low temperature in a region of strong magnetic or electric field thereby producing a net alignment of nuclear spins. Another method uses nuclear reactions that leave the target nucleus in an oriented state because of the conservation of angular momentum of the reaction products. A third method, and the one with which this thesis is concerned, is the selection of nuclei whose spins happen to be in a preferred direction.

The basis of this method can be explained by considering a nucleus that decays through the successive emission of two γ-rays, γ_1 and γ_2 as shown in figure 1.1. Although γ-rays are chosen here, other two-step nuclear processes can be utilized
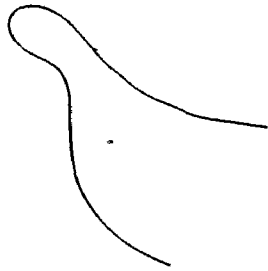
Figure 1.1

Decay of an Excited Nucleus by Successive γ-Ray Emission

γ_1

Θ

γ_2

J_1

I

J_2

L_1

L_2

γ_1

γ_2
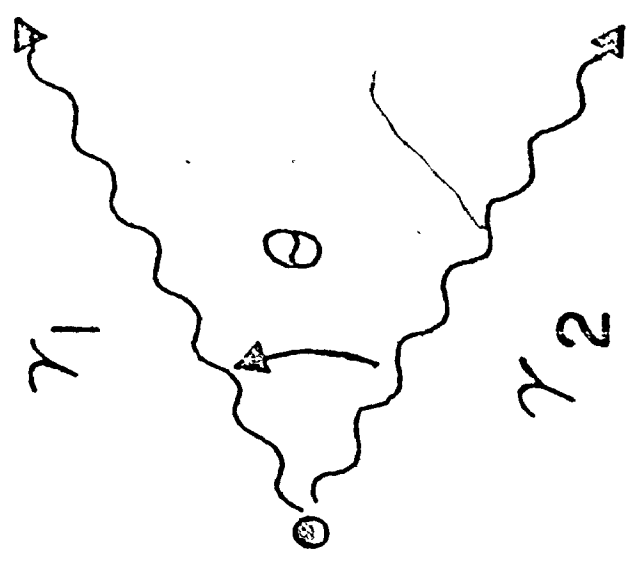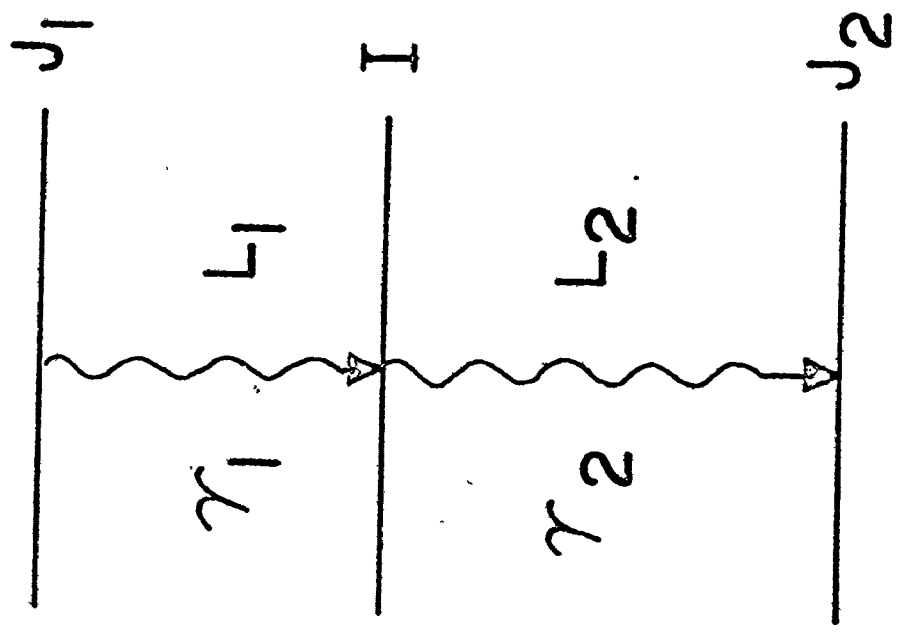
e.g. the scattering of a charged particle followed by
γ emission due to Coulomb excitation. The nuclei are
randomly oriented and γ_1 can be emitted in any direction.
The observation of γ_1 in a fixed direction, however, selects
those nuclei with preferentially aligned spins. The second
radiation γ_2 will then be emitted by nuclei with this prefer-
ential alignment and γ_2 will show an angular dependent coinci-
dence rate $W(0)$ with respect to γ_1. This angular correlation
is dependent only upon the nuclear properties of the cascade
and it provides information about the nuclear levels involved
and the angular momentum carried away by the γ-rays, if the
orientation of the nucleus remains unchanged between the times
of emission of γ_1 and γ_2 i.e. when the nucleus is in the inter-
mediate level I. The measured distribution is known as the
unperturbed angular correlation.

Extranuclear magnetic or electric fields interacting
with the nuclear magnetic dipole or electric quadrupole moments
can cause the nucleus to precess about the field direction
much like a spinning top will precess in a gravitational field.
If the strength of the interaction is sufficiently strong to
cause a significant change in the alignment of the nuclear spin
within the lifetime of the intermediate level, then γ_2 is emitted
from an altered distribution of nuclear spins and the γ_1-γ_2

angular correlation is perturbed. In quantum mechanical language, the interactions cause transitions among the m states of the intermediate level thus changing the m state population distribution and this change is responsible for the perturbation or attenuation of the angular correlation.

A schematic of the apparatus used to measure the angular correlation is shown in figure 1.2. A complete description of the experimental arrangement is given in chapter 3. Detectors 1 and 2 are made to accept only γ_1 and γ_2 respectively when emitted at an angle Θ relative to each other. The detectors respond to all γ_1 and γ_2 radiation but the coincidence analyzer accepts only those pairs γ_1 and γ_2 which are emitted within the resolving time of the coincidence circuit. This ensures that both γ-rays are from the same nucleus. The angular correlation function $W(\Theta)$ is then given by the number of coincidences per unit time as a function of the angle Θ.

The times of emission of γ_1 and γ_2 are not simultaneous but are separated by the exponential decay of the intermediate level of lifetime τ. If the resolving time of the coincidence circuit is small in comparison to τ, the distribution in time intervals between the emissions of γ_1 and γ_2 can also be recorded. The resulting time spectrum $W(\Theta,t)$ is an exponential decay that

Figure 1.2

Schematic of the Experimental Arrangement Used

for Angular Correlation Measurements

COINCIDENCE
ANALYZER

DETECTOR 1

DETECTOR 2

θ

γ_1

γ_2

SOURCE
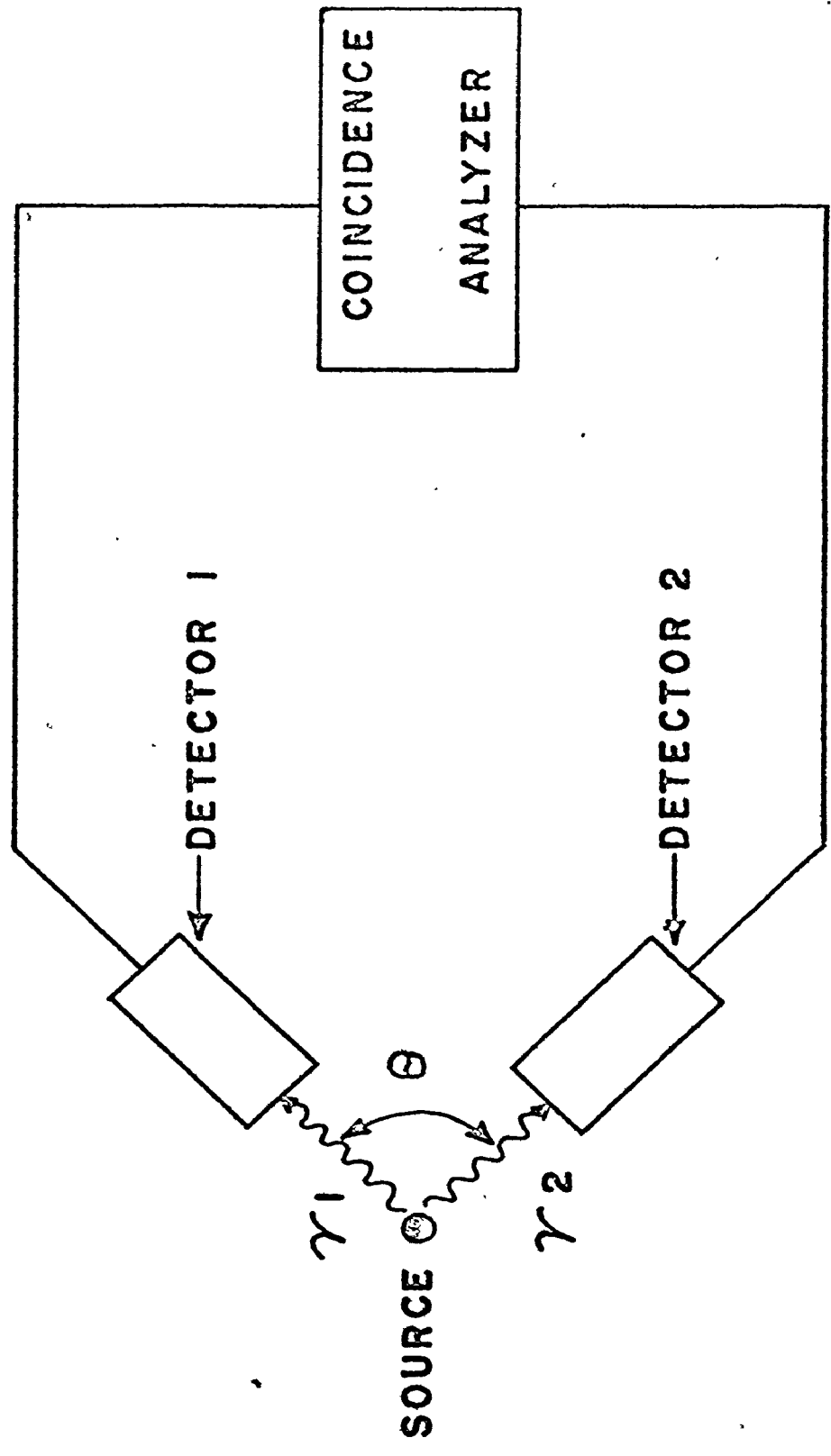
is modulated by the reorientation of the angular corre-
lation pattern due to any extranuclear field interaction.
This is known as a differential perturbed angular corre-
lation (DPAC) measurement. If the resolving time of the
coincidence circuit is much larger than τ, the experiment
is called an integral measurement. DPAC generally yields
information of a more detailed nature than the integral
method. In particular, it is possible with differential
measurements to reach conclusions about the symmetry of
electric field gradients at the nuclear site whereas the
integral correlation method is rather insensitive to asym-
metry effects.

The above description of the method of perturbed
angular correlations is only of an introductory nature. A
further treatment of this subject outlining the theoretical
equations involved is given in chapter 2.

The PAC technique possesses some important advantages
when compared to other experimental methods, such as the
Mossbauer effect, which also uses the nucleus as a probe into
the solid-state or chemical behaviour of matter: the method
can be performed at all temperatures; measurements can be
carried out in liquids and gases as well as solids; it requires
a relatively small amount of active nuclei when compared to

resonance methods; it is not restricted to ground state transitions or low energy γ-rays; it can be used to study directly the time variation of the local environment of the probe nucleus. As a result, PAC applications have become both numerous and diverse. These include the measurement of the "tumbling" times of biologically important molecules in solution (SH70) which is related to their effective length and hence their chemical constitution, the study of protein structure (BA74) and in vivo experiments on the chemical behaviour of certain compounds in mice (ME72). Radiation damage measurement (VA69) is another important application. PAC has also been used in the elucidation of solid-state physico-chemical phenomena such as interconversion among possible conformational isomers (BO72) and electronic bonding symmetries in organic complexes (RA75). The latter two applications are related to the research area of the present work.

This thesis is concerned in part with the electric quadrupole interaction of ^{181}Ta in the fluorine compounds $(NH_4)_3HfF_7$ and K_3HfF_7. DPAC studies of these compounds are particularly intriguing because they contain the unusual ion HfF_7^{3-}. Original models were based on a structure consisting of ZrF_6^{2-} and F^- ions (HA24) from studies of the analogous compound $(NH_4)_3ZrF_7$. A later study (HA38) on this same compound

and K_3ZrF_7 proposed the model containing the ZrF_7^{3-} ion in a disordered structure that allowed several possible orientations of the ion. Some disorder of the zirconium and nitrogen atoms was also postulated. This disorder made a definitive study of these compounds difficult to achieve. More recent X-ray analysis (HU70) on $(NH_4)_3ZrF_7$ disagreed with the structure proposed earlier. Nuclear magnetic resonance experiments (PI67) have indicated that the ZrF_7^{3-} and NH_4^+ ions are dynamically distorted and reorienting. This dynamic or time dependent relaxation effect has been studied by Andrade et al. (AN70) and Gerdau et al. (GE73) who, during the course of this work, performed DPAC measurements of the quadrupole interaction of ^{181}Ta in $(NH_4)_3HfF_7$. Both papers attributed the relaxation to the "jumping about" of the seventh fluorine atom above the trianglular faces of the HfF_6^{2-} octahedra although only Gerdau saw definite indications of a static interaction at low temperatures.

In the present work, DPAC experiments on $(NH_4)_3HfF_7$ were performed at various temperatures and compared to the previous results. In addition, a DPAC study of the similar compound K_3HfF_7 was carried out in the hope that a comparative study would shed more light on these compounds. Any time dependent and temperature sensitive variation of the Hf

environment in this compound could not be attributed to NH_4^+ ion dynamics and any manifestation of HfF_7^{3-} ion effects including reorientation or structure changes could be separately observed.

A second concern of this thesis is the study of the electric field gradient at the metal site in hafnium acetylacetonate, $Hf(acac)_4$. Early interest in this compound was initiated by the possibility of using it as a probe to study the orientation effects of the layered structure of a liquid crystal. It had been demonstrated (UH70) in a Mossbauer investigation that a molecular probe could yield structure information for both the solute molecules and liquid-crystalline solvent. Because of the orientation effects, DPAC is a logical, complementary technique in this research area. However, prior to such an investigation, a more complete knowledge of the $Hf(acac)_4$ molecule itself was required and DPAC studies of the quadrupole interaction of ^{181}Ta in $Hf(acac)_4$ were performed. As shall be seen in a later chapter, the data analysis of this compound is related to that of K_3HfF_7. Both compounds are concerned with the possibility that the Hf atom can be situated within two different chemical environments. Earlier DPAC data on $Hf(acac)_4$ (BE69) had indicated this two site approach, with the probability of occurrence of each site being dependent on

the radiation history of the sample. The ability of the data reduction methods used in this thesis to distinguish between the one and two site models is important for a proper interpretation of the experimental results. The present DPAC study of $Hf(acac)_4$, which is significantly different from the previous results, is analyzed in terms of the symmetry nature of the electric field gradient at the Hf site and is shown to be consistent with an earlier structure determination done by X-ray analysis (SI63).

Another aspect of this thesis is concerned with instrumental effects involved in DPAC measurements and the corresponding data manipulation that is required to deal with these effects. These include time and angular resolution calculations, nonlinearities in the measuring system and background anomalies in time-interval distributions. A basic knowledge of these instrumental limitations is a requisite for proper DPAC research using the present experimental arrangement.

Finally, included in the data reduction section of this work is a precise measurement of the half-life of the 482 keV level of ^{181}Ta. The half-life of this level, which is the intermediate level of the $\gamma-\gamma$ cascade used in the DPAC studies, can be calculated from the DPAC data and in fact serves as an indicator of correct data reduction. During the course of

this work, the half-life values derived from the DPAC data
were found to be consistently lower than the most recently
published result. In the measurement of the half-life,
careful attention was directed towards system non-linearities
and an accurate method of time calibration in order to obtain
a more precise value.

CHAPTER 2

The Theory of γ-γ Angular Correlations

The general theory of the angular distribution of nuclear radiation has been extensively studied and reviewed; for example see (FR68). The theory is far-ranging and is usually divided into subsections centred on the type of radiation observed (α,β,γ), on the properties that are singled out by the experiment (direction, polarization), and on the extranuclear fields acting on the nucleus (magnetic or electric). This chapter presents the fundamental equations of the theory on which the calculations of the present study are based. As such, they deal with the angular correlation of γ-rays from a γ-γ cascade and the perturbation of this correlation by the interaction of the extranuclear electric field gradient with the nuclear quadrupole moment.

1. The Unperturbed Angular Correlation

The angular variation of the intensity of a cascade pair of γ-rays is given by

$$W(\theta) = 1 + \sum_{\substack{k=2 \\ k \text{ even}}}^{k_{max}} A_k P_k (\cos \theta) \qquad (2.1)$$

13

In this expression, Θ is the angle between the two γ-rays, $P_k(\cos \Theta)$ is the Legendre polynomial of order k and the A_k are parameters depending on the level spin sequence and transition multipolarities. The sum limit kmax is determined by kmax=minimum $(2J, 2L_1, 2L_2)$ where J is the spin of the intermediate level and L_1, L_2 are the multipolarities of the γ-rays; kmax=4 for the case of the 482 keV level of ^{181}Ta. This is always the maximum for practical experimental purposes and, as shall be seen in a later chapter, terms up to only k=2 are sufficient in the present study. Time differential measurements also record the time of emission of γ_2 with respect to γ_1 and equation 2.1 becomes

$$W(\Theta,t) = \left[1 + \sum_{\substack{k=2 \\ k \text{ even}}}^{kmax} A_k P_k (\cos \Theta)\right] \exp (-t/\tau) \qquad (2.2)$$

where τ is the lifetime of the intermediate state.

2. The Perturbed Angular Correlation

The angular correlation of the γ-γ cascade will be altered if the orientation of the nucleus is disturbed while the nucleus is in the intermediate state. This perturbation is a result of the coupling of the electromagnetic moments of the nucleus and extranuclear electromagnetic fields. These

fields may be static or time dependent and of electric or magnetic origin. The γ-γ correlation is changed in the time interval between the emission of the first and second γ-rays and equation 2.2 must now contain functions $G_k(t)$ describing the attenuation of the angular correlation coefficients A_k,

$$W(0,t) = \left[1 + \sum_k A_k G_k(t) P_k(\cos 0)\right] \exp(-t/\tau) \qquad (2.3)$$

The $G_k(t)$ contain all the physical information about the perturbation mechanisms. Much theoretical work is concerned with the derivation of $G_k(t)$ for various types of interactions. This work is concerned with electric field interactions.

A. Static Interactions

For the case of a fixed electrostatic crystalline field gradient interacting with the electric quadrupole moment Q of a nuclear state of spin I, the interaction Hamiltonian may be represented as (GF69)

$$H = \left[e^2 Q V_{zz}/4I(2I-1)\right] \left[3 I_z^2 - I(I+1) + \frac{1}{2} \eta (I_+^2 + I_-^2)\right] \quad (2.4)$$

where $\eta = \dfrac{V_{xx} - V_{yy}}{V_{zz}}$ \qquad (2.5)

and V_{zz} is a component of the electric field gradient such

that $V_{zz} = \dfrac{d^2V}{dz^2}$. The parameter η is a measure of the asymmetry of the field gradient and is identical to zero for axially symmetric field gradients. The electric field gradients are not independent but are related by Laplace's equation

$$V_{xx} + V_{yy} + V_{zz} = 0 \qquad (2.6)$$

The principal axes are chosen such that

$$|V_{zz}| \geq |V_{yy}| \geq |V_{xx}|$$

and thus η is restricted to $0 \leq \eta \leq 1$. The electric field gradient is then characterised by its greatest component V_{zz} and the asymmetry parameter η.

The quadrupole interaction causes a hyperfine splitting of the nuclear energy levels. The energy splittings are not uniform and the states are twofold degenerate, i.e. the magnetic quantum numbers + m and − m give the same energy. For odd 2I, there are $\frac{1}{2}(2I+1)$ levels and transitions between these levels occur with characteristic frequencies ω_n.

For the case of axial symmetry, $\eta=0$, the simplified interaction Hamiltonian yields the energies

$$E_m = [3m^2 - I(I+1)]\hbar\omega_Q$$

where ω_Q is the quadrupole interaction frequency defined by

$$\omega_Q = - \frac{eQV_{ZZ}}{4I(2I-1)\hbar} \qquad (2.7)$$

The smallest frequency ω_1 is related to ω_Q by

$$\omega_1 = 3\, \omega_Q \quad \text{for even } 2I$$
$$= 6\, \omega_Q \quad \text{for odd } 2I$$

and the remaining frequencies are harmonics of ω_1. For a polycrystalline sample, the interactions are averaged over all directions and the perturbation function $G_k(t)$ is given by

$$G_k(t) = \sum_{n=0}^{n_{max}} S_{kn} \cos(n\omega_1 t) \qquad (2.8)$$

The spin dependent S_{kn} have been calculated for the $\eta=0$ case by Alder et al. (AL64). The spin dependent $n_{max} = 3$ for $I = 5/2$. An example of $G_2(t)$ for $I = 5/2$ and $\eta=0$ is shown in figure 2.1.

The perturbation function is thus a sum of periodic functions and the static interaction cannot destroy the angular correlation. If the field strength is constant in time the time-integrated attenuation function is

$$G_k(\infty) = \sum_n S_{kn} \frac{1}{1+(n\omega_1\tau)^2}$$

where τ is the lifetime of the intermediate level. Even for an infinitely strong interaction, $G_k(\infty)$ never goes below the so-called "hard core" value:

$$\lim_{\omega_1 \to \infty} G_k(\infty) = S_{ko} \qquad (2.9)$$

Figure 2.1

The Perturbation Function $G_2(t)$ for $I=5/2$ and

Various Values of the Asymmetry Parameter η

Axis labels: $G_2(t)$ (vertical), $\omega_1 t/\pi$ (horizontal)

$\eta = 0.00$

$\eta = 0.45$

$\eta = 1.00$
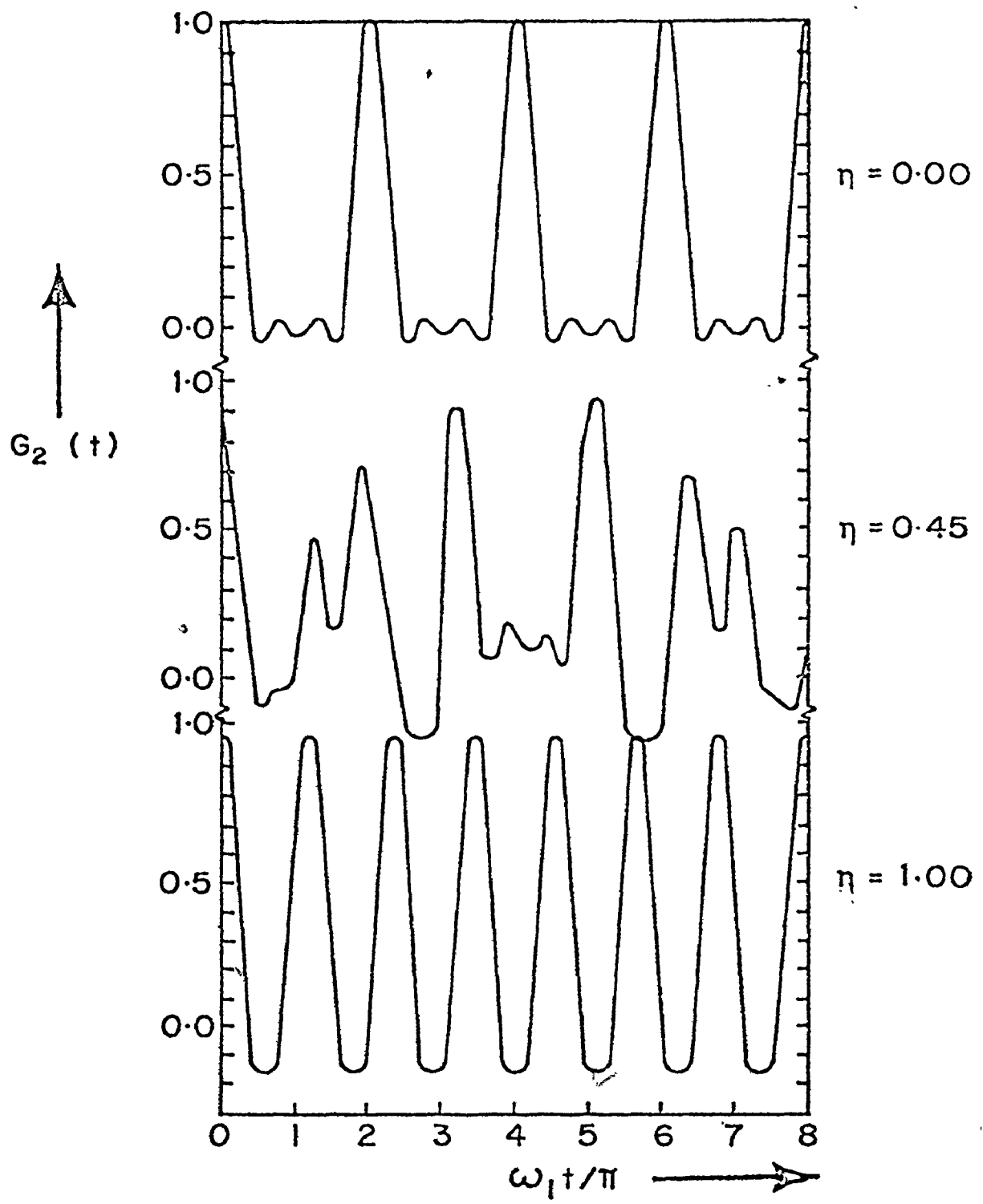
The calculation of the attentuation coefficients for non-axially symmetric fields ($\eta \neq 0$) is more complicated. The eigenfunctions and eigenvalues of the interaction Hamiltonian must be determined for different values of ω_Q and η. The interaction frequencies are no longer multiples of ω_Q. This case has been treated by Matthias et al. (MA62,MA63) and also numerically by Alder et al. (AL64) who calculated the a_{kn} coefficients of the perturbation function

$$G_k(t) = a_{ko} + \sum_{n=1} a_{kn} \cos (\omega_n t) \qquad (2.10)$$

Figure 2.1 shows the results for $G_2(t)$ for $I=5/2$ and various values of η. The dependence of $G_2(t)$ on η is obvious.

Beraud et al. (BE69) have considered the quadrupole interaction for the $I=5/2$ case. They determined that the eigenvalues of the interaction Hamiltonian are given by the solutions of the equation

$$W^3 - 28\ W(\eta^2+3) + 160\ (\eta^2-1)=0 \qquad (2.11)$$

where W is in units of $\hbar \omega_Q$. The solutions of this cubic equation are (GE69)

$$E_{\pm 5/2} = 2\alpha\hbar\omega_Q \cos (\tfrac{1}{3} \arccos \beta) \qquad (2.12)$$

$$E_{\pm 3/2} = -2\alpha\hbar\omega_Q \cos (\tfrac{1}{3} (\pi + \arccos \beta))$$

$$E_{\pm 1/2} = -2\alpha\hbar\omega_Q \cos (\tfrac{1}{3} (\pi - \arccos \beta))$$

where $\alpha = \sqrt{\frac{28}{3}} (3+\eta^2)$ and $\beta = \frac{80(1-\eta^2)}{\alpha^3}$

The energy level splittings are shown in figure 2.2. The frequencies ω_n of equation 2.10 are the differences in these energy levels divided by $\hbar$. Using equation 2.11 gives

$$\omega_1 = 2\sqrt{3}\ \omega_Q \sin\ (\tfrac{1}{3}\ \arccos\ \beta) \qquad\qquad (2.13)$$

$$\omega_2 = \alpha\ \omega_Q (3 \cos\ (\tfrac{1}{3}\ \arccos\ \beta)\ -\ \sqrt{3} \sin\ (\tfrac{1}{3}\ \arccos\ \beta))$$

$$\omega_3 = \omega_1\ +\ \omega_2$$

It can be seen that the ω_n are determined solely by ω_Q or ω_1 and η.

Beraud et al. (BE69) have also tabulated the amplitude coefficients a_{2n} of equation 2.10 for the case of I=5/2 and various values of η. Thus for I=5/2, the exact form of $G_2(t)$ can be calculated by specifying the two parameters ω_1 and η and using equations 2.10 and 2.13. A measurement of $G_2(t)$ is then a determination of the crystal structure characteristics η and V_{zz}.

It should be noted that the chemical environment of a nucleus in a solid need not consist of only one type of structure. This is possible because the energy differences between idealized geometries for a particular compound may be small and

Figure 2.2

The Quadrupole Splitting of a $5/2$ Level

as a Function of η
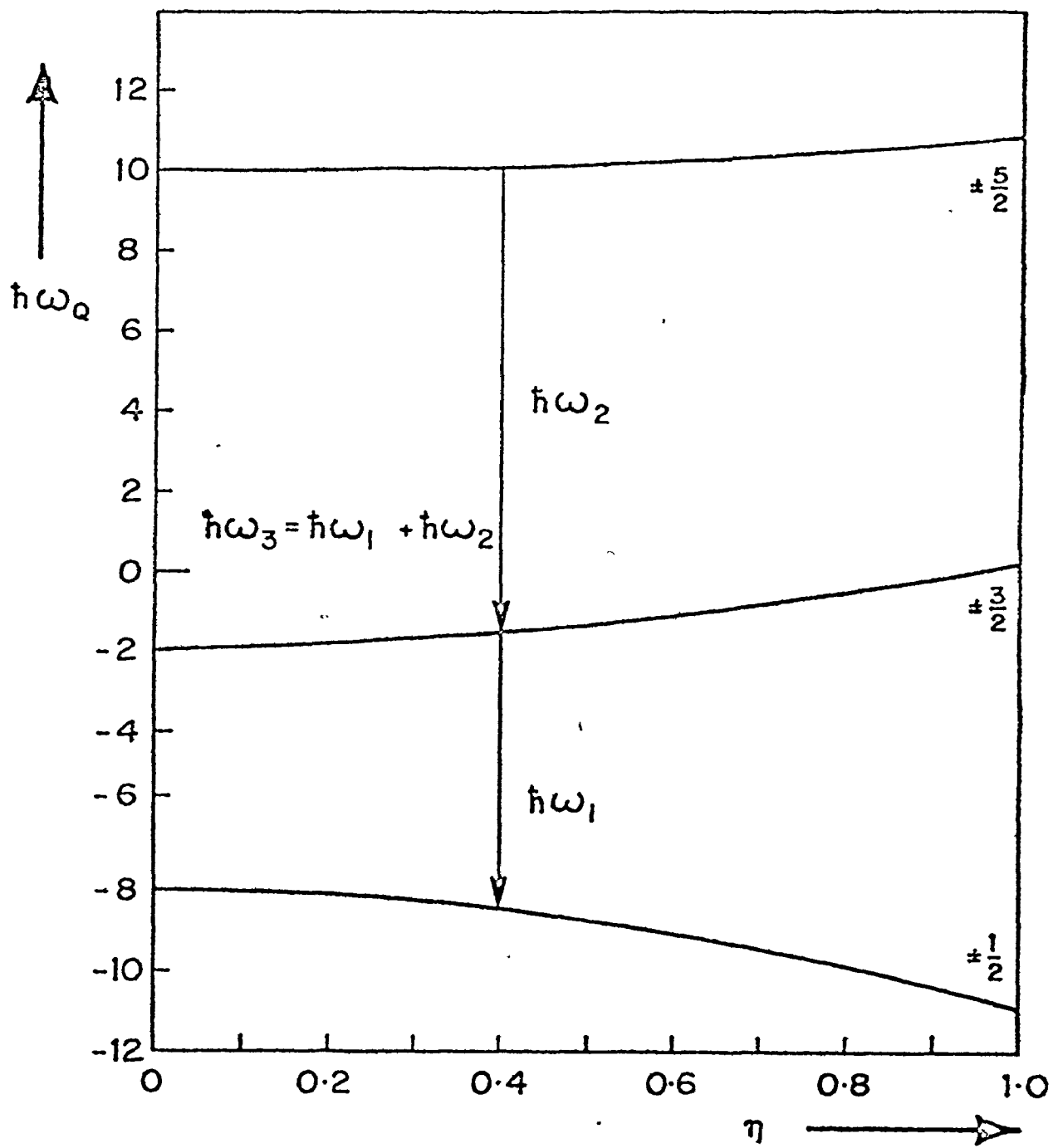
only slight distortions are required to interconvert these
structures (HO63). There is evidence from DPAC measurements
(BO72) that some compounds exhibit two sites for the probe
nucleus, each with separate values of η and ω_Q. In such
cases, the perturbation function is of the form

$$G_k(t) = p\, S_1 + (1-p)\, S_2 \qquad (2.14)$$

where S_1, S_2 represent the perturbation functions for sites
1 and 2 (equation 2.10) and p is the population probability
of site 1. If thermal interconversion of the site structures
is possible, then p will be temperature dependent.

So far in the discussion of DPAC it has been assumed
that the electric field gradient (FFG) at the site of the
perturbed nucleus has some well defined magnitude. In reality,
however, there exist many lattice imperfections due to impur-
ity atoms, vacancies or radiation damage that cause a change in
the atomic environment and thus alter the EFG sensed by the
decaying nucleus. This effect was first mathematically
treated by Matthias (MA63) who assigned a functional distribu-
tion to the interaction frequencies and calculated the new form
of the perturbation function: if the frequency distribution
centred about ω_o is given by $P(\omega - \omega_o)$, then the new perturbation
function is

$$\overline{G_k(\omega_o t)} = \frac{\int P(\omega - \omega_o)\, G_k(\omega t)\, d\omega}{\int P(\omega - \omega_o)\, d\omega}$$

where $G_k(\omega t)$ is the original perturbation function (equation 2.10). If a Gaussian distribution is assumed, then

$$\overline{G_k(\omega t)} = a_{ko} + \sum_n a_{kn} \exp\left[-\frac{1}{2}(\delta_n \omega_n t)^2\right]\cos \omega_n t \qquad (2.15)$$

It is common practice to take $\delta_n = \delta$ for all n. Table 2.1 summarizes the attenuation coefficients resulting from different types of frequency distributions. The effect of a Gaussian distribution on $G_2(\omega t)$ is shown 'in figure 2.3. The frequency distribution tends to smear out the time pattern of the attenuation coefficients.

This procedure is of course only a model calculation and to this author there is no known rigid physical reason why the interaction frequencies should have any of the functional distributions of Table 2.1. The effect of these distributions is mathematically easy to calculate. It is known, however, that this concept does permit a better fit to the experimental attenuation coefficients and the distribution width parameter δ is correlated with possible crystal lattice irregularities.

EFG distributions affect the calculation of EFG parameters such as η and ω_Q as determined from DPAC data. Results of such calculations are given in the data analysis section of this thesis.

TABLE 2.1

Attentuation Coefficients for a Distribution of Interaction Frequencies

$P(\omega-\omega_0)$	$G_k(\omega t)$ *
Gaussian $= \exp\left[-(\omega-\omega_0)^2/2\lambda^2\right]$	$a_{ko} + \sum_n a_{kn} \exp\left[-(\delta\omega_n t)^2/2\right] \cos \omega_n t$
Lorentzian $= \lambda/\left[\lambda^2 + (\omega-\omega_0)^2\right]$	$a_{ko} + \sum_n a_{kn} \exp\left[-\delta\omega_n t\right] \cos \omega_n t$
Square $= \dfrac{1}{\lambda}$ for $\omega_0 - \lambda \leq \omega \leq \omega_0 + \lambda$	$a_{ko} + \sum_n a_{kn} \dfrac{\sin\left[\delta\omega_n t\right]}{\delta\omega_n t} \cos \omega_n t$

* $\delta = \lambda/\omega_n$

Figure 2.3

The Effect on $G_2(t)$ of a Gaussian Interaction

Frequency Distribution of Varying Width δ
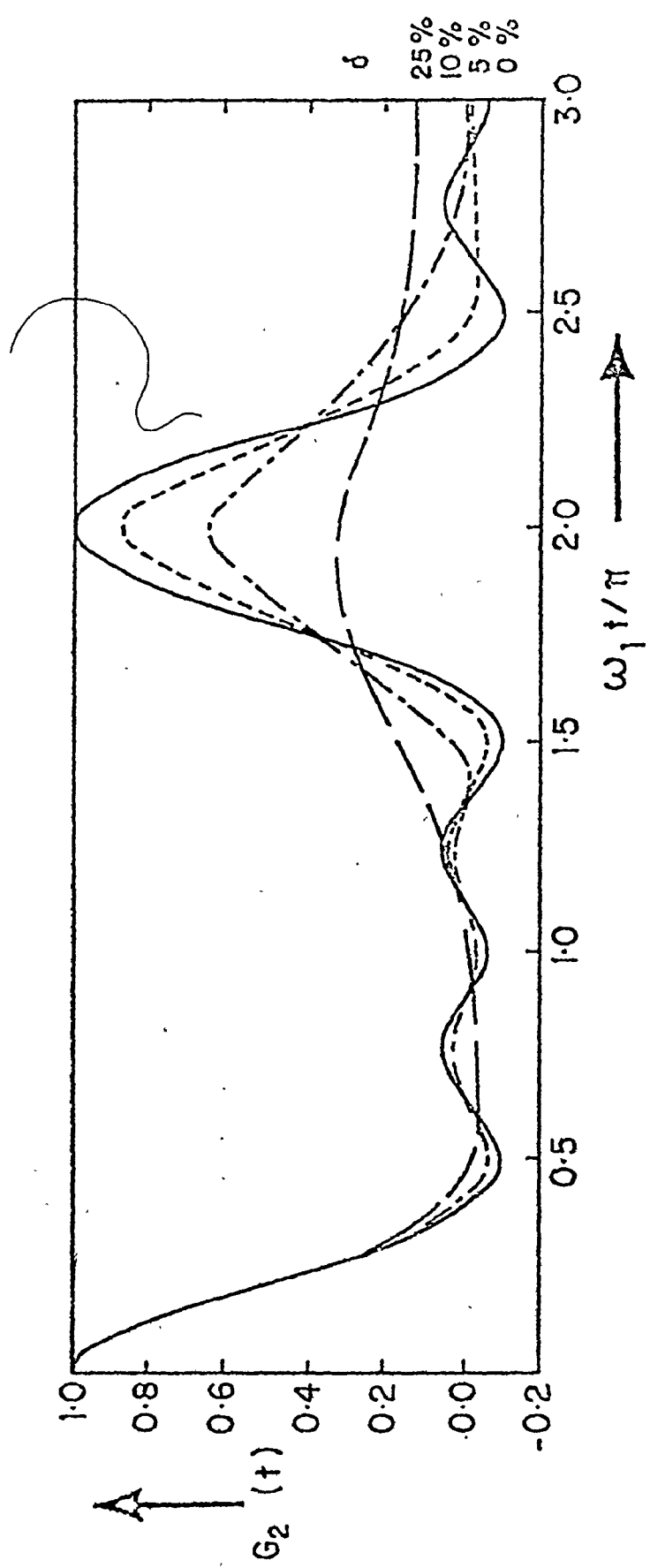
B. Time-dependent Interactions

When the extranuclear fields acting on the nucleus are time-dependent, the solution of the Hamiltonian governing the system cannot in general be written down in closed form. However, there are a number of theories that have been developed for some special cases.

The time dependence of the fields may be due, for instance, to ions and molecules in a liquid source travelling past the nucleus in a random fashion or to rapid conformational changes in the crystalline environment of the nucleus when in a solid. Eventually, the angular correlation measured in a PAC experiment disappears. This is because the random interactions cause transitions among the different m-states of the intermediate nuclear level until they are equally populated and the directional correlation becomes isotropic. This is in contrast to static interactions in polycrystalline sources in which the time-integrated correlation is never reduced below the hard core value (equation 2.9).

The time interval τ_c separating two interactions between the external field and the quadrupole moment is called the correlation time. The case of correlation times that are short relative to the lifetime τ of the intermediate nuclear

level and of small perturbing fields, $\omega_Q \tau_c \ll 1$, has been treated by Abragam and Pound (AB53). They showed that

$$G_k(t) = \exp(-\lambda_k t) \qquad (2.16)$$

where the relaxation parameter is related to the correlation time by

$$\lambda_k = \frac{3}{5} \tau_c \omega_Q^2 k(k+1) \left[4I(I+1) - k(k+1)-1\right] \qquad (2.17)$$

and the time integrated attenuation coefficient is

$$\overline{G_k} = \frac{1}{1+\lambda_k \tau} \qquad (2.18)$$

Many experiments on liquid sources have demonstrated the validity of this theory.

This theory has been generalized (DI62) to include strong perturbations with the result that

$$G_k(t) = \sum_{i=2}^{i\,max} \varepsilon_i \exp(-\lambda_i t) \qquad (2.19)$$

and
$$\sum_{i=2}^{i\,max} \varepsilon_i = 1$$

The parameters ε_i, λ_i must be experimentally determined. Possible evidence for such a multiexponential decay is ambiguous.

The limit of long correlation times that might for example exist for slowly rotating large molecules in solution

has been solved explicitly (MA72). The calculations show that

$$G_k(t) = G_k^O(t)\exp(-t/t_k) \qquad\qquad (2.20)$$

where $G_k^O(t)$ is the static perturbation function and t_k is related to the rotational diffusion constant of the molecule containing the active nucleus. This exponential attenuation is difficult to separate experimentally from the similar effects of a static interaction involving a distribution of frequencies.

Other theories for special cases have been solved for arbitrary correlation time. The work of Gabriel (GA69) is good for all τ_c but assumes small perturbations. The results of Blume (BL71) are also good for all τ_c and are based on a simplifying random interaction assumption: there is no correlation between the orientation of the perturbing field before and after an interaction. The end result is an expression for the Laplace transform of the perturbation function

$$\widetilde{G}_k(p) = \frac{\widetilde{G}_k^O(p+\lambda)}{1-\lambda\widetilde{G}_k^O(p+\lambda)} \qquad\qquad (2.21)$$

$\widetilde{G}_k^O(p)$ is the Laplace transform of the static perturbation function $G_k^O(t)$ and $\lambda=1/\tau_c$ is the relaxation parameter.

This expression which is amenable to numerical calculation reduces to the static case for long τ_c and to unity for short τ_c. The Abragam - Pound results also follow in a suitable limit.

Identical results to that of Blume have been obtained by Lynden-Bell (LY71) who calculated the effect of reorientation of the nuclear spin by molecular motion and the resulting time-dependence of the angular correlation. Although it has been suggested that both theories give a different rate of decay for $G_k(t)$ (WI73), both in fact derive the mathematically identical equation 2.21 and thus must produce the same results (GE75).

Some experimental data on relaxation phenomena in a solid has been fitted by assuming a temperature-dependent mixture of static and time-dependent perturbations (VA73). The effect ranges from a complete static perturbation at low temperatures to pure exponential relaxation at high temperatures.

CHAPTER 3

The Experimental System

1. The Detection Apparatus

The detection apparatus consisted of NaI scintillation detectors and the associated photomultiplier (PM) tubes and bases. Sodium iodide was chosen because of its suitable combination of time and energy resolution and high detection efficiency. Plastic scintillators have inherently better time resolution because of a scintillation decay time of about 2 ns as compared to 250 ns for NaI. However, the predominant γ-ray interaction in plastic is the Compton effect. The energy spectrum of a γ-ray acquired using a plastic detector is then a broad Compton continuum rather than a photopeak indicating full γ-ray energy deposition in the detector via the photoelectric effect as in NaI and the resultant energy resolution is poor. Sufficient energy resolution was necessary to resolve the 482 keV γ-ray of the ^{181}Ta source (figure 5.1) from the 346 keV γ-ray which would produce a large prompt peak in the time spectrum.

The size of the detectors was determined by choosing between the mutually contradictory aims of high detection efficiency which requires large detectors and good time

resolution. Boulter (BO71) has experimentally shown

that even at a low energy such as 133 keV it is important

to use as small a NaI detector as possible in order to

minimize the time resolution. This effect is due to the

number of internal random reflections of the scintillation

photons that occur before emission to the photocathode of

the PM tube. The 133 keV γ-ray detector was a cylinder of

25mm diameter by 6mm thickness and the 482 keV γ-ray

detectors were 25mm diameter by 25mm thickness. The use of

three detectors, as shall be explained in section 3.2,

enabled the simultaneous recording of two coincidence

spectra. These detectors have efficiencies of 80% and 65%

for the 133 keV and 482 keV γ-rays respectively (HA64).

The 133 keV detector was covered by a 0.8mm cadmium absorber

for the low energy X-rays and the 482 keV detectors were

covered by 3mm lead absorbers to reduce the intensity of the

133 keV γ-rays. The source-detector distance was $\simeq$ 25mm even

for the low temperature runs because of the narrow tail of

the liquid helium cryostat in which the source was positioned.

The PM tubes used were the RCA 8850 and RCA 8575. Both of

these tubes are excellent for timing experiments because of

the fast rise-times, about 2 ns, high gain and low noise.

The 8850 was chosen for the 133 keV detector because it has

a higher gain than the 8575. The detectors were optically
coupled to the faces of the PM tubes via silicone grease
and the whole assembly was made light tight with a cover-
ing of black electric insulating tape.

The tube base is essentially an external resistor
divider chain used to maintain the PM dynodes at the
required potentials. It also provides outputs for the
fast timing pulses taken from the anode and the energy
selection pulses taken from the ninth dynode. The photo-
cathodes of the PM tubes were kept at − 2600 V and − 2700 V
relative to the anodes for the 8575 and 8850 respectively.
Too low a voltage would reduce the gain of the PM tube and
give poorer time resolution due to increased transit time
variation of the electrons travelling down the PM tube while
too high a voltage would increase the dark current or noise
of the PM tube.

In scintillation counting, a common problem is that
of the dependence of the gain of the PM tube on the rate
of scintillation producing events. This is due to a change
in the inter-dynode voltages which is caused by the high
inter-dynode currents relative to the voltage-divider
current of the base i.e. the large number of electrons,
impinging on the dynodes cannot be balanced by the voltage-

divider current and a change in the inter-dynode voltages and hence, in the gain of the PM tube, results. This can be somewhat reduced by designing a high-current base but this involves bulky, high wattage components and the resultant heat requires the base to be fan cooled.

Although this problem was not of a critical nature in the present work because of the slowly varying activity of the ^{181}Hf source with a half-life of 42 days, a base using Zener diodes as voltage stabilizers was constructed. The first stage and the last three stages of the PM tube were chosen for stabilization because direct, inter-dynode voltage measurements showed these to be the most sensitive to counting rate changes. Although a full chain of Zener diodes would be most stable, it would only have one operating voltage whereas the present design operates from 2500 V to 3000 V. The voltage distribution across the dynodes is somewhat affected by voltage supply changes but this is not serious. Tests showed that this base operating at 2 ma was more stable by a factor of two than a 10 ma base. The time resolution of the system was not affected by the new design.

This base was used for one of the 482 keV detectors while the other 482 keV detector used a commercial ORTEC 265

2 ma base. Except for the higher gain stability of the

Zener diode base, the performance of the bases was

identical. The base of the RCA 8850 PM tube used a

conventional 2 ma design that followed the voltage

distribution recommended by RCA.

2. The Electronic System

The type of system used in the present experiment

was the "fast-slow" delayed coincidence system which is

schematically outlined in figure 3.1. The "fast" side

consists of the anode pulses, discriminators and time-to-

amplitude converter.(TAC). The fast anode current pulse

marks the time of arrival of a scintillation producing event.

The discriminator is a circuit that produces a standardized

pulse when triggered by an appropriate anode pulse. The

voltage level above which the discriminator is triggered may

be varied. For NaI, it is generally chosen to be as low as

possible, just above the PM tube noise, in order to achieve

the best time resolution (BO71). The outputs of the

discriminators are connected to the start and stop inputs

of the TAC. The TAC is basically a device which converts the

start-stop time interval to a pulse whose height is proportion-

al to the time interval. This pulse is then analyzed and

stored by the pulse height analyzer. The accumulated data

Figure 3.1

Schematic of a Fast Slow Coincidence

System

scintillators

dynode   PM   source   PM   dynode

anode   anode

discriminator   discriminator

START   TAC   STOP

SCA   SCA

linear
gate   coincidence
                                       unit

pulse height
analyzer
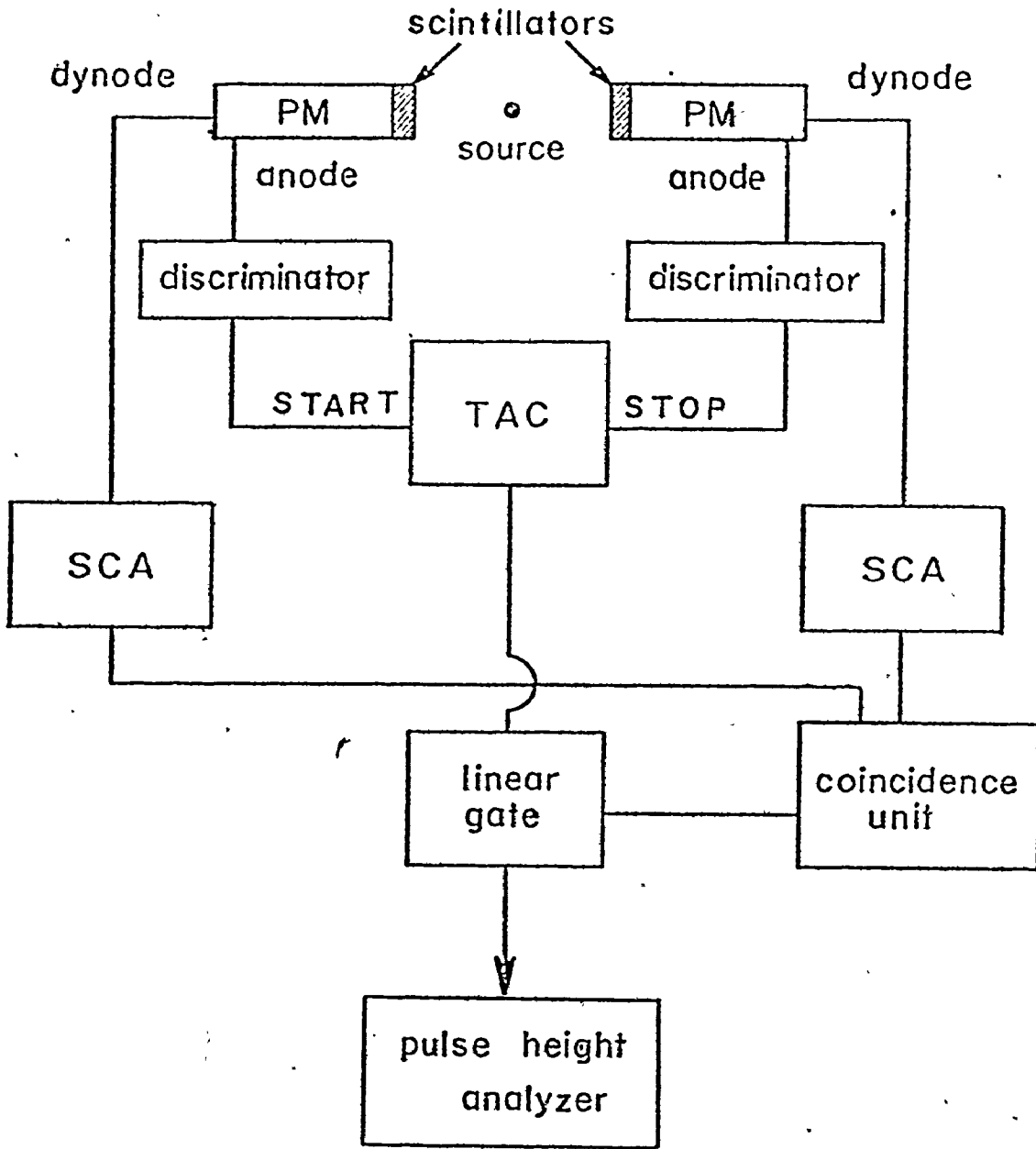
is a plot of the number of start-stop coincidences as a function of time.

The "slow" side of this coincidence system makes use of the slower, integrated dynode pulses whose height are proportional to the energy of the scintillation events. These pulses are shaped, amplified and then fed to the single channel analyzers (SCA) where the energy selection is performed. The SCA produces a logic pulse output when the input pulse is within the desired energy "window" defined by adjustable upper and lower levels. Coincidences between the SCA logic pulses indicate that the energy conditions for both the start and stop detectors have been satisfied. These coincidences open a linear gate which allows analysis and storage of the TAC output pulse. Hence, the "fast" side yields the timing information and the "slow" side controls the energy selection.

The electronic configuration adopted for the present work required some additional electronics in order to simultaneously record two coincidence spectra as measured with one stop detector and two start detectors. The electronic system is shown in figure 3.2. The start input of the TAC was coupled to two pulses which indicated an event at either 90° or 180° relative to the stop detector. The start-stop

Figure 3.2

The Electronic System for the

DPAC Measurements
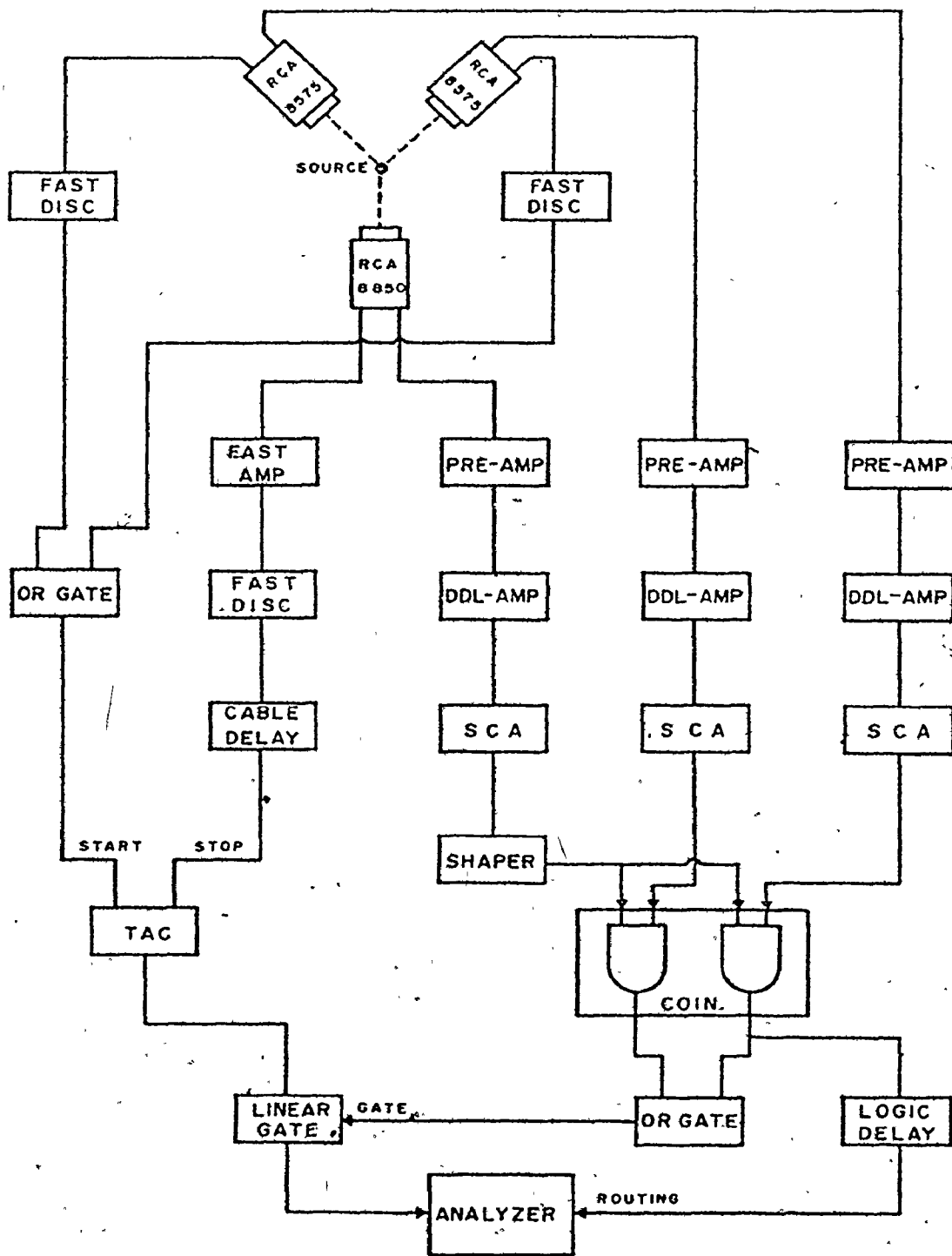
coincidences were energy selected as described earlier
with the linear gate being opened by coincidences at
both 90° and 180°. In addition, the SCA coincidence signal
between the stop detector and only one start detector was
used as a routing pulse to direct the coincidence spectra
at 90° and 180° to different halves of the analyzer. Each
spectrum contained 256 channels.

The SCA output of the stop detector was first
shaped by a monostable (Texas Instruments SN74121) before
entering the SCA coincidence unit. This shaper was used to
vary the width of the stop SCA pulse. The optimum width is
equal to the TAC timescale range (100 ns or 200 ns was chosen)
but this was increased by 50% in order to allow for less
critical adjustment in setting up the experiment. The delays
of the SCA outputs were optimized by using the prompt events
produced by the coincident 511 keV γ-rays from a ^{22}Na source
(see section 3.4). This source was also used to adjust the
timing of the pulses coupled to the analyzer routing input
as follows. A coincidence experiment was performed with
only the 180° start-stop detector combination in use.
These coincidences were routed to the upper half of the
analyzer. Coincidence pulses that "fell" into the lower
half were indicative of poor routing. The timing of the

routing pulse was set to slightly precede (≈ 0.5 µs) the linear gate output as prescribed by the analyzer instruction manual. All coincidences were then stored in the upper half of the analyzer.

Although the 133 keV γ-ray is emitted from the ^{181}Ta nucleus before the 482 keV γ-ray, the TAC was started by the latter and stopped by the artificially delayed 133 keV γ-ray. This is because the dead time of the TAC is controlled by the start rate and the 133 keV detection rate was higher than that of the 482 keV γ-ray. A cable delay of about 100 ns was used rather than a logic delay because of its higher stability. Logic delays, which have an inherent deadtime, tend to degrade fast pulse shapes and they are also rate dependent. The resultant spectra are thus stored "back to front" with time increasing to the left (figure 6.1).

3. The Measurement Procedure

The three detector assemblies were mounted on an aluminum structure so that all three detectors pointed to and were at the same height as the source. The angle between the two 482 keV start detectors was fixed at 90° but the angle between these and the 133 keV stop detector was variable. The experiments were performed by alternating daily between two positions as shown in figure 3.3. This

Figure 3.3

Detector Configuration

These two positions were alternated for each of the daily runs.

POSITION 1

180°

| STOP | ✳ SOURCE | START #2 |

90°

START #1

POSITION 2

START #2

90° SOURCE

| STOP | ✳ | START #1 |

180°
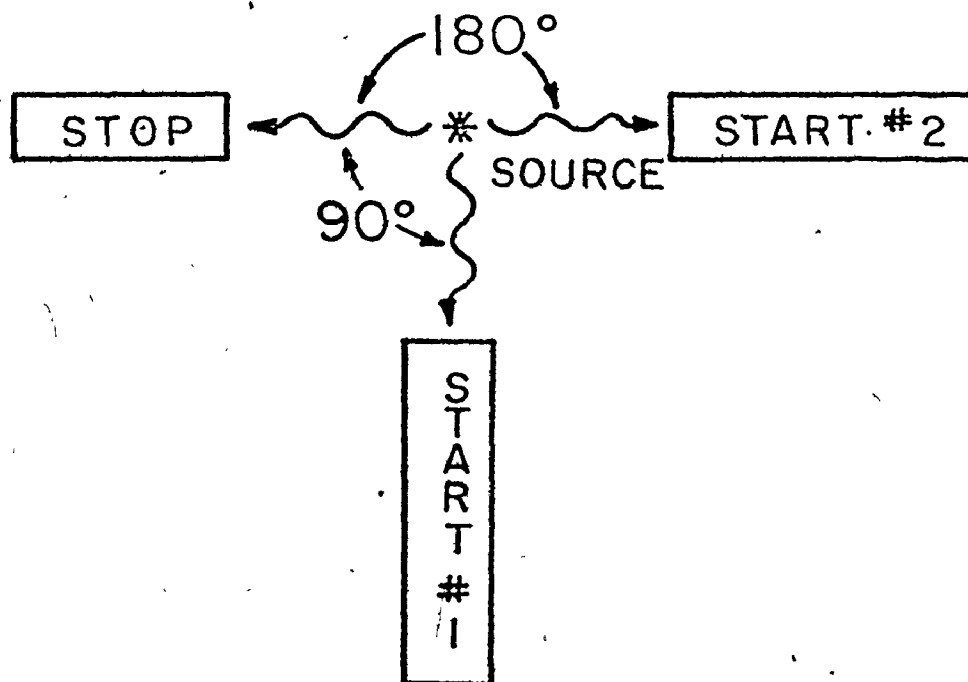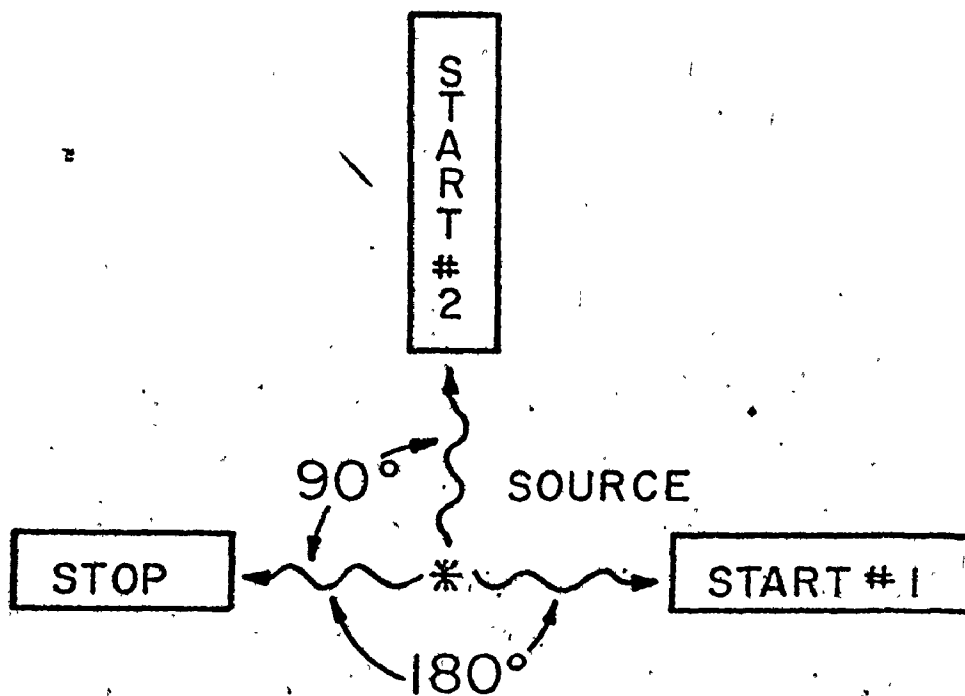
procedure made use of the two available 90° positions and this reduced errors due to possible incorrect source centering. Furthermore, the alternate use of each start detector at 90° and 180° lessened the chance of systematic errors in the data collection.

The SCA outputs were scaled prior to all runs to check for equal count rates in both start detectors. They were also scaled during each of the daily runs. These were checked against the 42 day decay of the source in order to monitor any drifting of the SCA energy "windows" during the experiment. These drifts were minimized by temperature control of the room and the use of a forced-air cooling cabinet for the electronics.

The timescale of the TAC was calibrated periodically (section 3.4) and the time resolution of the system was measured at the beginning and end of a series of runs. These checks verified the stability of the electronic system. The data recorded over a one day period was printed out by a typewriter interfaced to the pulse height analyzer and then transformed to cards from which the computer data analysis was carried out.

4. The Measurement of Time Resolution

The time resolution of the system plays a critical role in the proper evaluation of the attenuation function $G_k(t)$

(see chapter 4). The time resolution function, which should be measured under the same conditions by which the data were collected, was obtained as follows.

The start and stop detectors were placed at 180° relative to each other and the energy selection windows of the SCA's were set at 482 keV and 133 keV respectively, as determined by a ^{181}Ta source. This source was replaced by a ^{22}Na source encapsulated in aluminum. This source emits two 511 keV γ-rays at 180° due to positron annihilation in the aluminum following the β^+ decay of ^{22}Na and also a 1275 keV γ-ray from the daughter nucleus ^{22}Ne. Since the 511 keV γ-rays are coincident in time, i.e. prompt, the resulting time interval distribution is a measurement of the time resolution of the system. The prompt peak was measured with the same energy discrimination as used during the experimental runs because of the energy dependence of the time resolution (BO71). This arrangement allowed possible 511-1275 keV coincidences which are not simultaneous γ-rays but are separated by a time interval determined by the lifetime of the positrons in the aluminum holder. However, such coincidences had a negligible effect on the measured time resolution because the 0.2 ns lifetime of the positrons in the aluminum (BE60) is small in comparison to the 1.8 ns

time resolution of the system. The resolution measurements were carried out over a one day period as were all the data runs, in order to measure any effects produced by electronic gain or zero shifts that tend to worsen the time resolution of the system

Figure 3.4 shows two prompt spectra acquired with the same stop detector but different start detectors. These two combinations were used for the data collection. The prompt curves have been normalized to the same peak height. The similarity of shapes and resolution for both combinations is quite apparent. The slightly steeper slope of the left-hand side of the prompt curves when compared to the right-hand side reflects the better time resolution one obtains for higher energy events, i.e. a start energy of 482 keV as opposed to a stop energy of 133 keV. This asymmetry is some-what reduced by the better resolution of the smaller 133 keV detector. The prompt curves obtained in this manner were used in the data analysis.

5. TAC Timescale Calibration

A. Introduction

In DPAC experiments, it is important to perform accu-rately the calibration of the TAC timescale as the asbolute precision of the measured quadrupole interaction frequency

Figure 3.4

Experimental Time Resolution

These prompt curves were obtained with the same
stop detector and either of the two start detectors.

FWHM=1.8 ns

1.0 ns
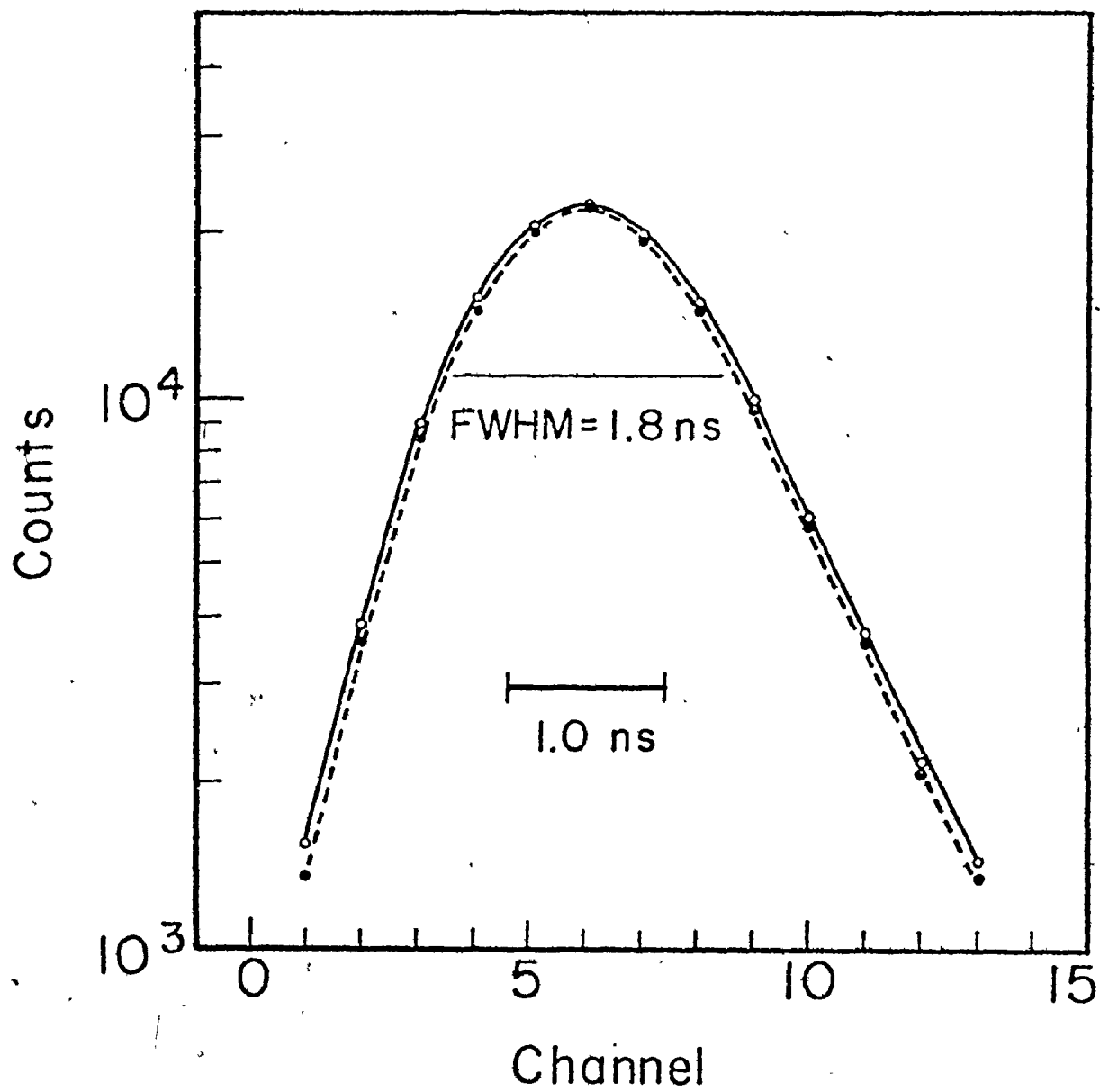
is directly related to this calibration. Many methods
of calibration have traditionally been used. These
procedures usually calibrate the timescale by inserting a
known delay into the start or stop side of the TAC and
measuring the displacement of the prompt peak in the time
spectrum. The precise measurement of the inserted delay is
then a problem. In general, these methods are time consuming
particularly if an accuracy of better than 1% is required.
The timescale calibrations for the present experiments were
performed precisely and quickly with a special calibrator
developed by Boulter et al. (BO70).

B. The TAC Calibrator

This device correlates the start and stop pulses with
a high frequency r.f. signal so that the start-stop time
interval is restricted to a random multiple of the r.f.
oscillator period (figure 3.5). The resulting peaks which
are generated across the TAC timescale are separated by one
oscillator period and hence yield the timescale calibration.
The precision of this device is based on a highly-stable
100 MHz crystal oscillator scaled down so that 10, 20, 40 or
80 ns calibration peak spacings may be selected. A direct
measurement with a frequency meter showed the oscillator
precision to be better than 8 parts in 500,000. Figure 3.6

is a typical timescale calibration spectrum acquired in
only a few minutes of running time. The spacings of the
calibration peaks provide an estimation of the integral
nonlinearity of the system (BA68) as channel number and
time are not necessarily related (section 4.3).

In a check on the calibrator, a linear least squares
fit of the peak centroid position to channel number after
correction of the peaks via the differential nonlinearity
curve (DNL, section 4.3) yielded a calibration of
0.5044 ± 0.0005 ns per channel. This linearity is a good
indication of the accuracy of both the TAC calibrator and
the DNL correction method. A second run compared the
calibrator to a calibration performed by using stop insertion
delays obtained from a commercial delay line module[†]. These
yielded identical calibrations to within the statistical
accuracy of the data (figure 3.7).

Calibrations were performed regularly during the
course of a series of daily runs. The calibration varied less
than 0.5% for any series of runs. Considering the stability
and precision of the calibrator, it can be concluded that the
error in the timescale calibration is negligible in comparison
to the statistical errors of the present experimental data.

[†] Dual Delay Line Module, Model 21, Chronetics Inc.,
Mount Vernon, N.Y.

Figure 3.5

Schematic of the TAC Calibrator
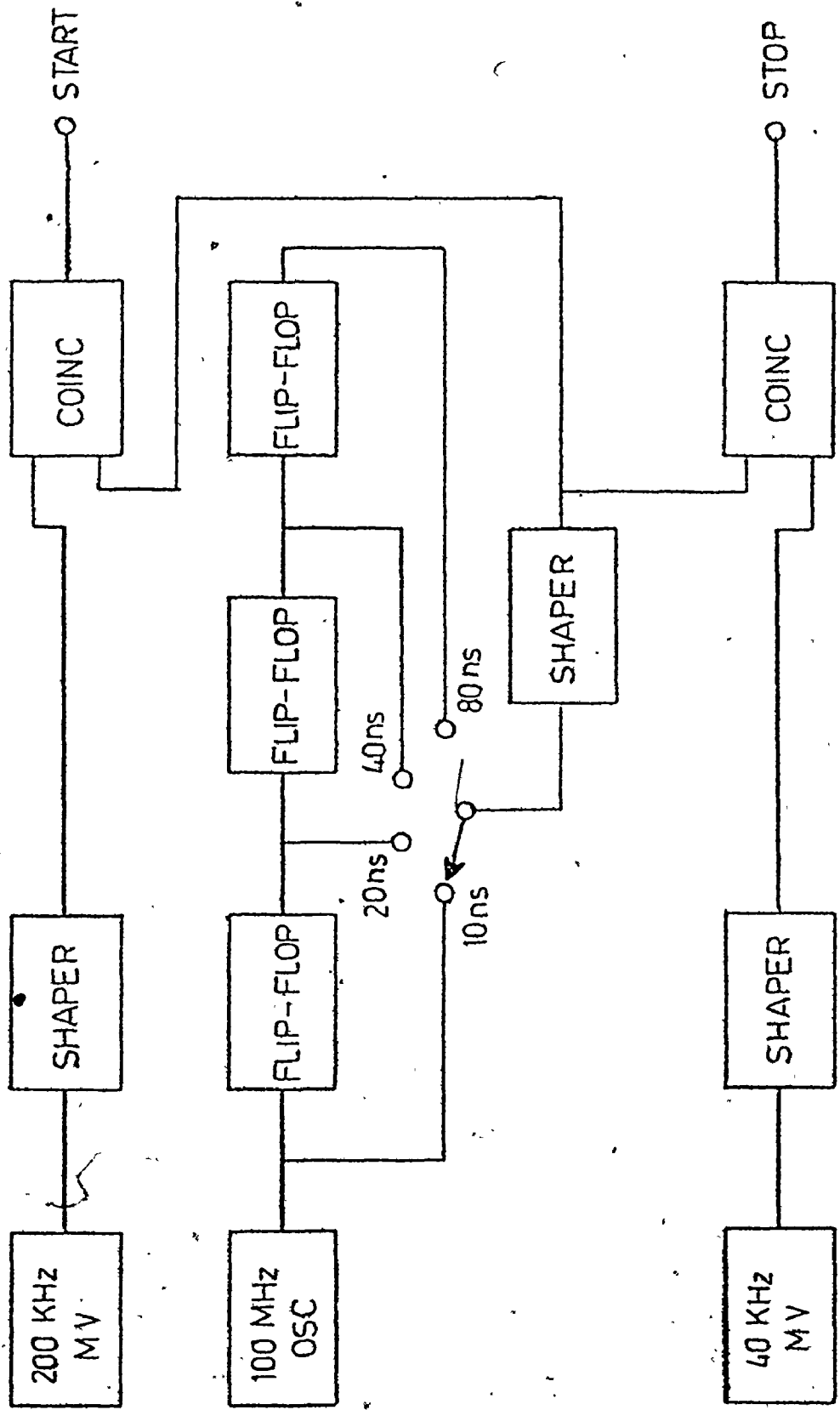
Figure 3.6

Typical TAC Calibration Curve

PEAK INTERVALS= 10 NS

CHANNEL

COUNTS

48
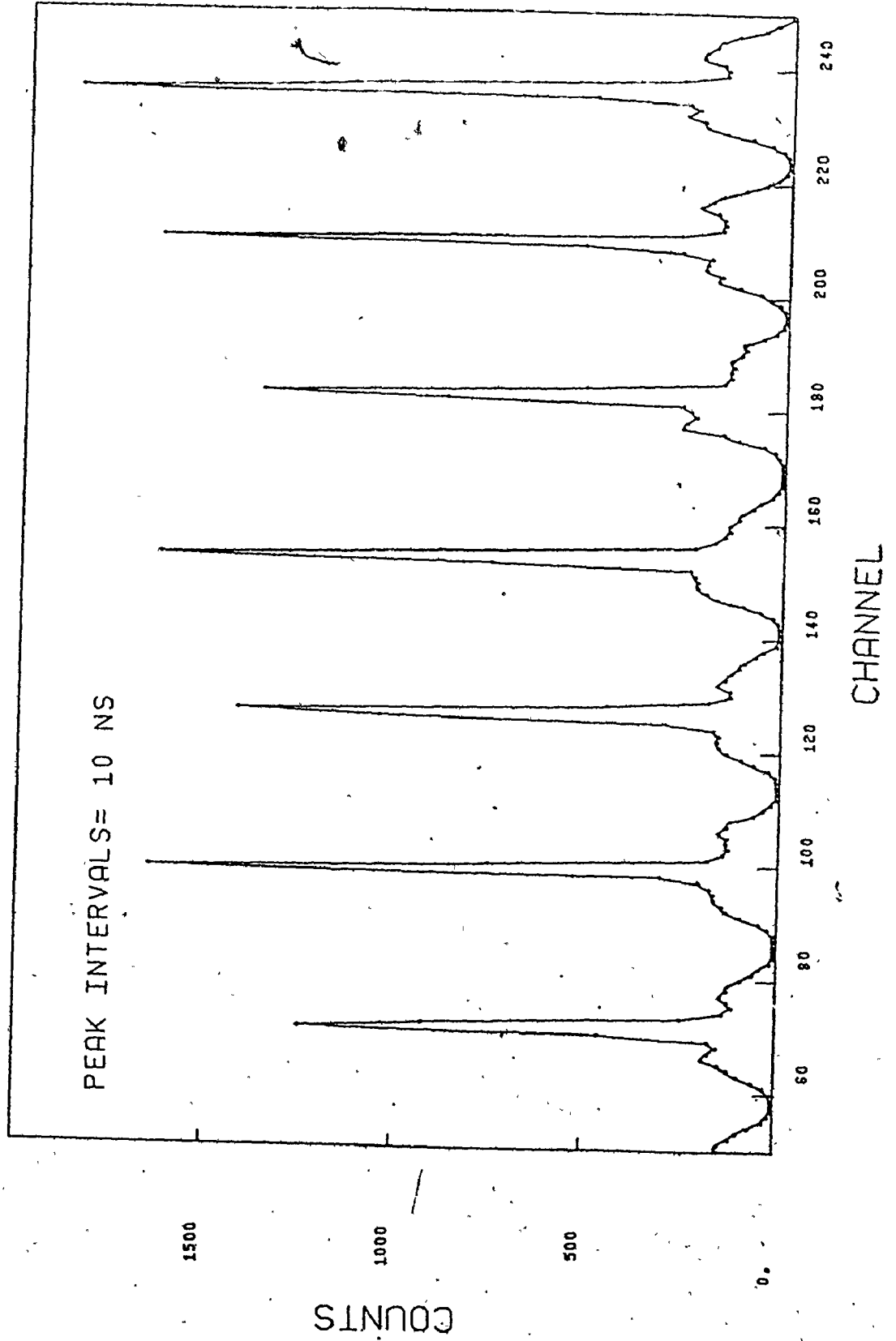
Figure 3.7

Comparison of TAC Calibration Methods

These calibrations were performed with the TAC calibrator
and also by the insertion of variable stop delays obtained
from a commercial module.
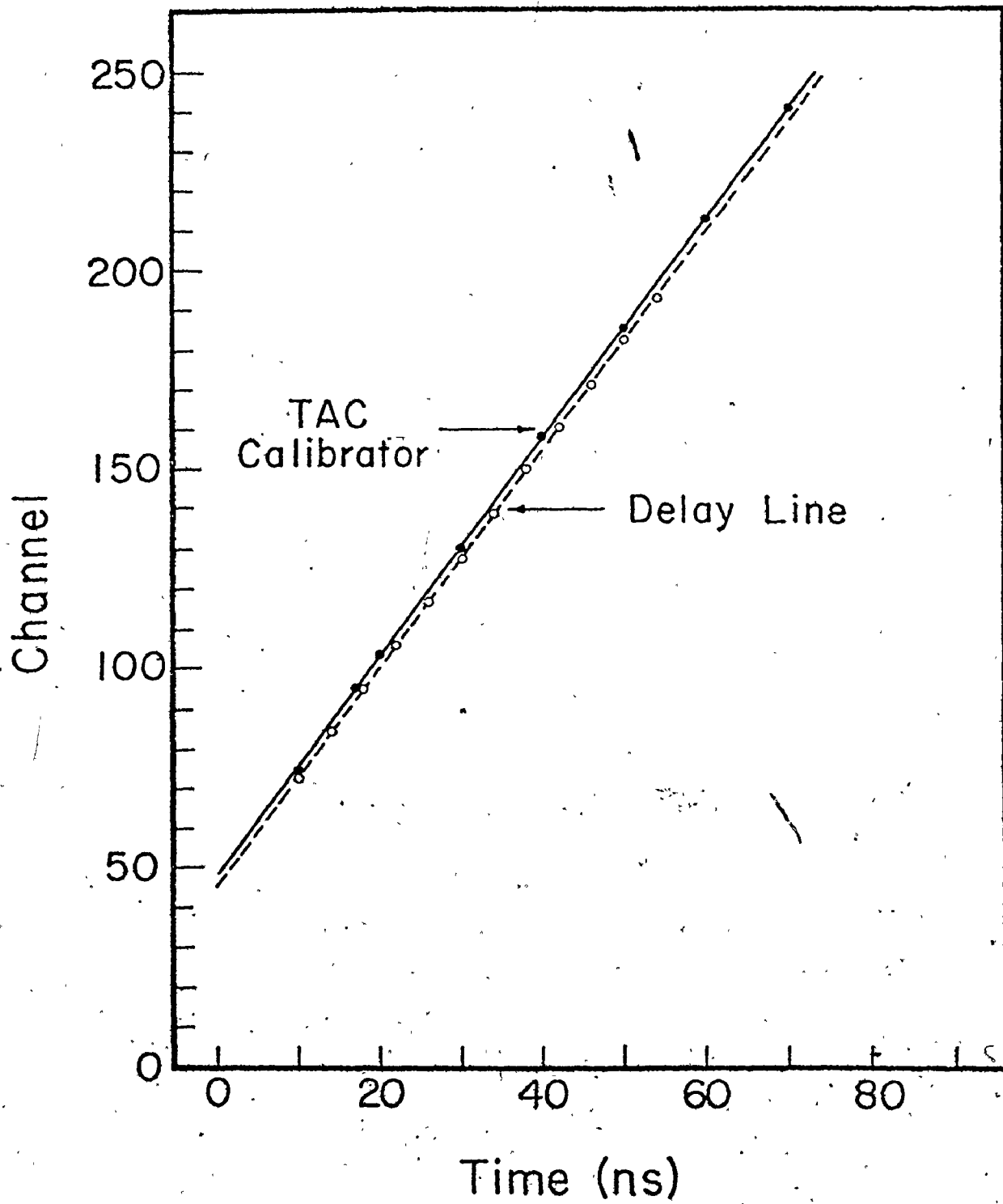
CHAPTER   4

Instrumental Effects In Differential
Perturbed Angular Correlation Measurements

The determination of the perturbed angular correla-
tion function $W(\Theta,t)$ from which the attenuation function
$G_k(t)$ is obtained necessarily involved the measurement of the
two independent variables Θ and t. However, the measuring
system contains inherent limitations that affect the perfect
calculation of these quantities; namely, a finite time response
and a finite angular resolution. There is in addition the
problem of nonlinearity that occurs to some degree in all time
spectra measurements. In this chapter, the effects of these
limitations on the measurement of the angular correlation
function and the associated attenuation function are discussed.
Finally, the problem of chance coincidence background in time
spectra acquired by means of a start-stop TAC is presented and
analysed.

1.   Finite Time Resolution In Differential Perturbed Angular
     Correlation Measurements

The data accumulated by the delayed coincidence system
described in chapter 3 is a plot of the number of $\gamma_1 - \gamma_2$
coincidences as a function of time. Such a system is often
used to measure the lifetime of an excited nuclear state.
The plot obtained is of the form $\exp(-\lambda t)$ where λ is the

decay constant of the excited state. The present DPAC studies seek to determine perturbations in this exponential coincidence plot. This system however has a finite time resolution that degrades the measurement of such perturbations i.e. if the two γ-rays are emitted simultaneously, then the form of this time distribution or prompt peak should be a δ function at time zero for perfect time resolution. However, the detectors and associated electronics produce some uncertainty in the measurement of the time of arrival of the γ-rays and the resulting prompt curve has a finite width τ. For a time distribution that is Gaussian shaped, τ is the standard deviation. Experimentalists generally measure the full width at half maximum (FWHM) of the prompt peak which is related to τ by FWHM = 2.35 τ and is referred to as the resolution. The present data were obtained with a resolution of 1.8 ns.

This effect has been studied by Beraud et al. (BE69) who calculated the distortion in the attenuation function $G_k(t)$ that is produced by a finite time resolution τ. The measured attenuation function is a weighted convolution of the theoretical attentuation function $G_k(t)$ and the time response function $p(t-t')$ of the system, the weighting factor being the factor $\exp(-\lambda t)$. Thus, we have

$$<G_k(t)> \quad = \frac{\int_0^\infty p(t-t')\exp(-\lambda t')G_k(t')dt'}{\int_0^\infty p(t-t')\exp(-\lambda t')dt'} \tag{4.1}$$

If a Gaussian time response is assumed and $G_k(t)$ represents a static quadrupole interaction (equation 2.10), this yields

$$<G_k(t)>_\tau \quad = \sum_{n=0}^{n_{max}} a_{kn} \exp(-\omega_n^2\tau^2/2)\cos(\omega_n t) \tag{4.2}$$

Thus, the finite time resolution produces a damping in the oscillation amplitudes of the frequencies by a factor $\exp(-\omega_n^2\tau^2/2)$. This effect is particularly important when ω_n is of the same order of magnitude as $1/\tau$. The finite time response acts as a filter and for large values of $\omega_n\tau$ the oscillations in $G_k(t)$ are suppressed. The time resolution thus puts an experimental limit on the measurable values of ω_n.

Beraud et al. calculated the form of $G_2(t)$ from equation 4.2 for various values of time resolution and asymmetry parameter η for the case of level spin 5/2 and the results for $\eta = 0.5$ are shown in figure 4.L. Note the damping of the amplitude of $G_2(t)$ and the loss of the high frequency components as the resolution is worsened. A quantitative knowledge of this finite time resolution

Figure 4.1

The Effect of a Finite Time Resolution

on $G_2(t)$

These curves were generated for $\eta = 0.5$ and $\omega_1\tau$ values of

a) 0, b) 0.211π, c) 0.30π, d) 0.38π
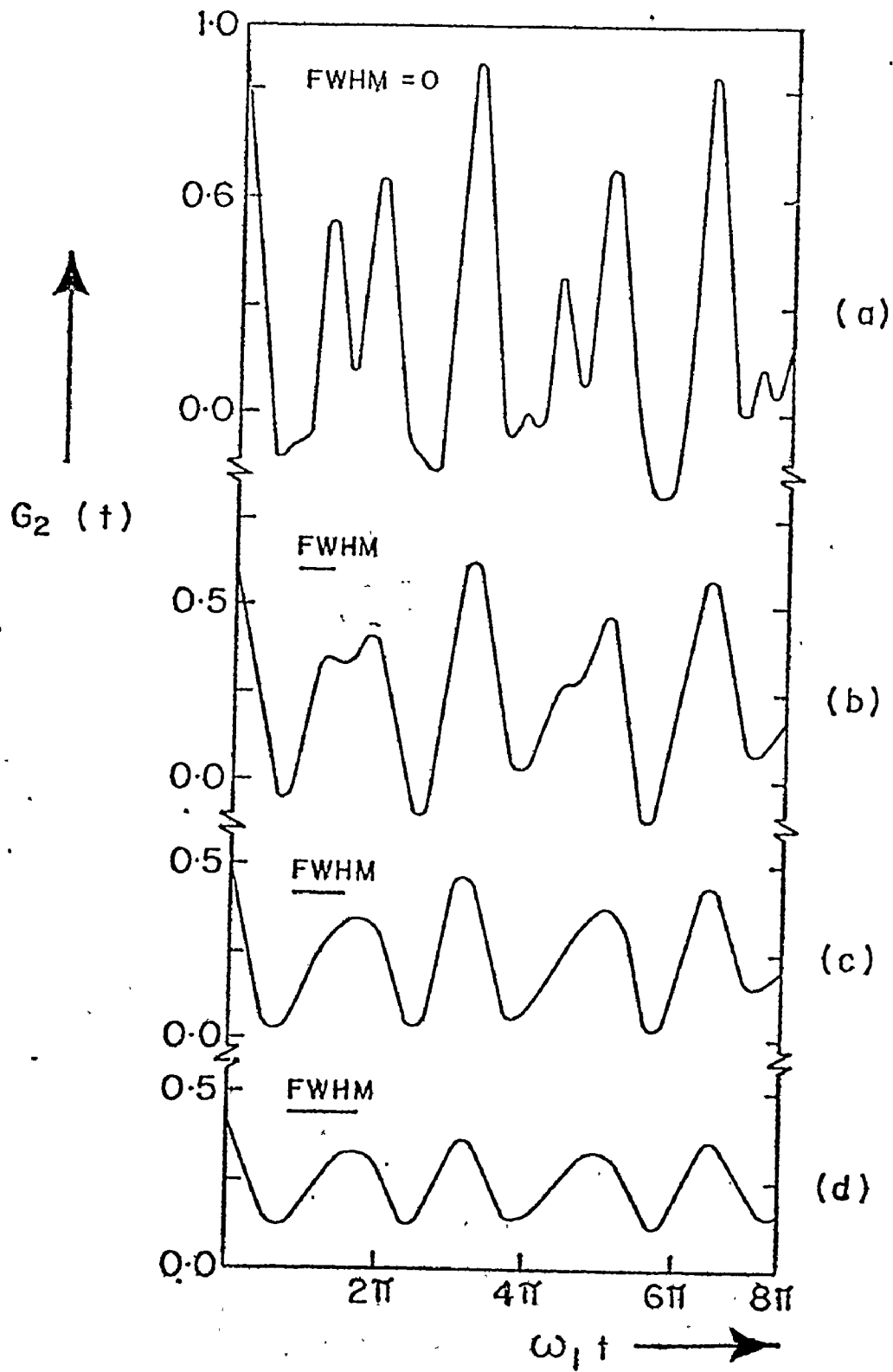
degradation is particularly important for the proper
calculation of FFG distribution widths which also cause
damping effects in the $G_k(t)$ function (equation 2.15).

2. The Finite Solid Angle Effect

The expression for the angular variation of the
intensity of a cascade pair of γ-rays (equation 2.1)
assumes point size detectors and sources, which is of course
not valid for experimental measurements. The effect of a
finite source size is negligible in the present work
($\approx$ 2 to 3mm square) and need not be calculated. As has
been discussed by Rose (RO53), the effect of finite detector
size is to introduce into each term of the angular correlation
function an attenuation factor so that the correlation is
somewhat smeared out. For detectors having axial symmetry
about the propagation directions of the γ rays, the form of
the distribution is unchanged but the coefficients are replaced
by

$$A_k' = Q_k^1 \, Q_k^2 \, A_k \tag{4.3}$$

where the Q_k^i correct for all the geometric effects on the
observed distribution function and i=1,2 refers to each of
the two detectors. The Q_k are a function of the probability
of absorption of a γ-ray and hence depend on detector

thickness and γ ray energy. The Q_k also depend on whether one counts the whole γ spectrum at each angle or just the photopeak. This is because the γ-rays interacting at the edge of the detector are less likely to contribute to the photopeak than those interacting at the centre. However, these effects are small (≈ 1%, YA65) and for the present case, we will consider full absorption. In this limit, Rose (RO53) has shown that

$$Q_k = \frac{P_{k-1}(X) - XP_k(X)}{(k+1)(1-X)} \qquad (4.4)$$

where $X = \cos \gamma$, γ is the half-angle subtended by the source at the face of the detector and P_k is a Legendre polynomial of order k. For k=2, this becomes

$$Q_2 = \frac{1}{2} X(1 + X) \qquad (4.5)$$

Using a value of $A_2 = -0.295$ (AV71), the present arrangement gives $A_2' = -0.21$. The values of A_2' were found to be in the range 0.20 ± 0.03. Because the finite solid angle effect is more pronounced for the A_4 coefficient which is initially quite small (-0.069, AV71), A_4 can be omitted in a good approximation of $W(\theta,t)$.

This effect can be decreased by using smaller detectors and/or larger source-detector distances. However, this

lengthens the data collection time needed for a given
statistical accuracy and so a compromise between the solid
angle attenuation effect and counting time must be chosen.

3. System Nonlinearities in Time Spectra Measurements

A. Introduction

The proper analysis of a complex time spectrum such
as that obtained in a DPAC experiment requires an accurate
knowledge of the linearity of the TAC-ADC system that con-
verts the delayed coincidence signals to stored time events.
ADC refers to the analogue-to-digital converter of the pulse
height analyzer. Experimentally, the time t is a function
of the channel number n of the ADC, $t = t(n)$, and therefore

$$P(t)dt = P(t(n)) \frac{dt}{dn} dn , \qquad (4.6)$$

where $P(t)$ is the time spectrum to be measured and $P(t(n))$
is the data obtained. Nonlinearities arise if the time
interval corresponding to one channel width, $\frac{dt}{dn}$, varies
from channel to channel (differential nonlinearity) or if
over a number of channels $t(n)$ is a non-linear function
(integral nonlinearity). In particular, if Δt_n is the
time interval corresponding to channel n of the ADC and
Δt is the true time interval of a channel in the absence

of all nonlinearities, then the differential nonlinearity ℓ_n of channel n is defined as

$$\ell_n = (\Delta t_n - \Delta t)/\Delta t \qquad (4.7)$$

In a real system $t_n = t_o + \sum_{i=1}^{n} \Delta t_i$ differs from $t_o + n\Delta t$ and one defines the integral nonlinearity L_{1n} from channel 1 to channel n as

$$L_{1n} = t_n - (t_o + n\Delta t)/(n\Delta t) \qquad (4.8)$$

$$= \sum_{i=1}^{n} \ell_i/n$$

The spectral shape will be distorted if such nonlinearities are present. If distortions are to be avoided or corrected all ℓ_n should be negligibly small or very accurately known. These errors appear to some degree in all systems and much effort has gone into their measurement and removal (e.g. IR66, BL67, SC68, BA68, CO70). In order to measure the effect of these nonlinearities in the present work and to correct for these effects if necessary, a method analogous to that suggested by Turner (TU70) was used to measure the differential nonlinearity curve (DNL) of the TAC-ADC system.

B. The DNL Measurement

Figure 4.2 shows the electronic schematic of the

Figure 4.2

Schematic of the Measurement of

the DNL Curve
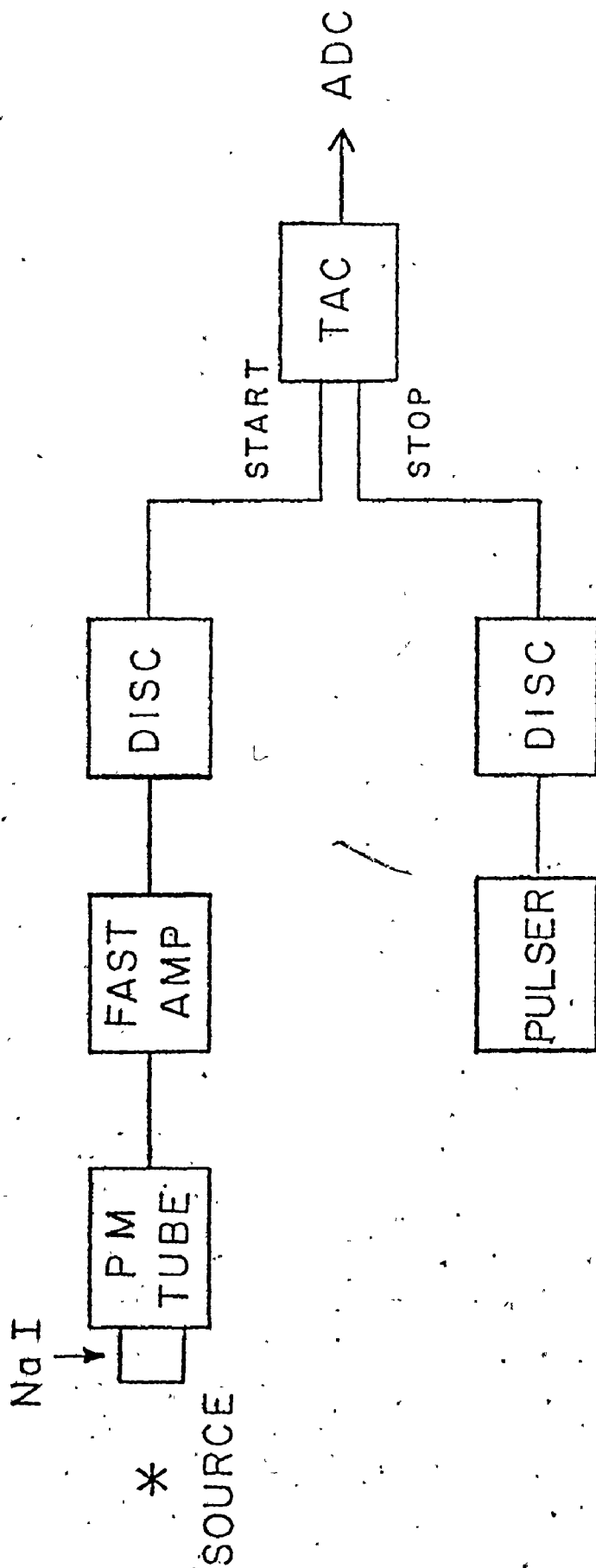
DNL measuring apparatus. The high rate periodic stop was chosen to have a period greater than the TAC timescale under consideration. The start pulses, produced by the decay of the radioactive source, occur at random during stop intervals of constant length and a uniform accidental distribution results. Good statistics are acquired in only a few hours of running time. Care must be taken in the choice of input rates as electronic distortions of the DNL due to analyzer pile-up or overdriving of the TAC input circuitry might result in a DNL curve that is not properly indicative of the DNL curve of the TAC-ADC system while running at lower data acquisition rates. For this reason, a lower rate DNL curve was measured over a longer time period under otherwise identical conditions. Upon comparison of the two curves, no sign of electronic distortion in the high-rate DNL curve was observed.

This DNL curve (figure 4.3) which would be flat in a perfect system is a measure of the nonlinearities of the system. The count in each channel n is directly proportional to the time width Δt_n of that channel and the integral of the counts from some arbitrary zero to that channel is proportional to the time position t of that channel. Thus

Figure 4.3

Differential Nonlinearity Curve

The region of high nonlinearity below channel 70 was not used
in the final data analysis.
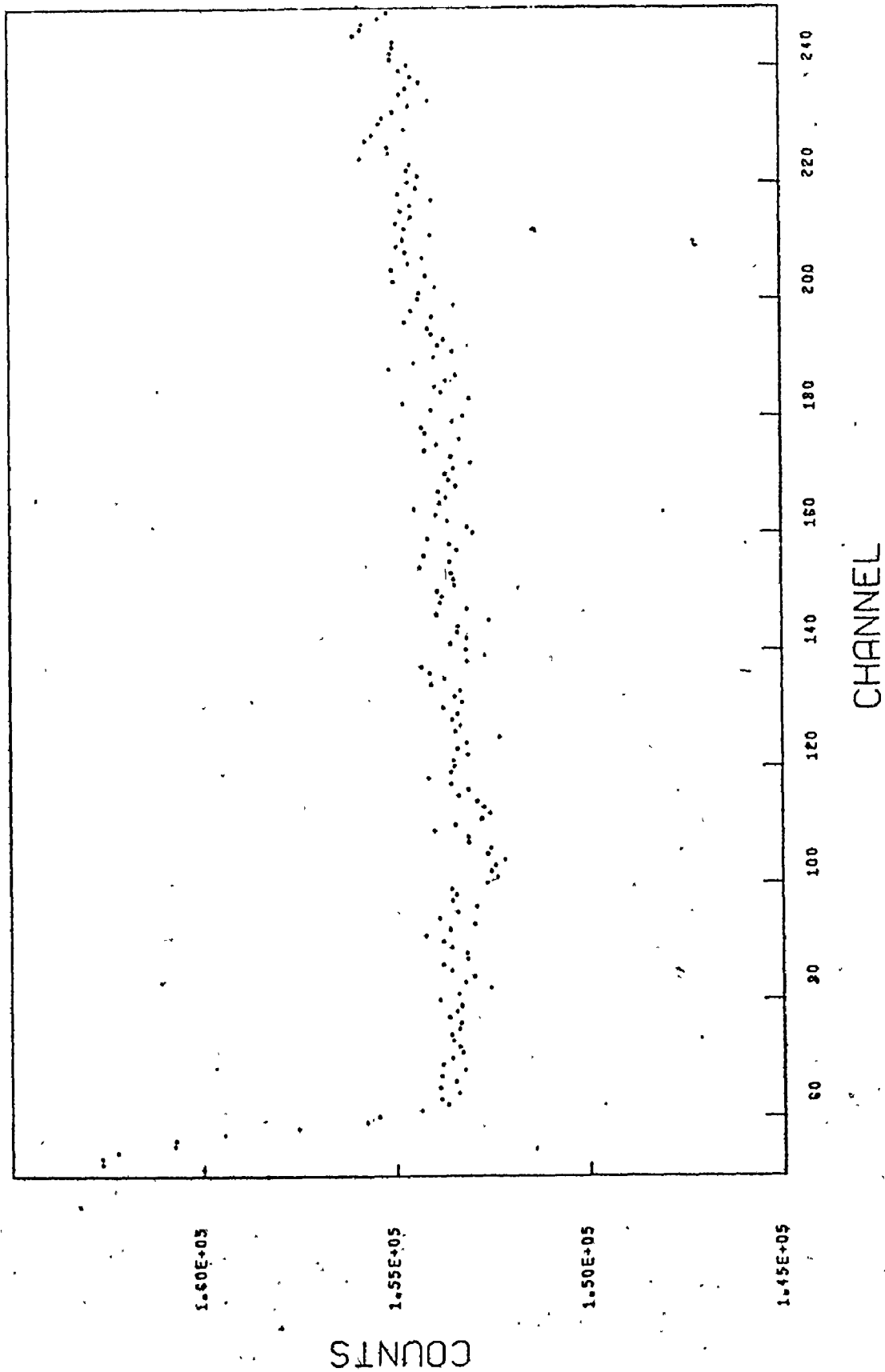
if $M(t)$ is the measured time spectrum and $D(t)$ is the DNL curve, then the corrected spectrum $C(t)$ in each channel n is

$$C_n = R_n \frac{\Sigma\ M_n}{\Sigma\ R_n} \qquad\qquad (4.9)$$

where

$$R_n = \frac{M_n}{D_n}$$

and the summations are over the entire area of the spectrum to be corrected. This ensures a constant channel width. Also, since $\Sigma C_n = \Sigma M_n$, the total number of counts in the corrected and measured spectra are equal. The time position t_n of each channel n as measured from the first channel of the corrected spectrum is given by

$$t_n = \frac{\sum\limits_{i=1}^{n} D_i}{\Sigma\ D_i}\ .\ \text{CAL} \qquad\qquad (4.10)$$

where CAL is the timescale calibration obtained as described in section 3.5.

These simple equations were incorporated into a short FORTRAN data correction program. To check the operation of the program, a DNL curve of 0.3% statistical accuracy was corrected using itself as the correction data and as expected a perfectly flat line resulted. A second DNL of 0.9% accuracy

was measured in a shorter time but under otherwise identical conditions. Of the 201 channels in the area to be corrected, there were 85 channels outside the one standard deviation range $\overline{N_i} \pm \sigma_i$, 18 of which had individual deviations from linearity of greater than 2%. This DNL curve was then smoothed using the first DNL curve as the correction data. The corrected spectrum had 65 channels outside the range $\overline{N_i} \pm \sigma_i$. For perfectly linear data, 33% of the 201 channels or 67 channels would be outside this range. Only 4 channels had individual nonlinearities of greater than 2%. The average percentage deviation from linearity for all channels before and after correction was 1.2% and 0.7% respectively. The calculated standard deviation of the corrected data was 103 which compares well with $\sqrt{N_i} = 107$. The 0.7% figure is better than the 0.9% statistical accuracy of the data and as noted by Turner (TU70) the ultimate accuracy is determined by the statistics of the DNL measurement.

A further test of this method, in particular the correction for integral nonlinearity or the proper time positions of the channels, involved the measurement of the lifetime of the 482 keV level of ^{181}Ta as described in chapter 6. Figure 6.5 is a plot of the delayed coincidence

time spectrum after the DNL correction. The extension
of the data to over 12 half-lives in a true exponential
decay as indicated by a least squares fit is a good test
of the power of this method. Any significant integral
nonlinearity would not permit the data to be properly
fitted to an exponential model.

Different DNL measurements performed 10 days apart
showed no significant differences indicating the stability
of the DNL curve of the system.

4. Chance Events In Delayed Coincidence Experiments

A. Introduction

DPAC delayed coincidence experiments measure the
time interval distribution of correlated start-stop events.
In addition, there is a contribution to this correlated
distribution from uncorrelated start-stop events that produce
the chance or background distribution. This background has
generally been considered to be of the form $\exp(-\lambda_b t)$ where
λ_b is the probability of a chance coincidence per unit time.
A point which has not been recognized is that the correlated
and chance distributions are not independent but that they
interact to produce apparent discontinuities in the back-
ground. The background level is suppressed in the region

corresponding to time intervals longer than those assoc-
iated with the correlated events. Such an effect has been
noted by Matoba et al. (MA71) for fission product recoil
time spectra. They, however, attributed this phenomenon
to a physical situation peculiar to their type of experiments.
Since this effect appears to varying degrees in all time-
interval measurements using a TAC, it was investigated more
fully. What follows is a description of the experimental
arrangement and data analysis techniques used in this
investigation (LO72).

B. Experimental arrangements and results.

In order to investigate the effect under controlled
conditions, two experimental arrangements were used. A block
diagram of the first arrangement is shown in figure 4.4.
The output of a digital clock was fanned out into two branches:
the first provided the start timing marker and the second was
coupled to a variable length register. The output of the
register was delayed and reshaped to provide the correlated
stop output. In this way the fraction of start events prod-
ucing correlated events could be varied as $(\frac{1}{2})^L$, where L is
the length of the register. The correlated output was then
mixed with the output of a random noise generator, this being

Figure 4.4

Block Diagram of the Electronics

used to vary the fraction of start events producing correlated
stop events.
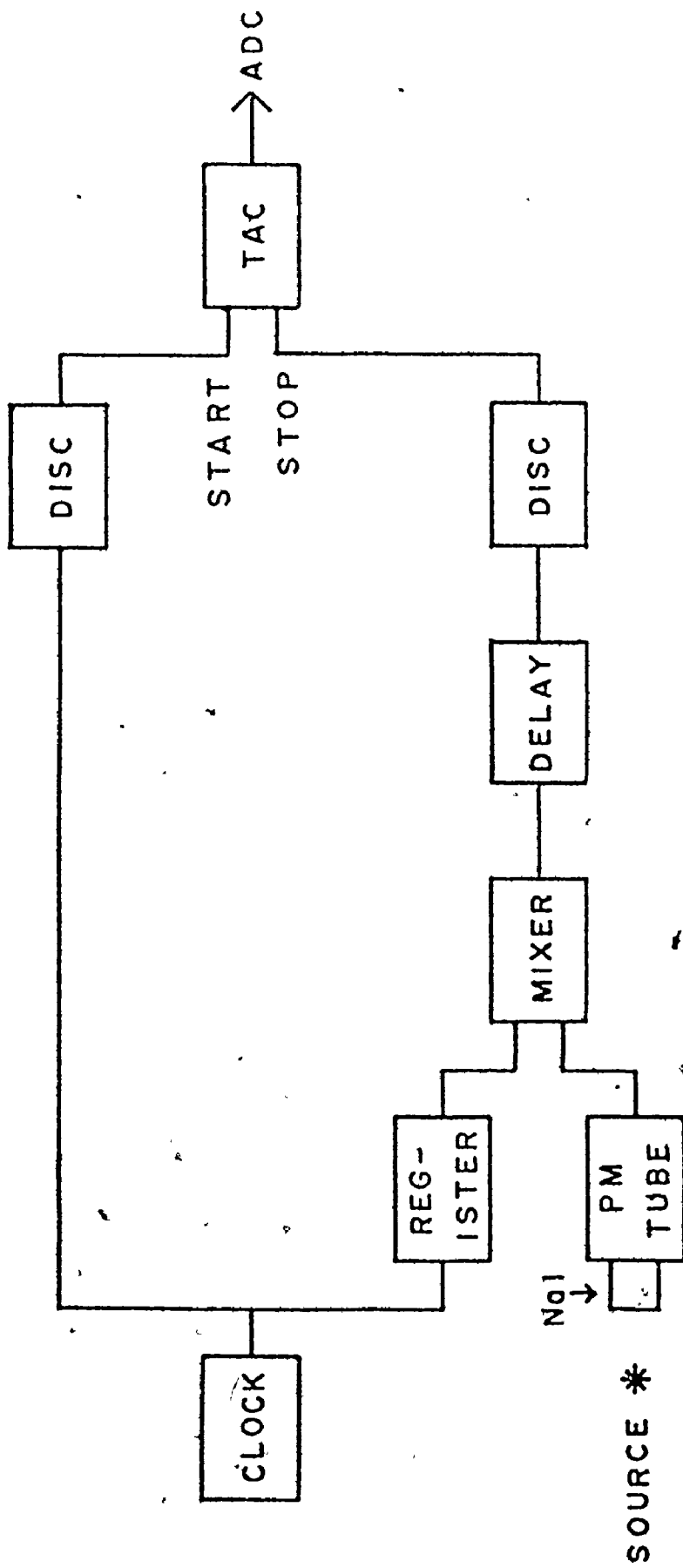
a photomultiplier tube - NaI assembly detecting events
from a radioactive source. These mixed signals provided
the stop timing markers for the time-to-amplitude converter.
The output of the TAC was connected to the ADC of a multi-
channel analyzer which recorded the time-interval distributions
generated for various stop-start fractions of correlated events.
The distributions obtained were corrected for system non-
linearities and are shown in figure 4.5. As can be seen from
the figure, there is a discontinuity in the uncorrelated time-
interval distribution occurring at the position of the peak
corresponding to the correlated events. The magnitude of the
discontinuity is dependent on the fraction of correlated stop-
start events.

The second experimental arrangement which provides
a better simulation of time-interval distribution measurements
is shown in figure 4.6. In this instance, correlated stop-
start events were obtained by conventional crossover timing
of 511-511 keV pair events produced by a ^{22}Na source.
Uncorrelated stop events were obtained from a second, independent
source (^{181}Ta). Crossover timing, with no energy selection
(in contrast to the leading-edge timing of the DPAC experiments),
was chosen to produce a relatively wide distribution of corre-
lated events. The distribution obtained is shown in figure 4.7.

Figure 4.5

TAC Time-Interval Distributions for Various

Correlated Stop-Start Fractions

of A) $1/2$, B) $1/4$, C) $1/8$, D) $1/16$.
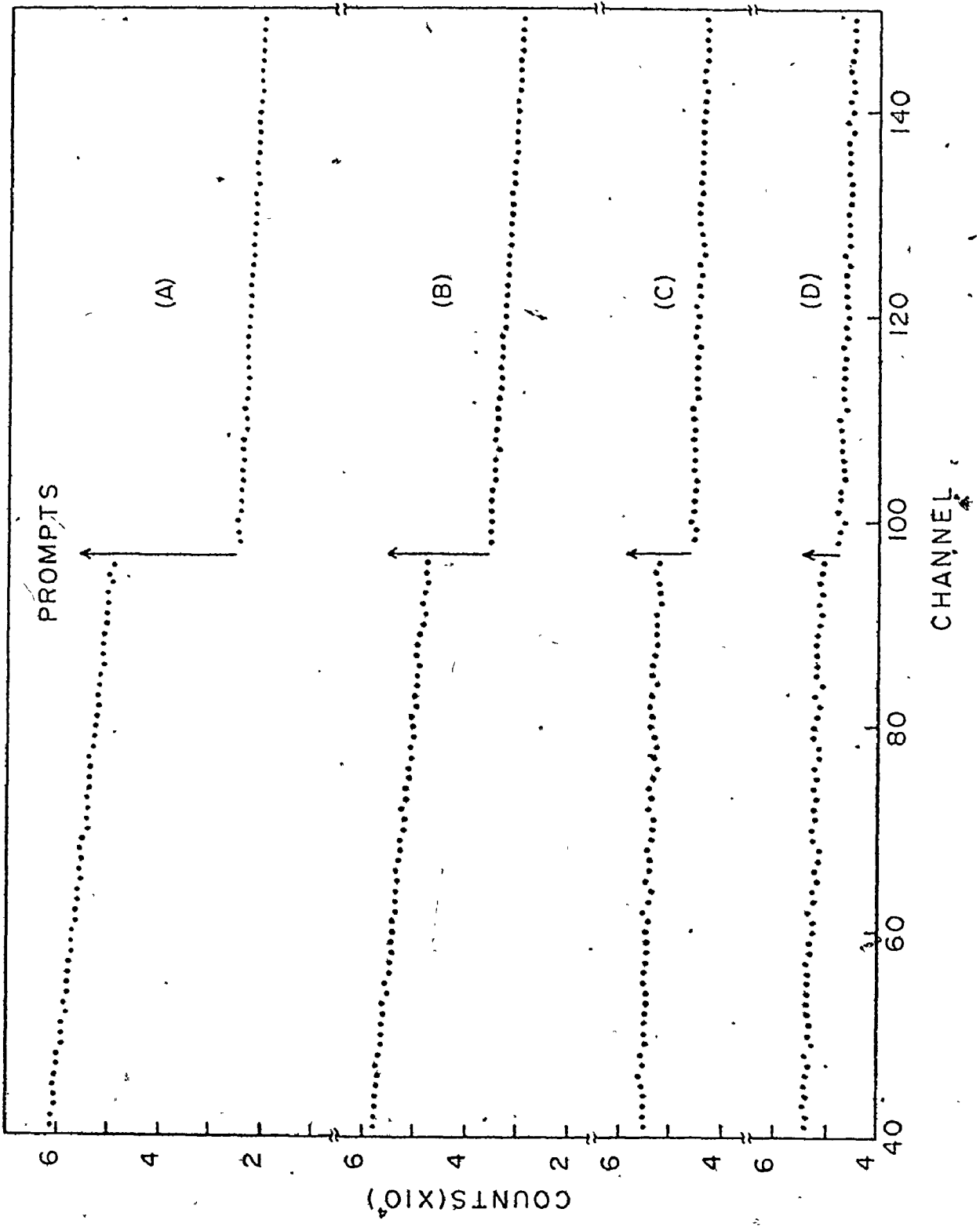
Figure 4.6

Block Diagram of the Electronics

used to produce a typical TAC time-interval distribution
involving a high rate of uncorrelated stop events.
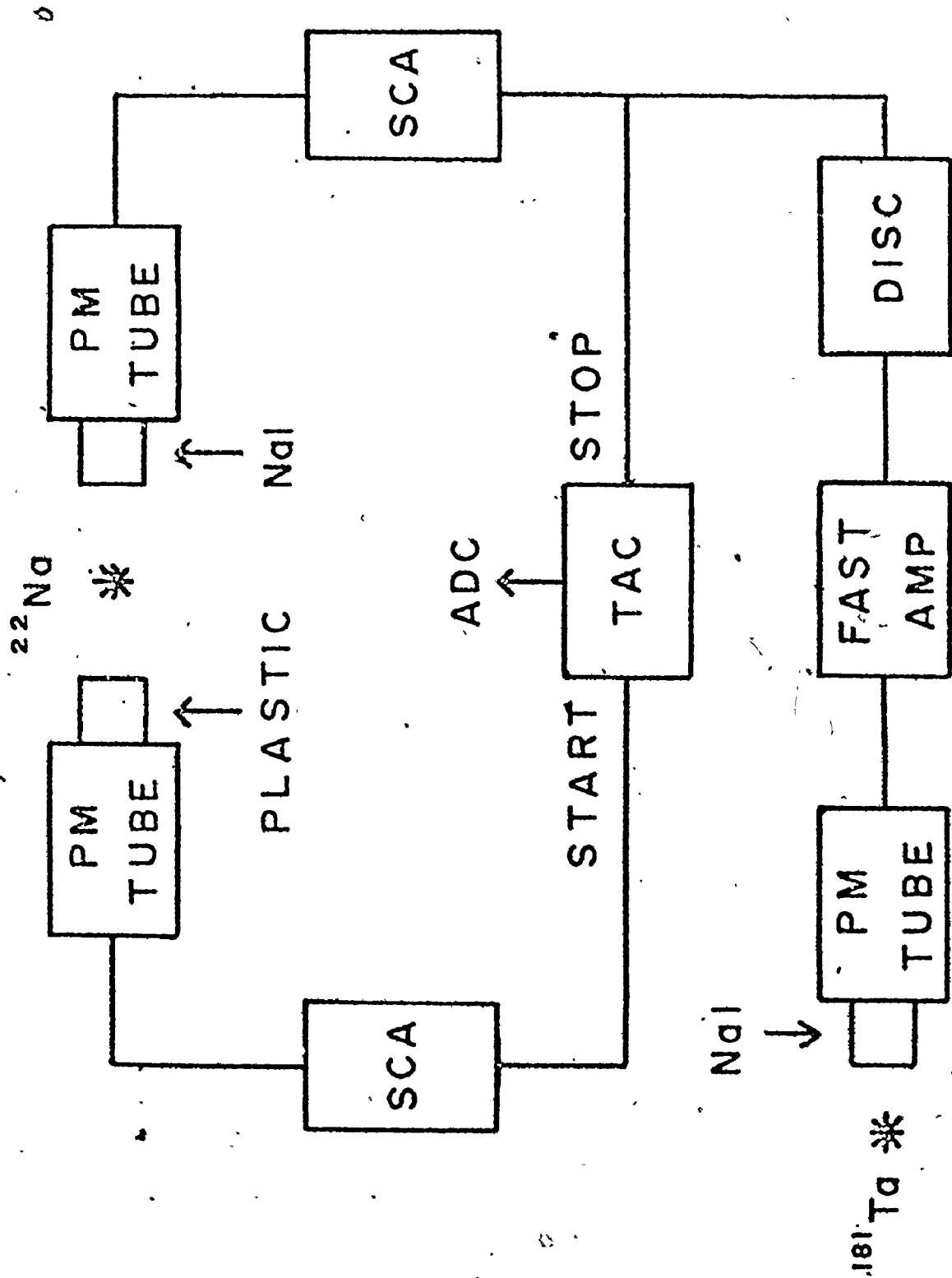
Figure 4.7

TAC Time-Interval Distribution

obtained with the arrangement shown in figure 4.7.

69
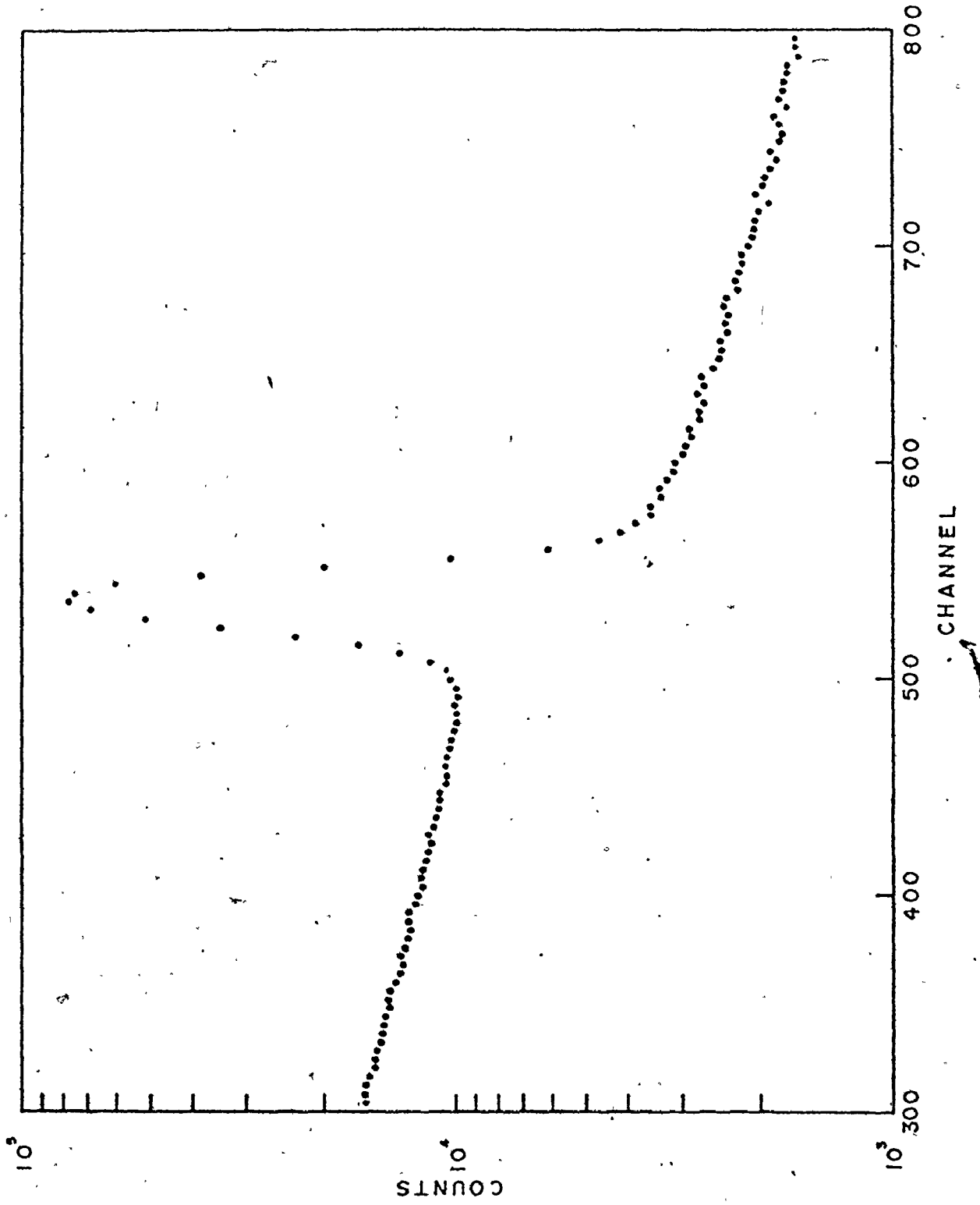
Again, there is a discontinuity in the uncorrelated time-interval distribution occurring about the prompt peak and, as will be demonstrated, the magnitude of this discontinuity varies with the fraction of correlated stop-start events. In this case, as in most experiments, this stop-start fraction is unknown. However, a simple procedure can be followed to obtain this fraction and by means of an iteration method, all uncorrelated stop-start events can be removed from the time-interval distribution. For comparison purposes, a distribution containing only the prompt peak was recorded by removal of the noise source.

C. Method of analysis

In the case where there are only uncorrelated start-stop events, the time-interval distribution is given by (EV72)

$$dN_u(t) = N_s R \; e^{-Rt} dt = N \; e^{-Rt} dt \tag{4.11}$$

where

N_s = start counting rate,

R = stop counting rate.

If a delta function distribution produced by correlated start-stop events is present in the spectrum, the above distribution is modified to

$$N_u(t) = N \; e^{-Rt} \times P \; ,$$

where P is the probability that a correlated start-stop event has <u>not</u> been detected. This is because the TAC can only respond to one stop event per start event. The distribution in figure 4.5 can then be described by

$$N_1(t) = N_1 \, e^{-Rt} \, , \ t < t_p \, , \qquad (4.12)$$

$$N_2(t) = N_2 \, e^{-Rt} = (1 - F) \, N_1 \, e^{-Rt} \, , \ t > t_p \, , \qquad (4.13)$$

where

t_p = prompt peak position

F = the probability that a correlated start-stop event has been detected.

The discontinuity parameter given by

$$\Delta = \frac{N_1 - N_2}{N_1} \, , \qquad (4.14)$$

is shown plotted against the variable F in figure 4.8. The postulate that $F=\Delta$, as derived from equations 4.12 and 4.13, leads to a reduced χ^2 of 0.83 and can be assigned a confidence limit of 93%.

Complications arise in practice however, because the correlated events are themselves distributed in time (figure 4.7). The interaction of the correlated and uncorrelated distributions produces an observed distribution that is not simply a linear superposition of independent distributions.

Figure 4.8

Plot of Experimental Against Theoretical

Background Discontinuity Parameters

as derived from equations 4.13 and 4.14.
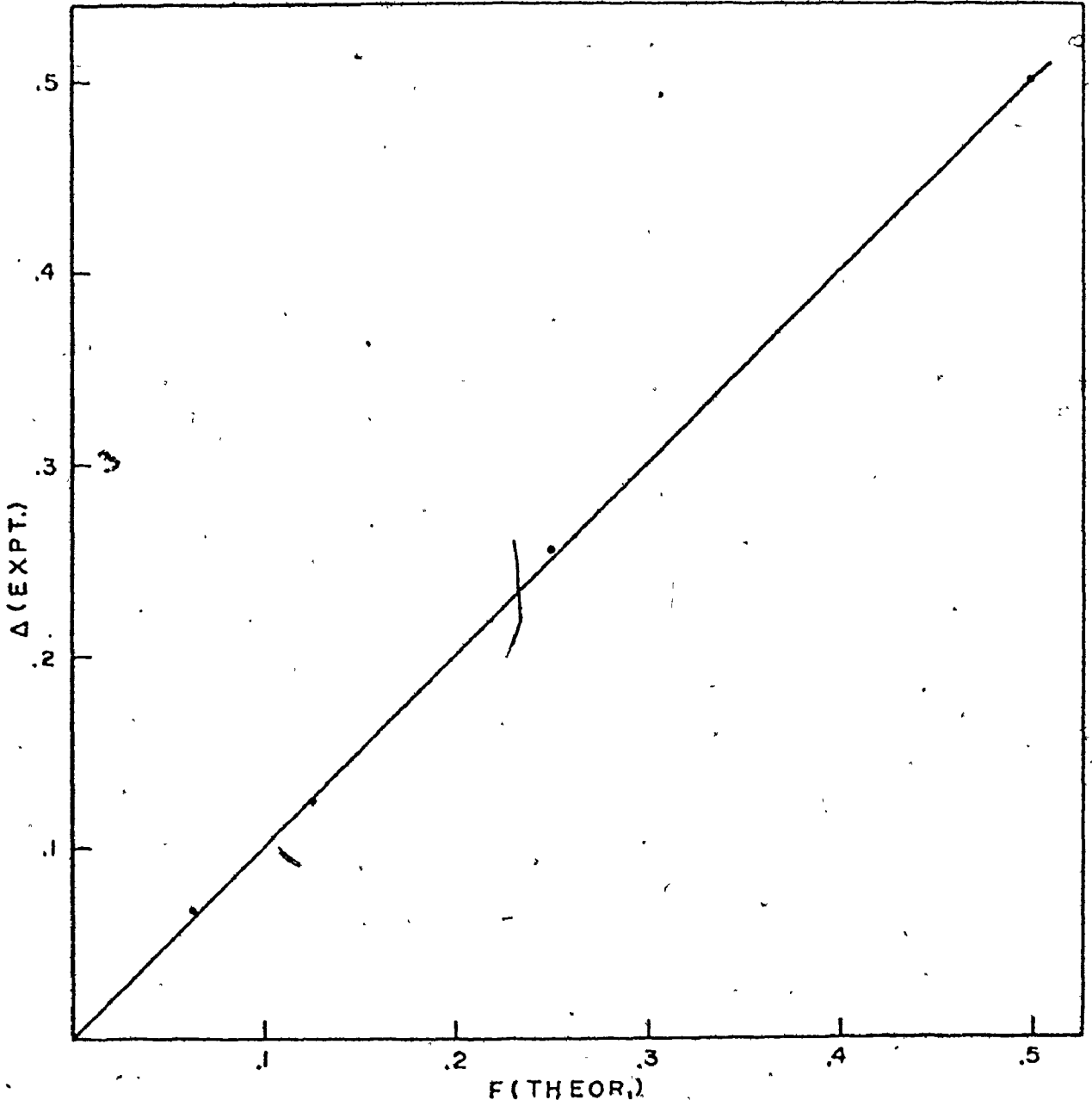
Let C(t) be the correlated time-interval distribution, U(t) be the uncorrelated time-interval distribution and N_s be the start rate. Then for a time-interval 0 to t, the probability that a correlated time interval or prompt event has been detected is

$$F(t) = \int_0^t \frac{C(t')dt'}{N_s} \qquad (4.15)$$

Similarly, the probability that an uncorrelated time interval or background event has been detected is

$$G(t) = \int_0^t \frac{U(t')dt'}{N_s} \qquad (4.16)$$

Since C(t) is weighted by the probability that a background event has not been detected and U(t) is weighted by the probability that a prompt event has not been detected, the resultant observed distribution is given by

$$N(t) = C(t) \left[1-G(t)\right] + U(t) \left[1-F(t)\right]. \qquad (4.17)$$

By using equations 4.15 and 4.16 and noting that

$$U(t) = N_s R \, e^{-Rt},$$

leads to

$$C(t) = N(t)e^{Rt} - RN_s \left[1 - \epsilon \frac{\int_0^t C(t')dt'}{\int_0^\infty C(t')dt'} \right] \qquad (4.18)$$

This shows that in order to determine the correlated distribution, it is necessary to subtract from the observed distribution the contribution from uncorrelated events; but to determine the latter, it is necessary to have a priori knowledge of the correlated distribution.

A suitable approach to follow is to use an iterative method based on the equation

$$C_{j+1}(t) = N(t)e^{Rt} - RN_s \left[1 - \epsilon \frac{\int_0^t C_j(t')dt'}{\int_0^\infty C_j(t')dt'} \right] \qquad (4.19)$$

The parameters R, N_s and ϵ were determined by assuming the background sufficiently away from the neighbourhood of the prompt peak to be of the form $N_i e^{-Rt}$, where $i = 1,2$ corresponds to the regions before and after the prompt distribution respectively (figure 4.9). In particular

$$RN_s = N_1 ,$$

and

$$\varepsilon = \Delta = \frac{N_1 - N_2}{N_1}$$

Figure 4.10   compares the iterative prompt peak, as derived by equation 4.19, with the prompt peak obtained when the source of uncorrelated stop events was removed. These are normalized to equal areas. This method converges very rapidly as the squared differences of consecutive iterations summed over the entire distribution decreased from 10^7 on the first iteration to 10^{-4} on the fifth iteration. In this instance, the first iteration guess was a Gaussian centered at the prompt peak. However, calculations have shown that the first iteration guess has practically no effect on the final iterative prompt peak.

This method was also applied to theoretically generated data based on equation 4.19. The correlated distribution was taken as a Gaussian with FWHM of 14.1 channels and area of 5000 counts. The uncorrelated distribution without the interaction was given by $500\ e^{-t/500}$. Statistics were included by sampling from a Poisson distribution. A goodness of fit parameter as defined by

$$\chi^2 = \frac{1}{N-1} \sum_{i=1}^{N} \frac{(C_i - P_i)^2}{D_i} \qquad (4.20)$$

Figure 4.9

Regions of TAC Background Events

fitted to $N_i e^{-Rt}$.

$N_2 e^{-RT}$

PROMPT

$N_1 e^{-RT}$

N_1

N_2

COUNTS

TIME
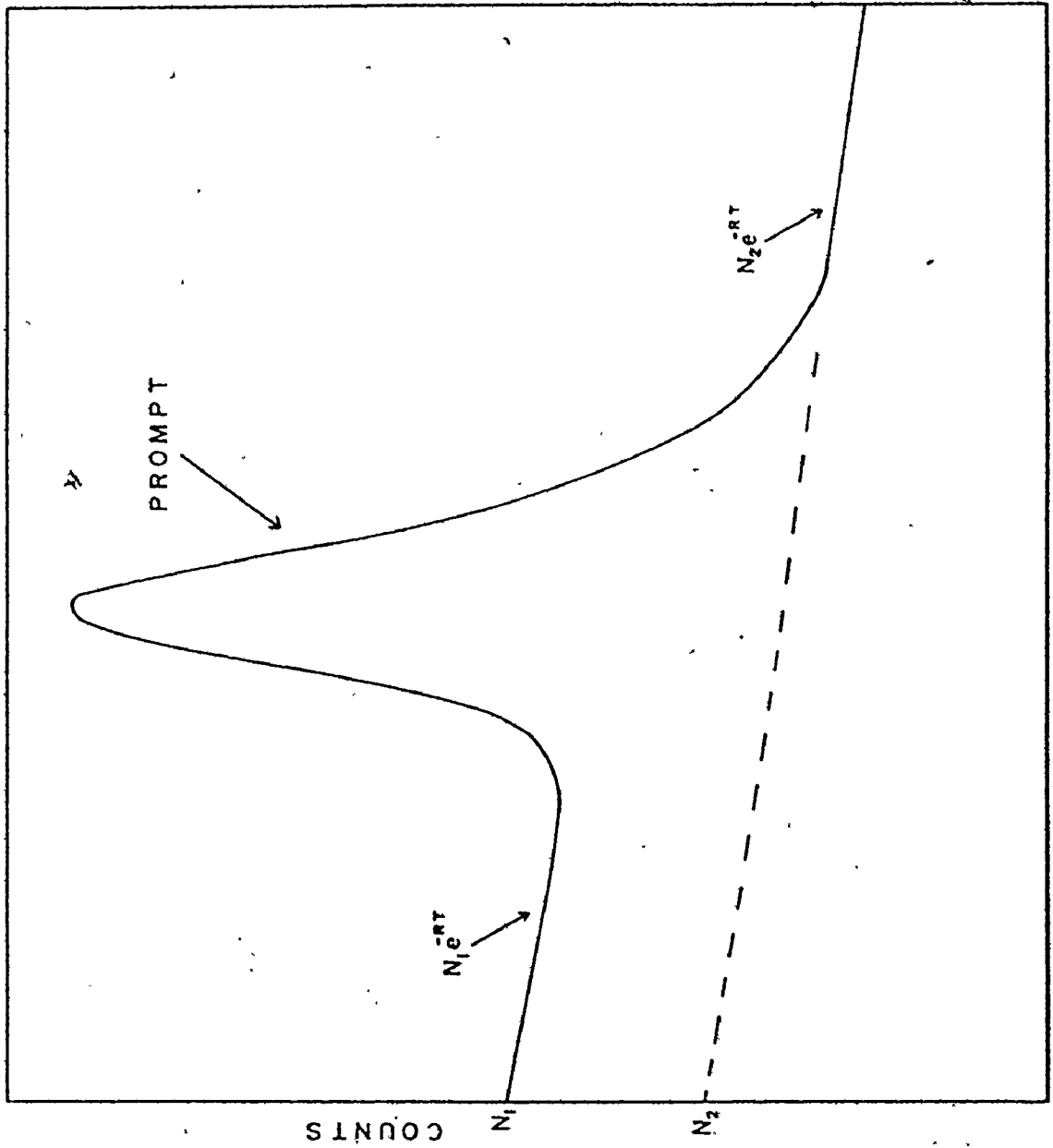
Figure 4.10

Comparison of The Calculated and

Experimental Prompt Curves

The iterative prompt curve (x's) was obtained from figure 4.7
using·equation 4.19 and the experimental prompt (dots) was
obtained when the source of uncorrelated stops was removed.
These curves are normalized to equal area from channels 517 to 557.
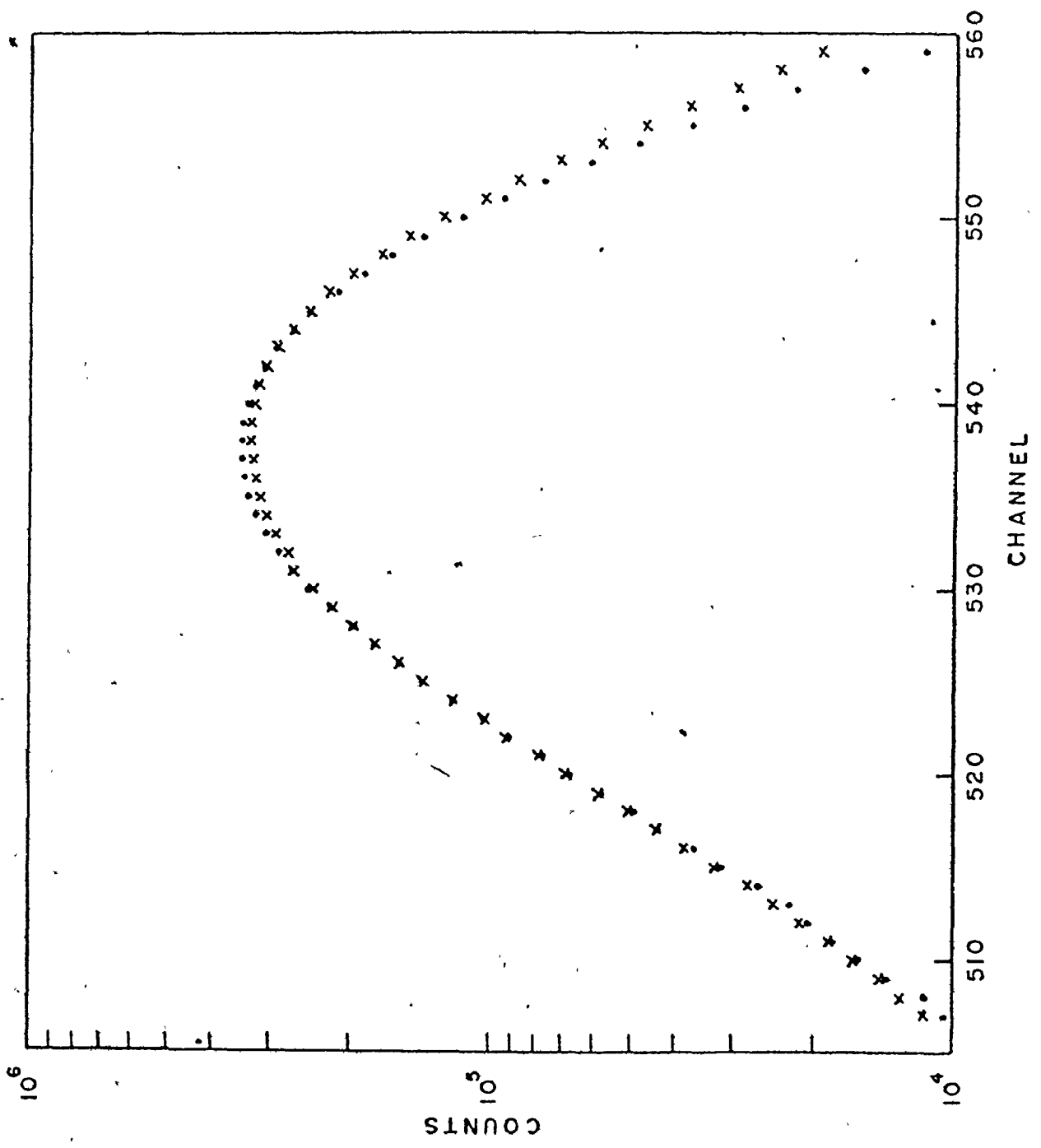
where

C_i = iterative prompt,

P_i = input prompt,

D_i = theoretically generated data,

N = 100 = number of data points,

was calculated to be 1.08 which demonstrates a very good fit within the statistical variation of the data.

In summary, the relation between the uncorrelated time-interval distribution or background $U(t)$ and the correlated time-interval distribution or prompt peak $C(t)$ is

$$C(t) = N(t) - U(t) \left(1 - F \int_0^t C(t')dt'\right) \qquad (4.21)$$

where $N(t)$ is the measured distribution and F is an experimentally determined parameter related to the efficiency of the stop event detector. Under most experimental arrangements, as in the present DPAC studies, the value of F is low enough to allow the use of the conventional background subtraction method without the loss of significant accuracy. The interaction of the correlated and uncorrelated time-interval distributions as shown in equation 4.21 does however become important in measurements in which it is necessary to run under high counting rate conditions in order to acquire adequate data statistics.

CHAPTER 5

The Sources

1. The Choice of ^{181}Ta in PAC Experiments

The nucleus ^{181}Ta has often been chosen as the
probe nucleus in the measurement of electric field gradients
(EFG). It is the product of the β^- decay of ^{181}Hf (LE68)
(figure 5.1) and the 133-482 keV γ-ray cascade of ^{181}Ta
is particularly suited for PAC experiments for several reasons.
What follows is an outline of these reasons and a discussion
of some of the source related problems that could arise in
PAC studies.

(i)   The strength of the EFG-electric quadrupole inter-
action is directly proportional to the nuclear quadrupole
moment. The nucleus ^{181}Ta, which is in a region of strongly
distorted nuclei, has a relatively large quadrupole moment of
2.51 ± 0.15 barns for the 482 keV level (NE73).

(ii)   The 10.8ns half-life of the 482 keV intermediate
level is sufficiently long to enable the perturbing mechanisms
to affect the angular correlation to a degree that is experi-
mentally measurable. Furthermore, nanosecond timing techniques
can be used to measure the perturbation as a function of time
i.e. differential measurements or DPAC.

(iii)   It is known that a radioactive decay may cause

Figure 5.1

Level Scheme of ^{181}Ta

keV

$1/2^-$ 42.5 d

$^{181}_{72}$Hf

(7)

(93)

2 n s $3/2^+$ 619

17.6 μs $1/2^+$ 615

137   133   615
           (99.5)   (0.5)

10.8 n s $5/2^+$ 482

482
(85)

346
(14)

476
(<1)

$9/2^+$ 136

136

$9/2^-$ 60
$7/2^+$ 0

$^{181}_{73}$Ta
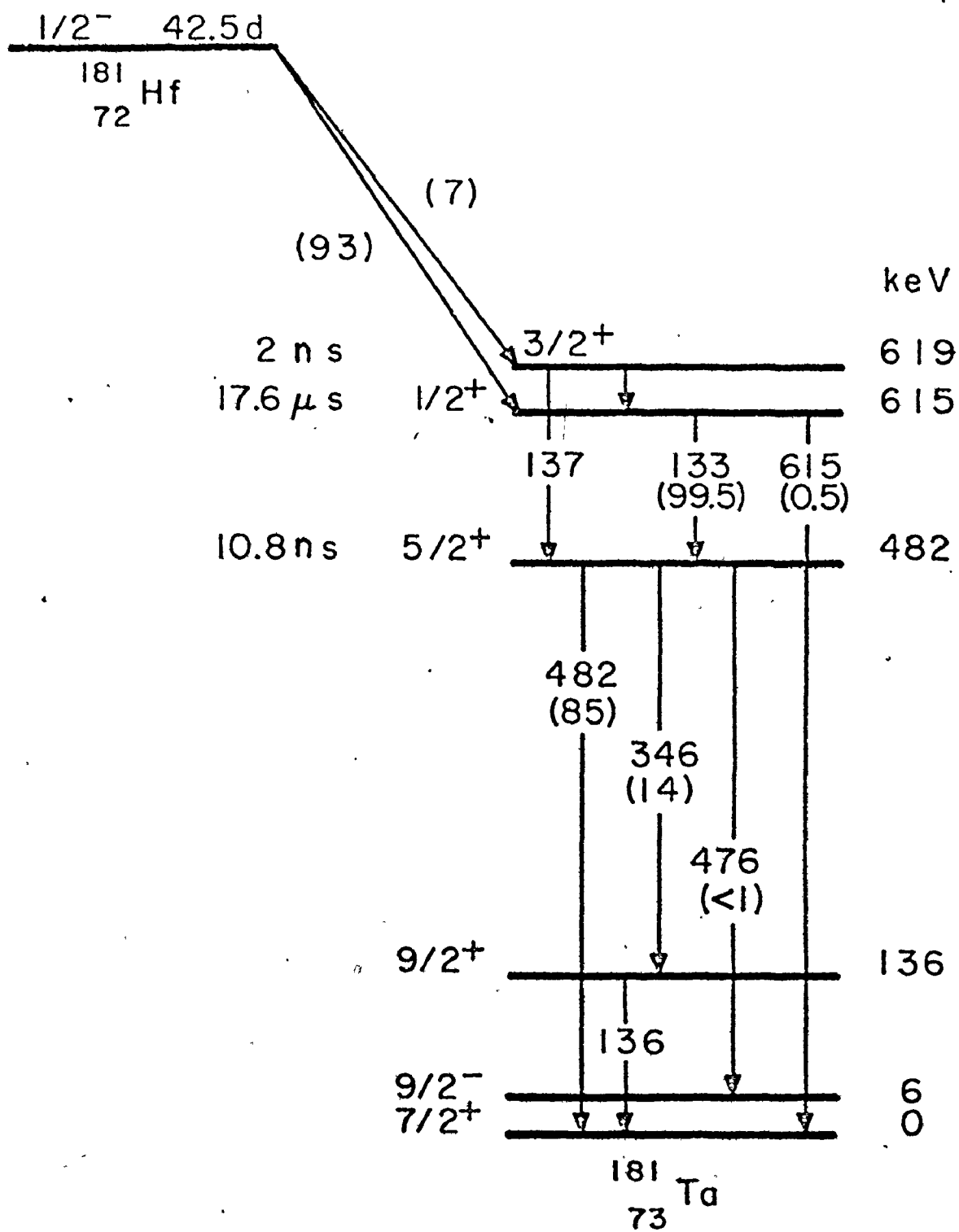
severe disturbances to the atomic electron configuration
of the decaying nucleus. Such after-effects produce time
varying FFG's which may perturb the angular correlation
of successive γ-rays and make the perturbations due to other
external causes such as crystal lattice FFG's difficult or
impossible to measure. This problem, however, is not present
with PAC measurements in this case. After the β^- decay of
^{181}Hf, the daughter nucleus is predominantly in the 615 keV
excited state (93% branching) which has a half-life of 17.6μs.
As the electronic rearrangement of atomic levels is relatively
fast, $\leq 10^{-9}$s even in insulators (TH71), such electronic
after-effects of the β^- decay do not perturb the angular
correlation.

A further possible disturbing influence of the β^- decay
is the recoil of the atom into an environment with an EFG
different from that of a regular lattice site. However, the
recoil energy of 1.6 eV calculated from the endpoint β^-
energy of 408 keV is small in comparison to the $\approx$ 25 eV
that is required to displace an atom from a stable site in
a well-bound solid (SE56).

(iv)   The value of the A_2 coefficient of the unperturbed
angular correlation function for the 133-482 keV cascade is
large : $A_2 = -0.290$ (AV71). This facilitates the measurement
of the perturbation function $A_2 G_2(t)$.

(v) The β^- decay of ^{181}Hf has a half-life of 42.5 days. The collection of data on the same source can then be extended to several weeks without the necessity of re-irradiation. The slowly varying activity of the source reduces the problems of count rate changes such as photo-multiplier tube gain shifts (chapter 3). Chemical preparation or annealing of samples can be performed after irradiation without a significant loss of source activity.

(vi) ^{181}Hf, the parent of ^{181}Ta, is the only long-lived isotope of significant abundance produced by neutron capture in natural hafnium. It is the most abundant isotope of hafnium, 35%, and has a capture cross section of 12.2 barns. Thus, irradiation times are only a few hours (for the McMaster Nuclear Reactor) and background activity due to other isotopes is negligible. Figure 5.2 is a γ-ray spectrum of a source obtained with a Ge(Li) counter in which the main peaks are identified. Those peaks marked with an asterisk are from the 70 day ^{175}Hf isotope. This spectrum was recorded 9 months after source irradiation and consequently the ^{175}Hf activity relative to that of ^{181}Hf had increased by a factor of about 6 from the time of irradiation.

(vii) Interference effects in the angular correlation measurements due to γ-rays that are unresolved by the NaI

detectors are negligible. Specifically,.the relative
intensities of the possible interfering γ-rays (figure 5.2)
in the 133-482 keV coincidence are (AV71)

$$\frac{I(482)}{I(476)} = 200 \quad \frac{I(133)}{I(137)} = 55 \quad \frac{I(133)}{I(136)} = 8$$

The 136 keV γ-ray is emitted after the 482 keV γ-ray and
thus only produces chance background. The 137 keV γ-ray
feeds the 482 keV level to produce coincidences with the 482
keV γ-ray but in only $\approx$ 2% of the total number of coincidences.
In any case, such coincidences result in the same form of
angular correlation function as the 133-482 keV cascade
(with altered A_k coefficients) and do not interfere with the
determination of the critical DPAC parameters.

2. Source Preparation and X-Ray Analysis

The chemical preparation of the sources is a critical
procedure as the DPAC data depends directly on the chemical
environment of the ^{181}Ta atom. In the present work, powder
X-ray photographs of inactive samples were taken to ensure
that the preparations yielded the required compounds. For
K_3HfF_7, an additional X-ray diffractometer measurement was
performed. The active samples were then prepared using the
identical methods. The following descriptions contain
several references to isomorphous zirconium compounds.

Figure 5.2

Ge(Li) γ-Ray Spectrum of a ^{181}Hf Source
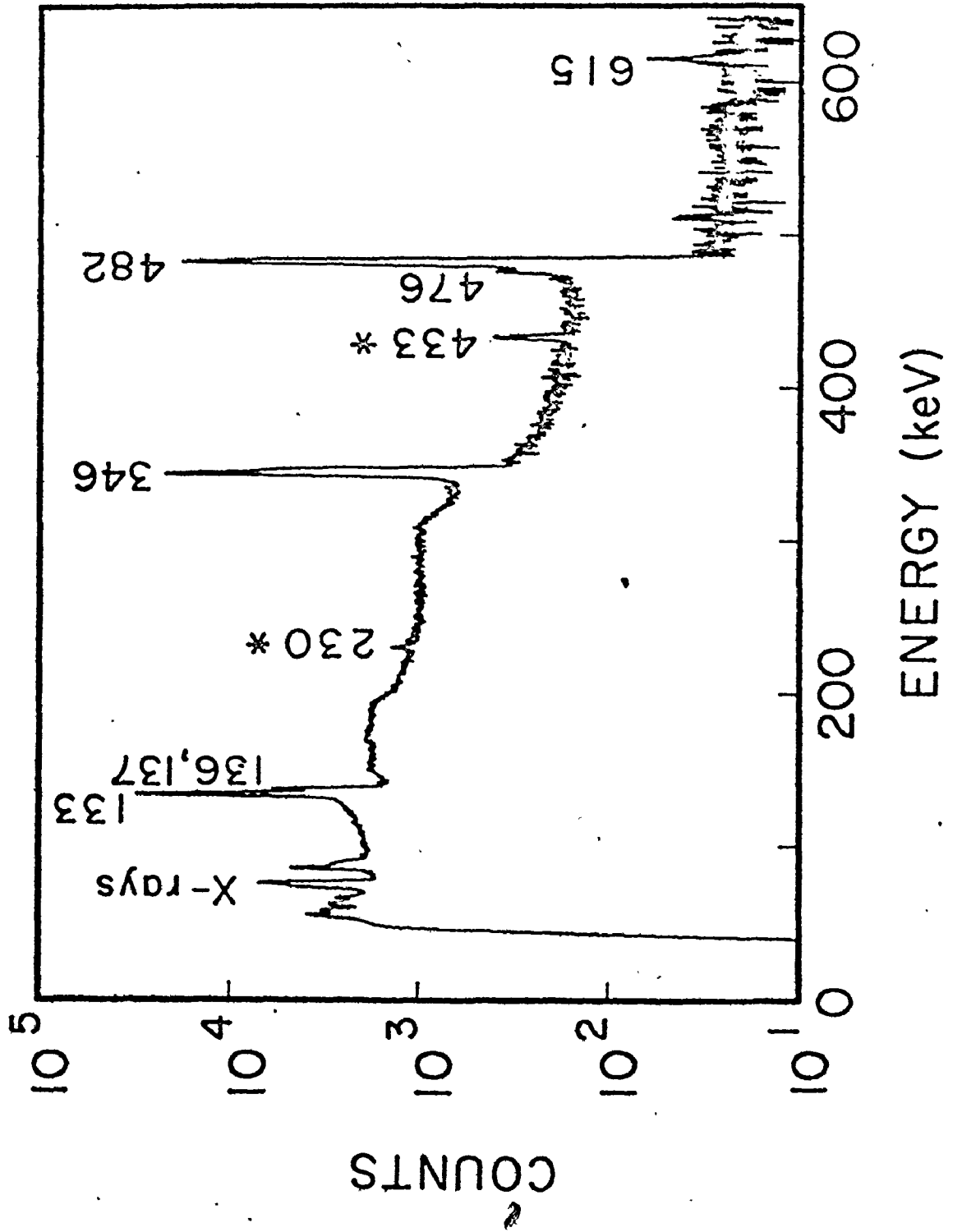
This was a consequence of the large amount of published data available on zirconium as compared to that of hafnium.

A.   The Heptafluorates

The preparation of the heptafluorates was carried out according to the procedure suggested by Paker (BA79) for the isomorphous zirconium compounds. Crystals of $(NH_4)_3HfF_7$ and K_3HfF_7 were grown by first dissolving 200mg of hafnium fluoride in 4mℓ of hot water and 0.2 mℓ of hydrofluoric acid. A 30% solution containing a large excess of ammonium fluoride or potassium fluoride was added to this. The resultant cloudy solution was cleared by the addition of 1 mℓ of water and 0.2 mℓ of hydrofluoric acid. The crystals formed slowly from this solution while it was cooled over-night. After filtering and drying, the crystals were sealed in 5 mm diameter glass vials. These vials fitted into the narrow extension at the bottom of the liquid helium cryostat.

Table 5.1 compares the d-spacings obtained from the X-ray powder photographs of an inactive sample of $(NH_4)_3HfF_7$ with those of the isomorphous zirconium compound obtained from the ASTM powder X-ray file index (AS69, card no. 7-24). The errors have been estimated from the calibrated template used to measure directly the d-spacings from the powder photograph. The measured spacings are in good agreement

TABLE 5.1

X-Ray Analysis of $(NH_4)_3HfF_7$

d-spacing ($\overset{\circ}{A}$)

Experimental	$(NH_4)_3ZrF_7$[†]
5.4 ± 0.1	5.44
4.7	4.71
3.30 ± 0.05	3.33
2.82 ± 0.02	2.84
2.62	–
2.57	–
2.34	2.36
2.15	2.16
2.10	2.11
1.91 ± 0.01	1.92
1.80	1.81
1.66	1.67
1.58	1.59
1.56	1.57
1.48	1.49
1.43	1.44
1.41	1.42
1.35	1.36

[†] ASTM X-Ray Powder File No. 7-24

with those of the zirconium compound which is expected to be slightly expanded from the isomorphous hafnium compound. Two weak lines on the photograph at 2.62 Å and 2.57 Å remained unidentified.

Initial preparations of K_3HfF_7 did not produce clean samples as noted by the large number of lines in the X-ray photograph, possibly due to the formation of other fluorides such as K_2HfF_6. This problem was overcome by using a much larger excess of potassium fluoride, 200%, in the preparation as compared to 100% excess of ammonium fluoride in the $(NH_4)_3HfF_7$ preparation. Figure 5.3 shows the X-ray analysis of the sample and table 5.2 lists the results in comparison with the isomorphous zirconium compound (AS69, card no. 10-372). The X-ray radiation was that of the copper K_α line (λ = 1.54178Å) and the d-spacings were calculated from the measured 2θ diffraction angles by the Bragg formula

$$d. = \frac{0.77089}{\sin\left(\frac{2\theta}{2}\right)}$$

The identification of all the major lines in the spectrum attests to the authenticity of the sample.

B. Hafnium Acetylacetonate

Two methods of sample preparation were used. In the first, a sample was prepared by irradiating commercial[†] Hf(acac)$_4$

[†] Obtained from KEK Laboratories, Inc., Plainsview, N.Y.

Figure 5.3

Powder X-Ray Diffractometer Spectrum

of K_3HfF_7

INTENSITY (arbitrary units)
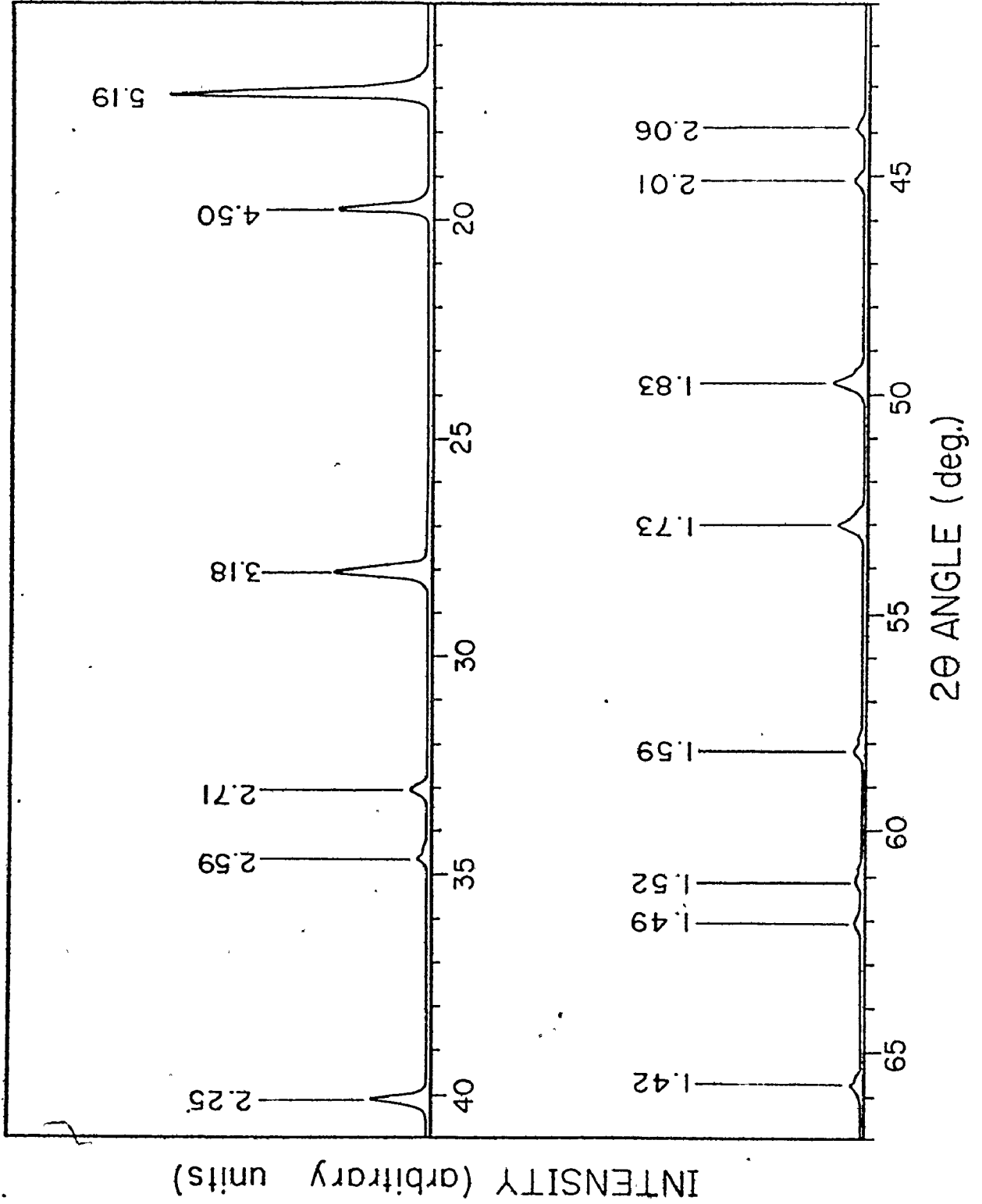
2θ ANGLE (deg.)

TABLE 5.2

X-Ray Analysis of K_3HfF_7

2θ Scattering Angle (deg)	Spacing	
	$d(\overset{O}{A})$ calculated	$d(\overset{O}{A})$ K_3ZrF_7†
17.10 ± 0.05	5.185 ± 0.015	5.190
19.75	4.495 ± 0.012	4.495
28.05	3.181 ± 0.006	3.177
33.05	2.710 ± 0.004	2.710
40.10	2.249	2.247
43.9 ± 0.1	2.062	2.062
45.1	2.010	2.009
49.7	1.834	1.835
53.0	1.728	1.729
58.1 ± 0.2	1.588	1.589
61.1	1.517	1.519
62.1	1.495	1.498
65.8	1.419	1.421

† ASTM X-Ray Powder File No. 10-372

for 2h in the McMaster Reactor at a thermal flux of $2.6 \times 10^{12} n/cm^2 s$. The flux was recorded in order to compare with previous DPAC studies of possible irradiation effects on this compound (BF69). This source was vacuum sealed in a 2mm diameter glass vial.

A second sample was prepared by incorporating radio-hafnium in the complex by synthesis of the acetylacetonate from $HfOCl_2$ according to the procedure of Larsen et al. (LA53). A 25% excess of the theoretical amount of acetylacetone was added to a cold 0.1 M solution of $HfOCl_2$ keeping the pH at 1.5 by the addition of a dilute sodium carbonate solution. Crystals of $Hf(acac)_4$ formed slowly from the cooled solution over a period of 1 1/2 days. The crystals were then washed and filtered and vacuum sealed in a 2mm diameter glass vial.

A comparison of the X-ray photographs showed that the diffraction-patterns for the commercial and synthetic samples were identical in all respects except line width. The commercial sample exhibited greater line broadening than did the one synthesized from the oxychloride. The d-spacings for 15 lines were determined and were all essentially in agreement with those calculated for the monoclinic structure of the isomorphous $Zr(acac)_4$ compound with lattice parameters as given by Silverton and Hoard (SI63). The results are

shown in Table 5.3. The calculated values were obtained from the lattice parameters

$a = 19.86 \overset{O}{A}$ $b = 8.38 \overset{O}{A}$ $c = 14.14 \overset{O}{A}$ $\beta = 102^\circ 50'$ and

the monoclinic d-spacing formula (AZ58)

$$\frac{1}{d^2} = \frac{\dfrac{h^2}{a^2} + \dfrac{\ell^2}{c^2} - \dfrac{2h\ell}{ac} \cos \beta}{\sin^2 \beta} + \frac{k^2}{b^2}$$

In some instances, more than one set of h k ℓ values resulted in similar d-spacings as indicated in Table 5.3. The calculated values are systematically larger than the experimental values as would be expected for the slightly expanded $Zr(acac)_4$ compound. It can be concluded from these X-ray results that an authentic sample of $Hf(acac)_4$ was synthesized.

TABLE 5.3

X-Ray Analysis of $Hf(acac)_4$

d-spacing (Å)

Experimental Hf(acac)$_4$	Calculated Zr(acac)$_4$	Plane h k ℓ
9.6 ± 0.3	9.68	200
7.7 ± 0.2	7.69	110
7.0 ± 0.1	6.89	002
6.3	6.34, 6.32	210, 20$\bar{2}$
5.3	5.32	012
5.1	5.11	202
4.85 ± 0.05	4.92	112
3.95	3.98	12$\bar{1}$
3.75	3.80	113, 22$\bar{1}$, 312
3.55	3.58, 3.51	022, 320
3.45	3.45, 3.49	122, 22$\bar{2}$
†2.65 ± 0.02	2.64	323
2.32	2.34	133
†2.24	2.26	233
2.11	2.13	534

† Wide lines, possibly unresolved doublets.

CHAPTER 6

Data Analysis

1. The Fitting Procedure

The daily time spectra corresponding to the two emission angles were summed and normalized (sections 6.2, 6.3) and corrected for the contribution from random events to yield the true time spectra $N(\pi,t)$ and $N(\frac{\pi}{2},t)$. A typical daily run is shown in figure 6.1. The perturbation function was then calculated from these spectra according to

$$A_2G_2(t) = 2 \frac{N(\pi,t) - N(\pi/2,t)}{N(\pi,t) + 2N(\pi/2,t)} \tag{6.1}$$

which is derived from equation 2.3. A plot of this function for $Hf(acac)_4$ is shown in figure 6.2.

The denominator of equation 6.1 should yield the lifetime of the 482 keV intermediate level providing that the randoms have been subtracted correctly. This served as a check for correct background subtraction and lead to a precise re-evaluation of the 482 keV level lifetime (section 6.5). The interaction of the correlated and chance time interval distributions as discussed in chapter 4 was not seen in any of the data because of the low rate of chance events which accounts for approximately 5% of the count rate at the maximum in the spectra.

Figure 6.1

Examples of the DPAC Data

obtained from the synthetic sample of $Hf(acac)_4$ in a one day run.
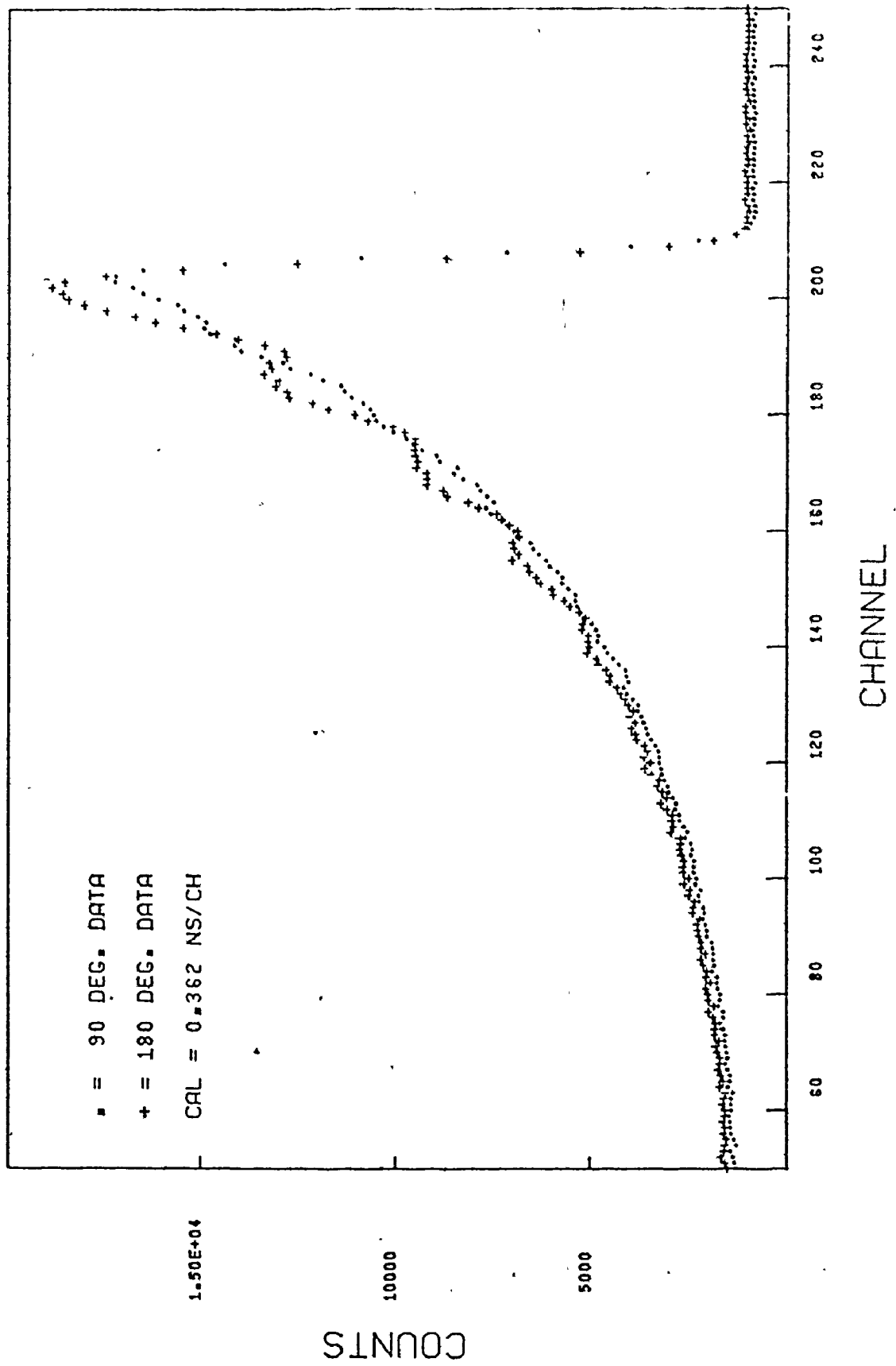
Figure 6.2

$A_2G_2(t)$ for $Hf(acac)_4$.

Curve A was obtained for the synthesized sample and
curve B for the commercially prepared sample.
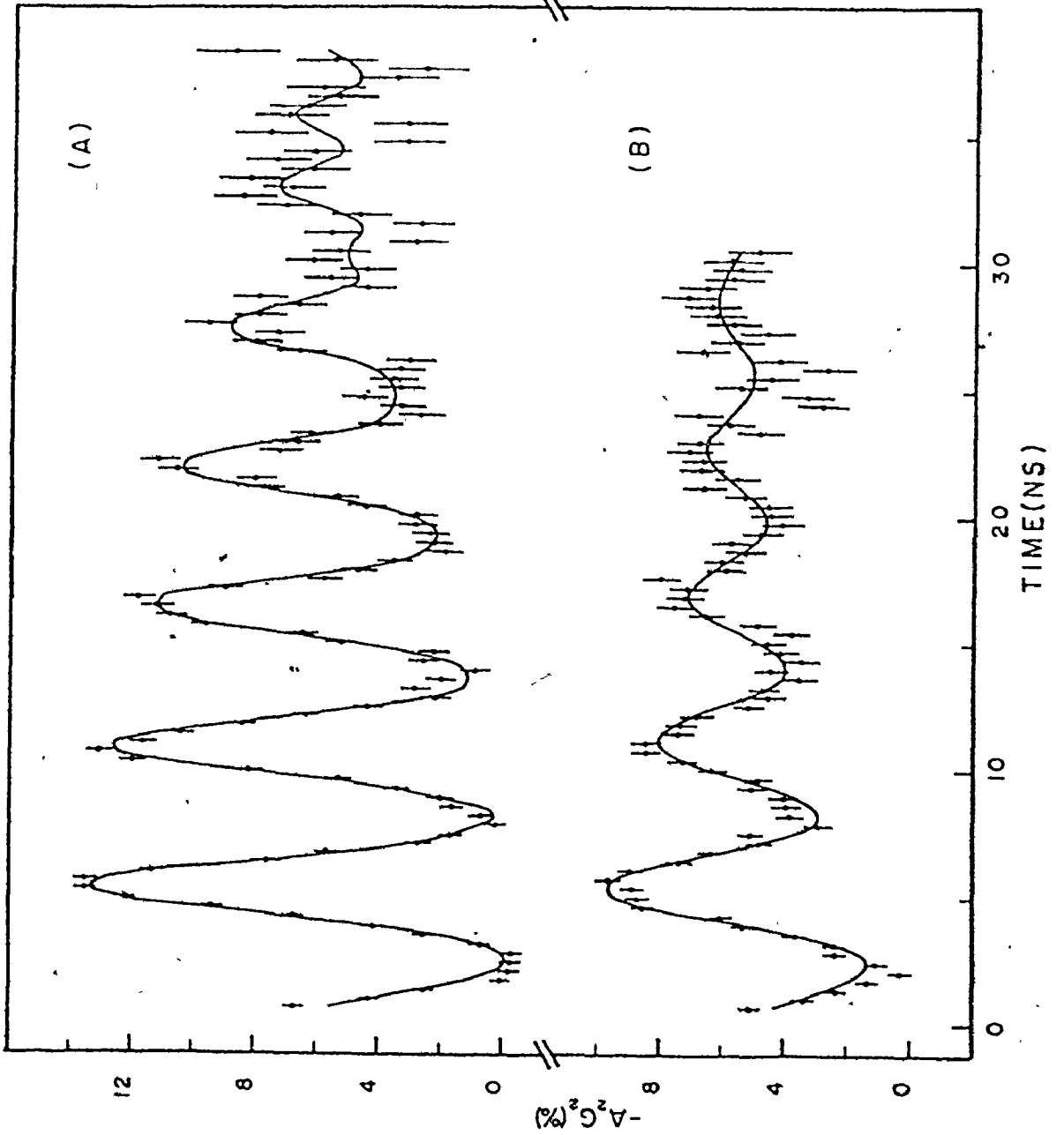
The background was calculated in the area of the spectrum beyond the correlated distribution and it was assumed to be constant throughout the spectrum. For a typical stop count rate of 20000/s, the fractional decrease in the background over a 100 ns time range is only 2×10^{-3}. It was found that the fitting of the background to exponential or linear functions did not alter the values of the derived DPAC quantities.

All the DPAC parameters were determined by a least squares fit to the perturbation function calculated in equation 6.1. The fitting took into consideration the distribution of FFG's and the finite time resolution of the system. A typical computer fitting run was initiated by calculation of the Fourier power spectrum of the perturbation function in order to determine a starting value of the fundamental frequency ω_1 for the least squares fit. This spectrum was calculated by numerical integration of the equation

$$P(\omega) = \left| \int_o^T A_2 G_2(t) \exp(i\omega t) dt \right|^2 \tag{6.2}$$

where T is the time span over which statistically significant data had been obtained, generally 30 to 50 ns. Figure 6.3 shows the power spectra of the perturbation functions shown

Figure 6.3

Fourier Power Spectra for Hf(acac)$_4$

of the perturbation functions shown in figure 6.2.
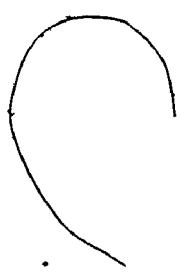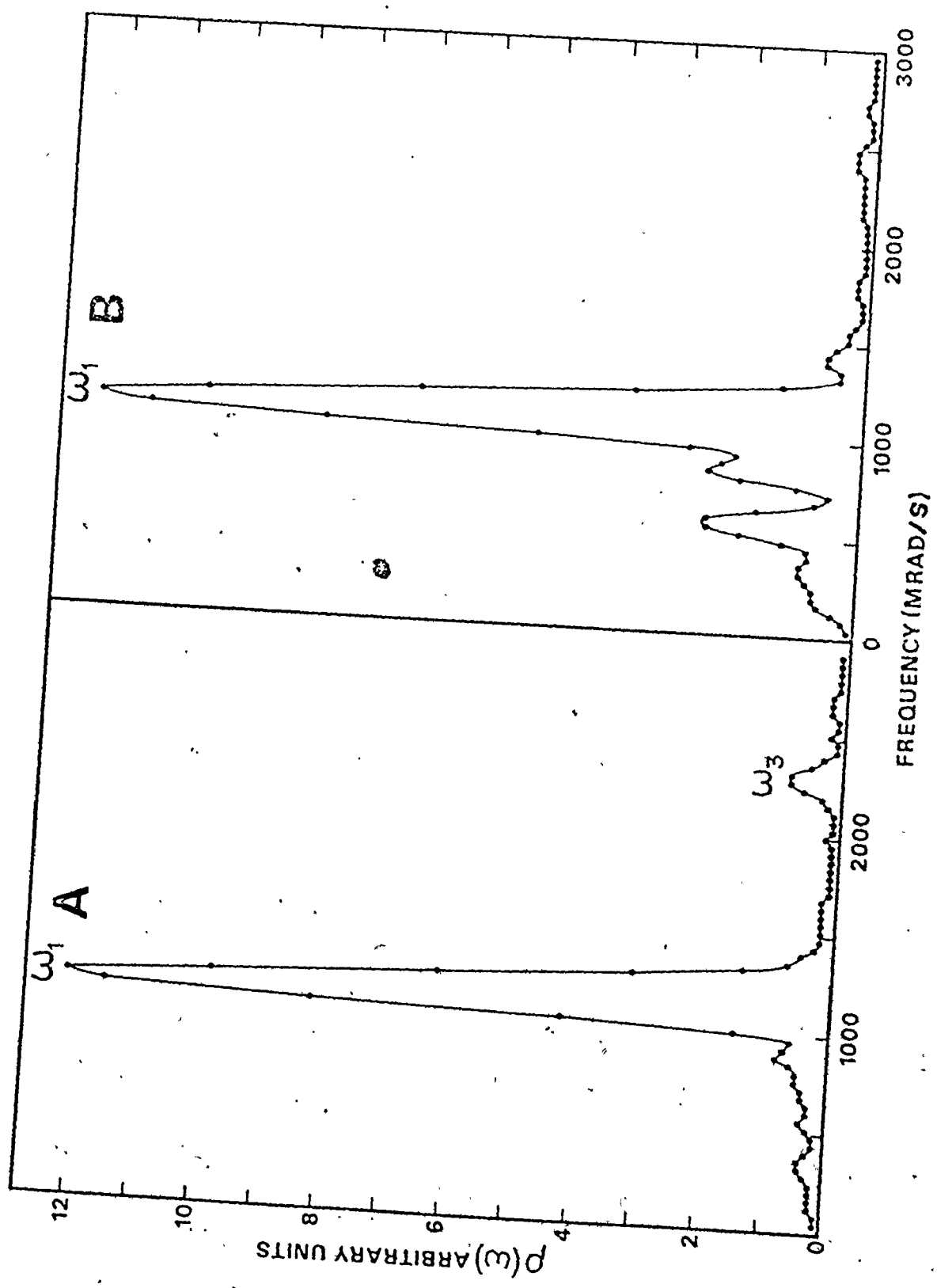
in figure 6.2. The power spectra method has been used.
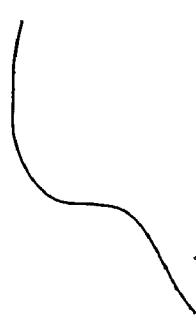directly for the determination of DPAC parameters
(e.g. GA69a) but in the present case it was predominantly
used in a qualitative analysis of the data and as a starting
point for the least squares fit.

As an example of the fitting procedure, consider
fitting data to a static EFG with a Gaussian frequency
distribution as given by equation 2.15. Having determined
a starting value for the fundamental frequency ω_1, the
asymmetry parameter η was randomly chosen and the remaining
frequencies ω_2 and ω_3 and the amplitude coefficients a_{2n} were
calculated from equations 2.12 and 2.13. The d.c. coefficient
a_{20} was left as a free parameter for reasons given in the
next section. A value for the EFG frequency spread δ was
assumed and the perturbation function of equation 2.15 was
then completely specified. Before comparison with the data,
this function was numerically convolved (equation 4.1) with
the time response curve of the system as determined in
section 3.7. This method did not then require an assumption
of the shape of the response curve. Finally, a variable
delay parameter was used to shift the data in time since the
t=o position did not necessarily fall exactly on the first
channel position of the data under analysis. This convolved

and shifted spectrum X_i was compared to the N data points of variance σ_i^2 and a goodness of fit parameter, the reduced χ^2, was calculated,

$$\chi^2 = \sqrt{\frac{1}{N-v} \sum_{i=1}^{N} \frac{(X_i - Y_i)^2}{\sigma_i^2}} \qquad (6.3)$$

Here, v is the number of free parameters which in this case is 5 : A_2, η, ω_1, a d.c. term and a delay parameter. The fitting program varied these parameters and repeated the above procedure in order to minimize χ^2. The program used a powerful iterative method with rapid convergence which is based upon a technique developed by Davidon (DA59) and later simplified and improved by Fletcher and Powell (FL63). The details and interpretation of the method including a firm theoretical basis are given in these references.

Because the nonlinearities of the TAC-ADC system as measured by the DNL curve were found to be relatively small, < 2%, correction of the data in a few test cases did not significantly alter the derived DPAC parameters. As a result, the correction of the data via the DNL curve was not performed except in the case of the precise lifetime measurement (section 6.5).

2. Time Zero Shifts

The data analysis required the addition of several
time spectra from each of the daily runs. These spectra in
general had different t=o positions and thus had to be
aligned properly before summation. Mis-alignment would
produce a distorted picture of the perturbation function.
The causes of the different time zero points originated in
two areas: zero shifts in the daily spectra all of which were
acquired with the same start-stop detector combination and
shifts in the spectra acquired with different start detectors.
The former shifts have been well studied by Wagner et al.
(WA69) and are due primarily to perturbations of the photo-
multiplier tube by magnetic fields and influences to the
detector electronics and associated timing discriminators by
temperature changes. The temperature effects were minimized
by performing all experiments in an air-conditioned room and
using a forced-air cooling cabinet for the electronics.
The magnetic field perturbations were checked by measuring
the prompt time response curve of the system with and without
mu-metal magnetic shields covering the photomultiplier tubes
and for various orientations of the tubes with respect to the
earth's magnetic field. No shifts in the prompt curve were
observed.

The latter shifts (in spectra acquired with different start detectors) were minimized by aligning in time the prompt curves acquired with the two detector combinations by the insertion of appropriate cable delays in the start side of the TAC. These precautions reduced the overall shifts to less than 0.5 ns. The problem of these remaining shifts was treated as follows.

The region of the measured time spectrum near time zero is a convolution of the lifetime curve of the intermediate level and the time response function ($\approx$ Gaussian) of the system. For the case of a lifetime that is long compared to the response width ($\frac{\tau}{\sigma} \approx 11$ for the present data), the lifetime curve may be approximated by a step function of height N_0 at time t=o. The measured spectrum is then

$$M(t) = \frac{1}{\sqrt{2\pi\sigma}} \int_o^\infty N_0 \exp\left[\frac{-(t-t')^2}{2\sigma^2}\right] dt'$$

$$= \frac{N_0}{2} (1 + erf \frac{t}{\sqrt{2\sigma}}) \qquad (6.4)$$

The maximum value of M(t) is M(∞) = N_0 and the value at t=o is M(o) = $\frac{N_0}{2}$. Thus, the time zero point occurs at one-half of the peak height of the leading edge of the time spectrum. This point was found for each daily spectrum, all

of which were then shifted to a common time zero point before summation. The computer shifting program used linear interpolation of the data between channels as the shifts were generally only fractions of a channel in magnitude.

A check of the method was performed by calculating the shifts necessary to minimize the residual

$$\sum_i \frac{(X_i-Y_i)^2}{X_i+Y_i}$$ for any two normalized spectra X and Y of the same

angle. It was found that these shifts were in excellent agreement with those determined by the half-height method.

3. Normalization of the Coincidence Spectra

The calculation of the perturbation function by equation 6.1 assumes a proper relative normalization of the π and π/2 coincidence spectra. If for some reasons such as unequal source-detector distances, unequal detector efficiencies or different energy windows (in the γ energy selection by the SCA's), the spectra are not normalized, then the calculated function becomes

$$C(t) = 2 \frac{1-M+A_2G_2(t)\ (1+M/2)}{1+2M+A_2G_2(t)\ (1-M)} \tag{6.5}$$

where M is the normalization factor of the original N' (π/2,t) data i.e.

$$N(\pi/2,t) = M\ N'(\pi/2,t) \tag{6.6}$$

This means that due to experimental conditions the probability of a coincidence at 90° has been increased or decreased by a factor M relative to a coincidence at 180°. Note that $C(t) \rightarrow A_2G_2(t)$ as $M \rightarrow 1$. Now, in the denominator of $C(t)$, $1 + 2M >> |A_2G_2(t)(1-M)|$ since $A_2G_2(t) < 1$ and $M = 1$ for properly arranged experiments. Therefore equation 6.5 becomes

$$C(t) = 2 \frac{1-M}{1+2M} + \frac{M+2}{2M+1} A_2G_2(t) \qquad (6.7)$$

This shows that for an incorrect normalization, the form of the function $C(t)$ from which the experimental parameters are obtained is the same as $A_2G_2(t)$ while only the amplitude, $\frac{M+2}{2M+1}$, and the d.c. level, $2 \frac{1-M}{1+2M}$, are changed.

Equation 6.7 was tested by performing least squares fits to DPAC data in which the normalization factor M was altered from fit to fit. A d.c. parameter and A_2 were allowed to vary freely. It was found that these fits yielded identical values for the asymmetry parameter η, the fundamental frequency ω_1 and the frequency distribution width δ whereas the d.c. and A_2 parameters varied with M. Table 6.1 lists the results along with the values predicted by equation 6.7. The agreement is good even for M as large as 1.5. The amplitude variations of A_2 are rather insensitive

TABLE 6.1

The Effects of Spectra Normalization

M	Fitted Values				Predicted Values	
	d.c. level	$\dfrac{A_2}{A_2'}$ †		$2\ \dfrac{1-M}{1+2M}$		$\dfrac{M+2}{2M+1}$
0.90	0.070	1.037		0.071		1.036
0.95	0.030	1.019		0.034		1.017
0.98	0.009	1.007		0.014		1.007
1.00	-0.004	1.0		0.0		1.0
1.02	-0.019	0.9922		-0.013		0.9934
1.05	-0.037	0.9824		-0.032		0.9839
1.10	-0.067	0.9641		-0.063		0.9688
1.50	-0.254	0.8343		-0.250		0.8750

† $A_2'=A_2$ at M = 1.00

to M and would generally be hidden by experimental uncertainty while the d.c. shifts in C(t) are comparable to the changes in the a_{20} term of $G_2(t)$. For example, a 2% change in M from unity results in a d.c. shift of 0.013 which spans about 20% of the entire range of a_{20} since, as η changes from 0 to 1, a_{20} changes from 0.200 to 0.258 (BE69).

Since equation 6.7 properly predicts the effect of spectra normalization on the calculation of $A_2G_2(t)$, a d.c. parameter was included in the least squares fitting of the DPAC data. The normalization factors in the present work were calculated by comparing the background levels in the π and π/2 spectra. These levels did·not differ by more than 3% for any sample.

4. The Effect of EFG Distributions on the Calculation
    of DPAC Parameters.

The effect of an EFG distribution on the measured perturbation function is usually taken into account by allowing for a distribution of interaction frequencies (chapter 2) and if this distribution is assumed to be Gaussian, the perturbation function takes the form given in equation 2.15

$$\overline{G_K(t)} = a_{ko} + \sum_n a_{kn} \exp\left[-(\delta_n\omega_nt)^2/2\right]\cos\omega_nt \qquad (2.15)$$

It is a common practice in the data analysis to assume that the individual frequencies ω_n have an identical distribution width i.e. $\delta_1=\delta_2=\delta_3=\delta$. However, the ω_n are strongly correlated as shown in equation 2.13 and cannot be varied independently. This problem was pointed out by Forker (FO73) who, instead of varying the ω_n, assumed Gaussian distributions in the EFG components V_{XX}, V_{YY} and V_{ZZ} :

$$P(V_{XX}) = \frac{1}{\sqrt{2\pi}\Delta_{XX}} \exp\left[-(V_{XX}-V_{XX}^o)^2/2\Delta_{XX}^2\right] \qquad (6.8)$$

and similar expressions for $P(V_{YY})$ and $P(V_{ZZ})$.

Starting from a certain asymmetry parameter η^o for the "perfect" crystal, together with the Laplace equation $V_{XX} + V_{YY} + V_{ZZ} = 0$, the corresponding $G_K(t)$ were calculated

by integrating over all possible V_{ii}'s :

$$\overline{G_K(t)} = \int\int G_K(V_{XX}, V_{YY}, t) \; P(V_{XX}) P(V_{YY}) dV_{XX} dV_{YY} \qquad (6.9)$$

These spectra were then least-squares fitted to equation 2.15 in order to determine the quantities ω_n, δ and η. Forker found that the derived η's differed considerably from the η^o values with which the model calculations were started, especially for η^o close to 0 or 1. As Forker explained, this is expected since η is restricted to the range $0 \leq \eta \leq 1$ and a distribution in η can never have an average of exactly 0 or 1. Thus, the most reliable data for the asymmetry parameter calculation are obtained when the distortions of the EFG by crystal lattice imperfections are small.

Concerning these two model calculations where either the ω_n or the EFG components are varied to account for a non-unique EFG at the site of the perturbed nucleus, the following should be noted (ZM73).

The assumption in the first model that the spread δ_n in the interaction frequencies ω_n are identical is equivalent to allowing for a distribution in the quadrupole interaction frequency ω_Q only. This can be seen by assuming a Gaussian distribution in ω_Q with a width $\lambda = \delta\omega_Q$.

This gives

$$\overline{G_k(t)} = a_{ko} + \sum_n a_{kn} \int \exp\left[-(\omega_Q - \omega_Q^o)^2/2\lambda^2\right] \cos(\omega_n t) d\omega_Q \qquad (6.10)$$

Now from equation 2.13, $\omega_n = \dot{\omega}_Q$ times a function of η, so

$$G_k(t) = a_{ko} + \sum_n a_{kn} \exp\left[-(\delta\omega_n t)^2/2\right] \cos \omega_n t \qquad (6.11)$$

which identical to equation 2.15 with $\delta_1 = \delta_2 = \delta_3 = \delta$.

The second model assumes a distribution in the EFG components. The deviation of the fitted η's from η^o in this model as found by Forker can be calculated directly from the distribution of EFG's by

$$\overline{\eta} = \int\int \eta(V_{XX}, V_{YY}) \, P(V_{XX}) \, P(V_{YY}) \, dV_{XX} \, dV_{YY} \qquad (6.12)$$

This integral was calculated numerically using the same η^o and $\Delta ZZ/V_{ZZ}$ values as Forker. Figure 6.4 shows the results which reproduce the least squares fitted values of Forker to within 20%. The $(\eta^o - \overline{\eta})$ difference is largest near an η^o of 0 or 1.

Since for a given field distribution, the average asymmetry parameter is given by $\overline{\eta}$ and not η^o, the average interaction frequencies should also be shifted. Calculation
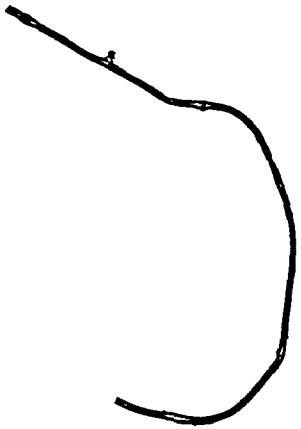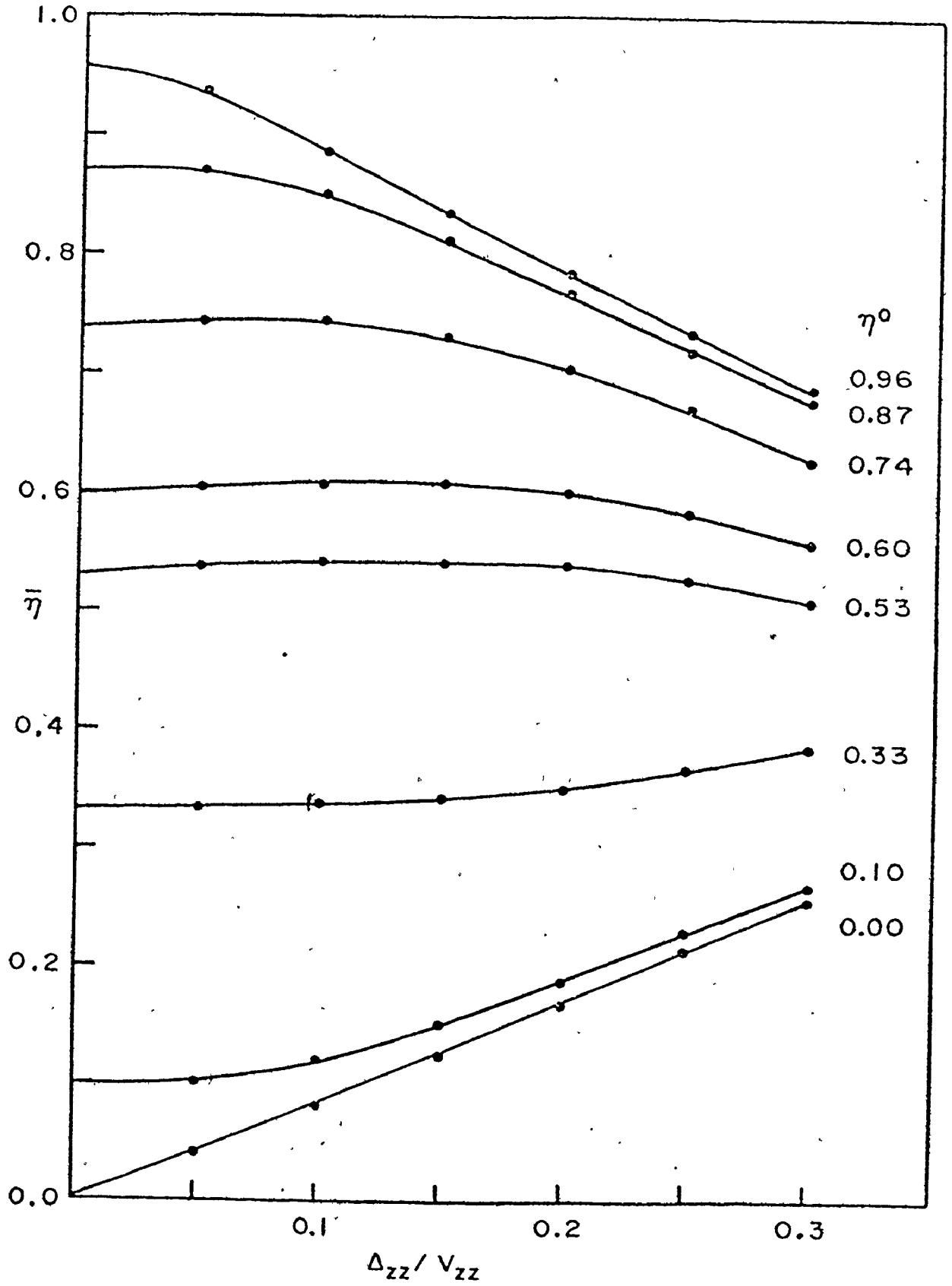
Figure 6.4

Plot of $\bar{\eta}$ Against Δ_{ZZ}/V_{ZZ}

for various initial values of η^O .

of these shifts from equation 2.13 reproduced the values
obtained by Forker.

In conclusion, while the first model assumes a
distribution of interaction frequencies which preserves
the asymmetry of the crystal (η remains unchanged), the
second model allows for an independent variation of the
EFG components with the only constraint given by the
Laplace equation.

Which of the two model calculations is closer to
a physical picture of the actual field distribution might
depend on the exact nature of the imperfections e.g. lattice
vacancies, impurities, radiation damage or incomplete crystal-
lization. If the observed field distribution is caused by
incomplete crystallization for instance then the measured
η which is derived from a fit to equation 2.15, rather than
η^O, will describe the actual asymmetry parameter of the sample.
On the other hand, impurities which occupy lattice sites and
do not distort the crystallographic structure will result in
a spatial distribution that is consistent with η^O but a
field distribution with an average η not equal to η^O.

The data in this thesis were analyzed according to
the conventional method by assuming either a Gaussian or
Lorentzian distribution of interaction frequencies (Table 2.1).

The significance of reported asymmetry parameters should be weighted by the above considerations.

5. Half-Life of the 48.2 keV Level of ^{181}Ta

   The data analysis via equation 6.1 often resulted in a half-life of the 482 keV level that was lower than the most recent result (BO71a) although in agreement within experimental error. Several previous measurements have been reported (Table 6.2) but only Bond et al. (BO71a) mention the significant contribution to the half-life uncertainty from the time calibration of the TAC and the nonlinearities of the measuring system and as a result they have quoted a larger error than the previous publications. Since a knowledge of the half-life is important for the correct analysis of DPAC measurements (section 6.1), a precise measurement of the half-life of the 482 keV level by the delayed coincidence method was performed (LO73).

   The electronic arrangement was similar to that described in chapter 3 for the 2 angle DPAC measurements but with only one pair of detectors in operation and no routing of the analyzer required. The spectrum was stored in 512 channels. The time resolution was 1.8ns (FWHM).

TABLE   6.2

Comparison of Half-Life Results

Half-life (ns)	Reference
11.0 ± 0.2	NA61
11.0 ± 0.1	MA63a
10.56± 0.15	ME65
11.0 ± 0.35	BO71a
10.81± 0.05	Present work

The source was produced by irradiating 2mg of HfI_4 for 1 MWh in the McMaster Reactor. HfI_4 was chosen because earlier attempts at a DPAC measurement of this sample did not produce any observable perturbations. The detectors, placed at 180°, were kept at a minimum separation ($\sim$ 5mm) to attenuate any possible angular perturbations. A shorter run at 90° was also recorded.

The effect of system nonlinearity was greatly reduced by correcting the data with the DNL curve of the system (section 4.3). This correction along with the accurate timescale calibration (section 3.5) and the large amount of data collected, greatly decreased the largest sources of error that may have influenced previous lifetime measurements.

Figure 6.5 is a plot of the data corrected by the DNL curve before and after background subtraction for a 3 day run with the detectors at 180°. The calibration is 0.504ns/channel. The background was considered constant throughout the spectrum because of a large ($\sim$ 300) peak-to-background ratio at the maximum in the spectrum.

The presence of possible time dependent perturbations in the solid, HfI_4 which could affect the value of the calculated half-life was discounted by the consistency of a series of least squares fits to various separate regions of the data.

Figure 6.5

The Decay of the 482 keV Level of ^{181}Ta

before and after background subtraction. The calibration is 0.504ns/channel.
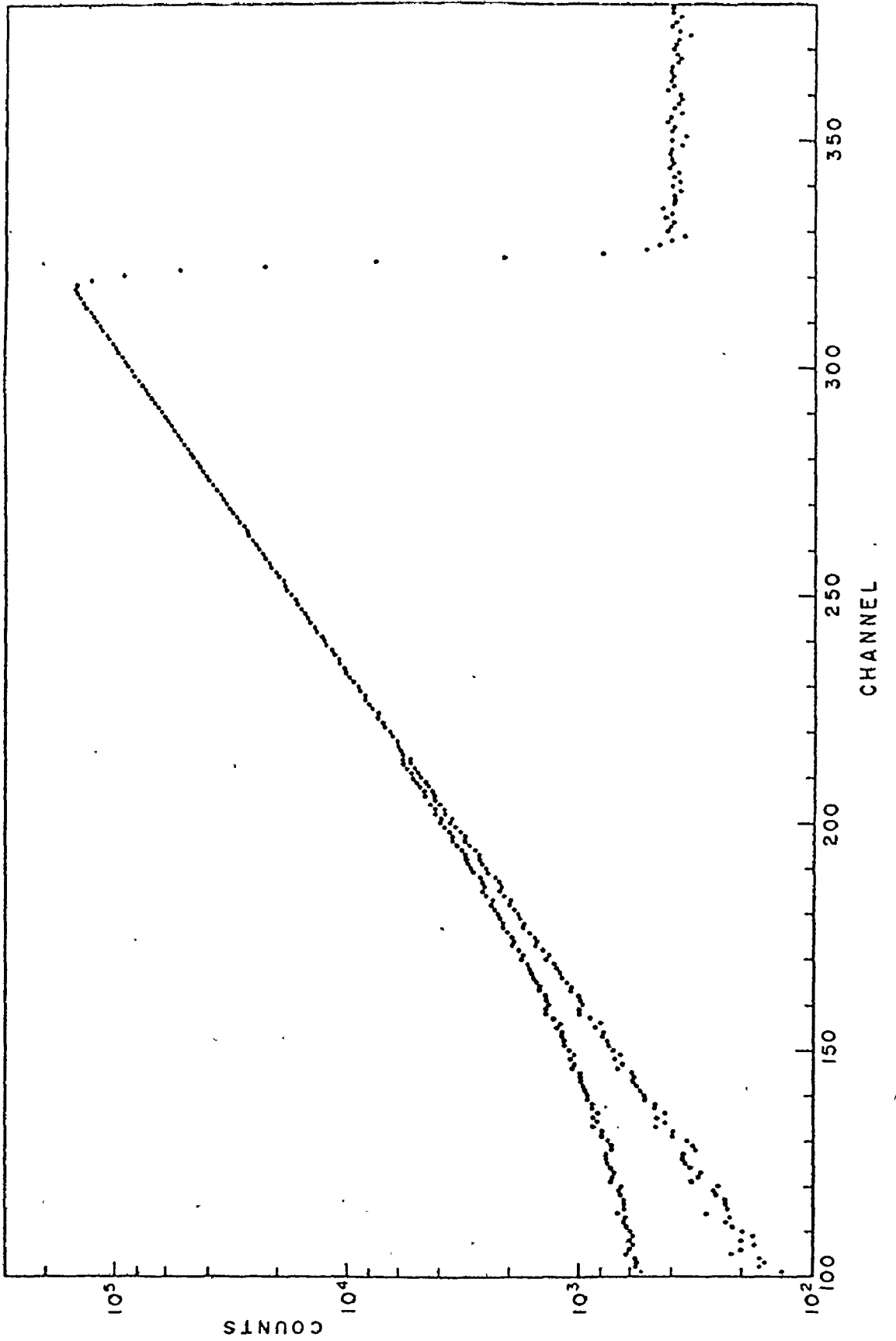
Angle dependent static perturbations were also ruled out by analysis of the one day run with the detectors at 90° which produced similar results.

The final fit to the corrected 180° data which extended over three decades gave a half-life of 10.809 ± 0.005ns where the quoted error is due to statistical analysis alone. Allowing for any possible systematic effects, the result for the half-life of the 482 keV level of ^{181}Ta is 10.81 ± 0.05ns.

CHAPTER 7

EXPERIMENTAL RESULTS AND DISCUSSION

1. ## The Heptafluorates

    A. ### Results

    (i) $(NH_4)_3HfF_7$

The calculated perturbation function for $(NH_4)_3HfF_7$ at liquid nitrogen temperature is shown in figure 7.1. This spectrum shows little oscillatory detail and rapid attenuation to a constant value with increasing time. This is indicative of a static EFG with a rather wide interaction frequency distribution. The fitted Gaussian frequency spread of 0.42 (Table 7.1) and the Fourier power spectrum of this function (figure 7.2) are in agreement. This result is somewhat expected from the suggested random orientation of the HfF_7^{3-} ions (HA38) on account of which the environment of the Hf atom is not unique. A measurement at liquid helium temperature yielded identical results within experimental error thus confirming the static nature of the EFG at these low temperatures.

Figure 7.3 shows the perturbation function at dry ice temperature. The static nature of the EFG is less apparent than at liquid nitrogen temperature and indeed, this function was equally well fitted to a pure static EFG with a very large

· 116

TABLE 7.1

Results for $(NH_4)_3HfF_7$

	-196°C		-78°C		21°C
Fundamental frequency ω_1 (Mrad/s)	207±7		120±8	123±8	–
Asymmetry parameter η	0.40±0.05 (0.39±0.02)*		0.41±0.06	0.45±0.06	–
Gaussian frequency spread δ	0.42±0.03 (0.39±0.01)*		0.64±0.08	0.45±0.06	–
Interaction frequency ω_Q (Mrad/s)	29.9 ±1.3 (34.95±0.90)*		17.1 ±1.3	17.1 ±1.3	–
V_{zz} (x10^{17}V/cm^2)	3.14±0.23 (3.62±0.18)*		1.80±0.17	1.80±0.17	–
Relaxation parameter λ (ns^{-1})	0		0	0.012±0.004	0.052±0.003

* From reference (GE73)

Figure 7.1

$A_2G_2(t)$ for $(NH_4)_3HfF_7$ at $-196^{\circ}C$

$(NH_4)_3 HfF_7$ $-196°C$
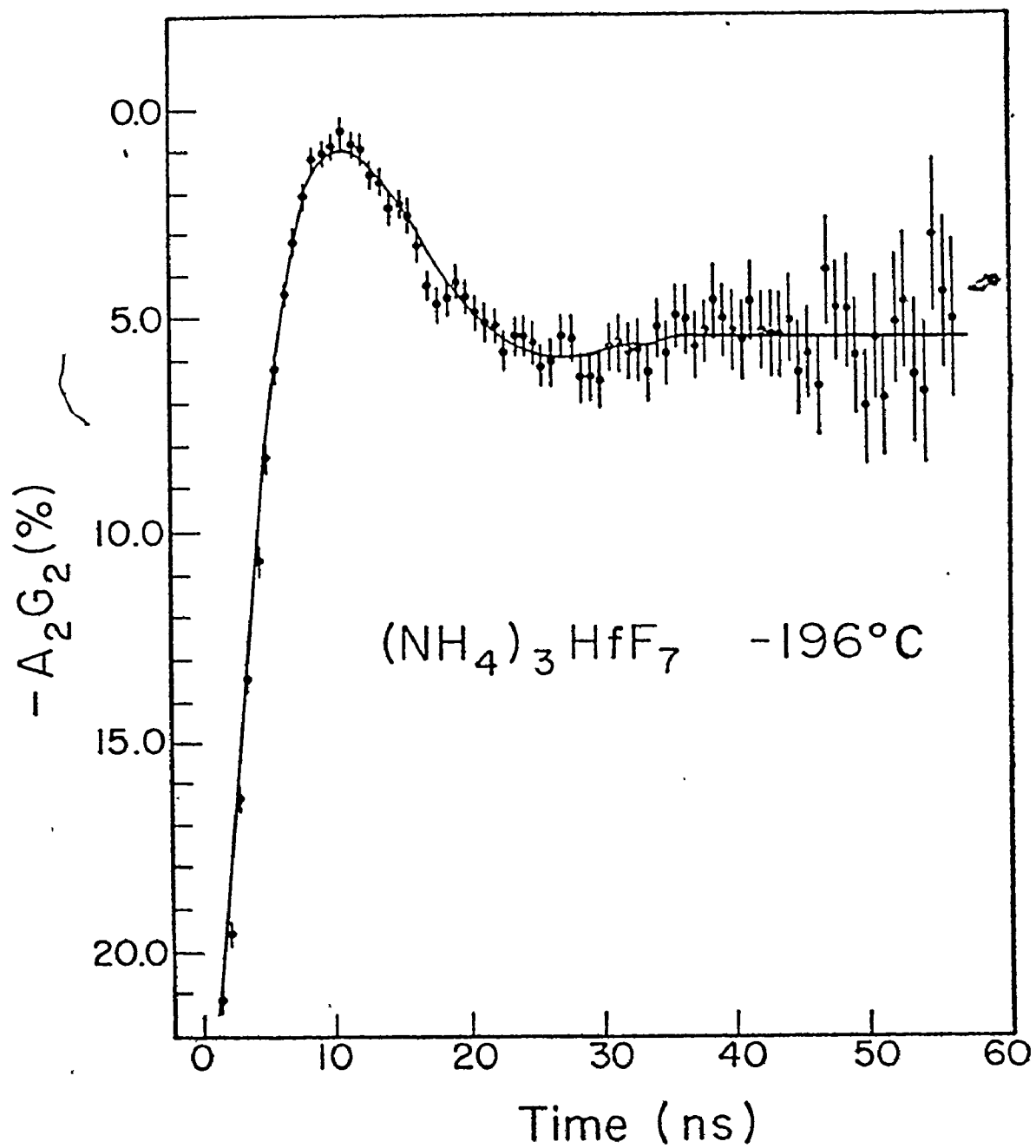
Figure 7.2

Fourier Power Spectrum for $(NH_4)_3HfF_7$ at $-196^{\circ}C$

of the perturbation function shown in figure 7.1 .

Figure 7.3

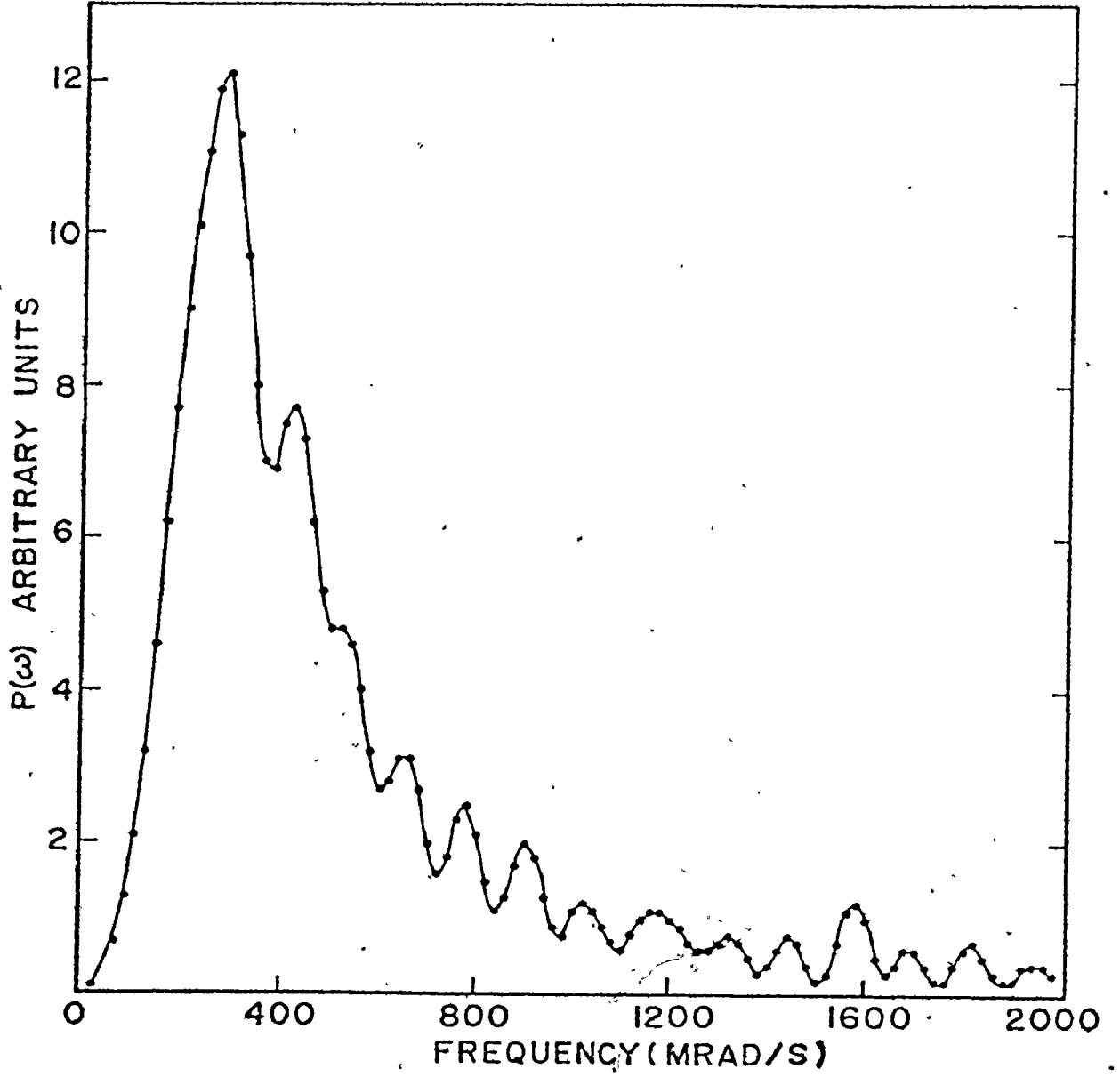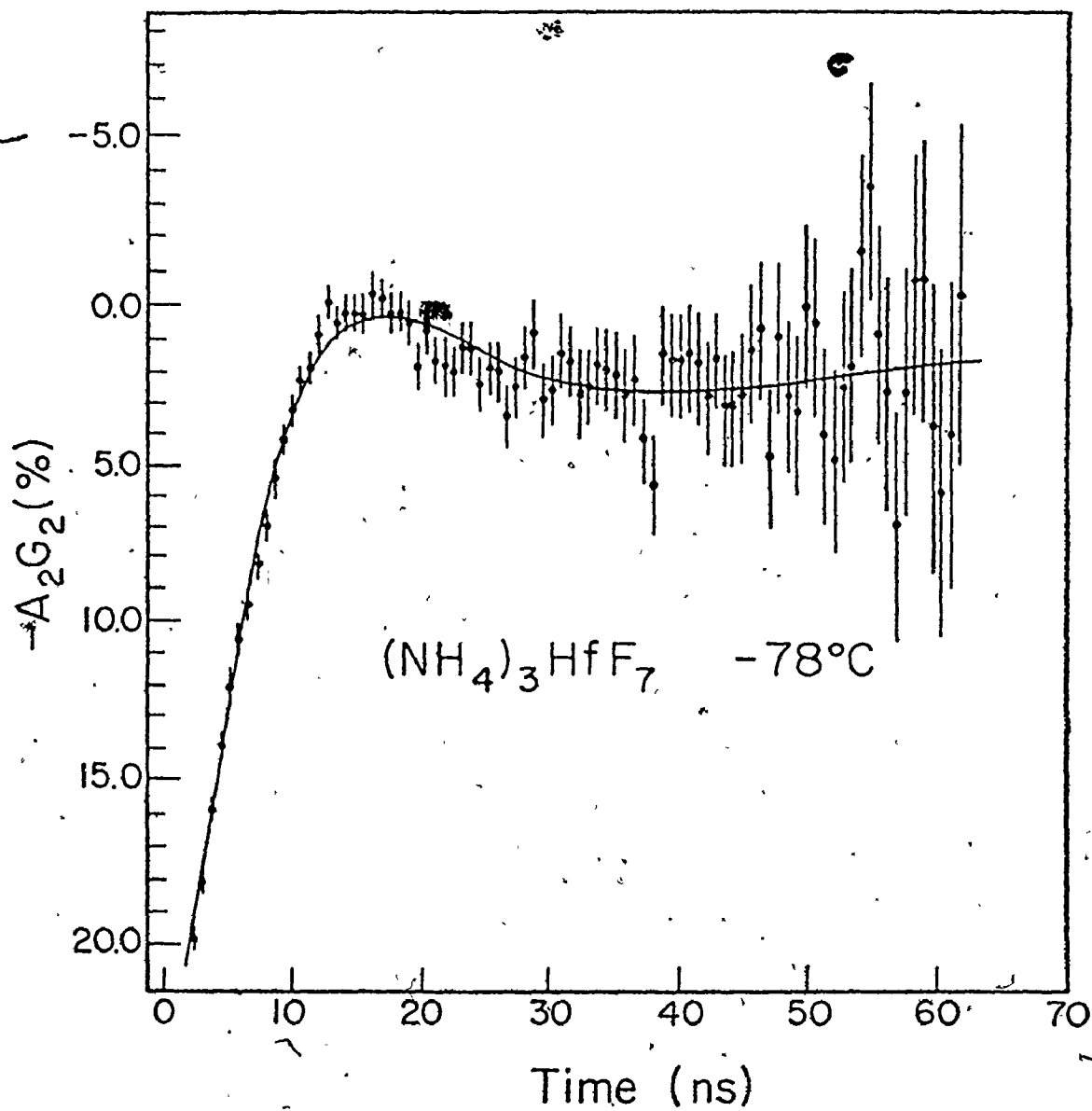$A_2G_2(t)$ for $(NH_4)_3HfF_7$ at $-78^{\circ}C$

$(NH_4)_3HfF_7$ $-78°C$

frequency distribution width of 0.64 or with a static FFG

modified by a time dependent exponential attenuation factor

of the form of equation 2.20. The results are given in

Table 7.1. This inability to firmly determine the exact

nature of the FFG is common in the presence of large

frequency distribution widths. In both fits, the fundamental

frequency ω_1 is much smaller than at liquid nitrogen temper-

ature.

Figure 7.4 shows the perturbation function at room

temperature plotted on a semi-log graph. This spectrum was

best fitted to a single-exponential decay which is indicative

of a pure time dependent relaxation process that is caused by

fast environmental fluctuations about the hafnium atom.

(ii) K_3HfF_7

The $A_2G_2(t)$ spectrum at liquid nitrogen temperature

for K_3HfF_7 (figure 7.5) contains more frequency detail than

the ammonium compound. The data could not be fitted to a one

site model under any conditions. Upon introduction of a second

site for the hafnium atom as modelled in equation 2.14, a good

fit shown by the solid line in figure 7.5 resulted. The results

are shown in Table 7.2. The population probability of the two

sites were found to be in the ratio of about 2 to 1. The EFG

characteristics as determined by the fundamental interaction

frequency and asymmetry parameter were found to be quite

Figure 7.4

$A_2G_2(t)$ for $(NH_4)_3HfF_7$ at $21^{\circ}C$

$(NH_4)_3HfF_7$ 21°C

$-A_2G_2(\%)$

TIME (ns)
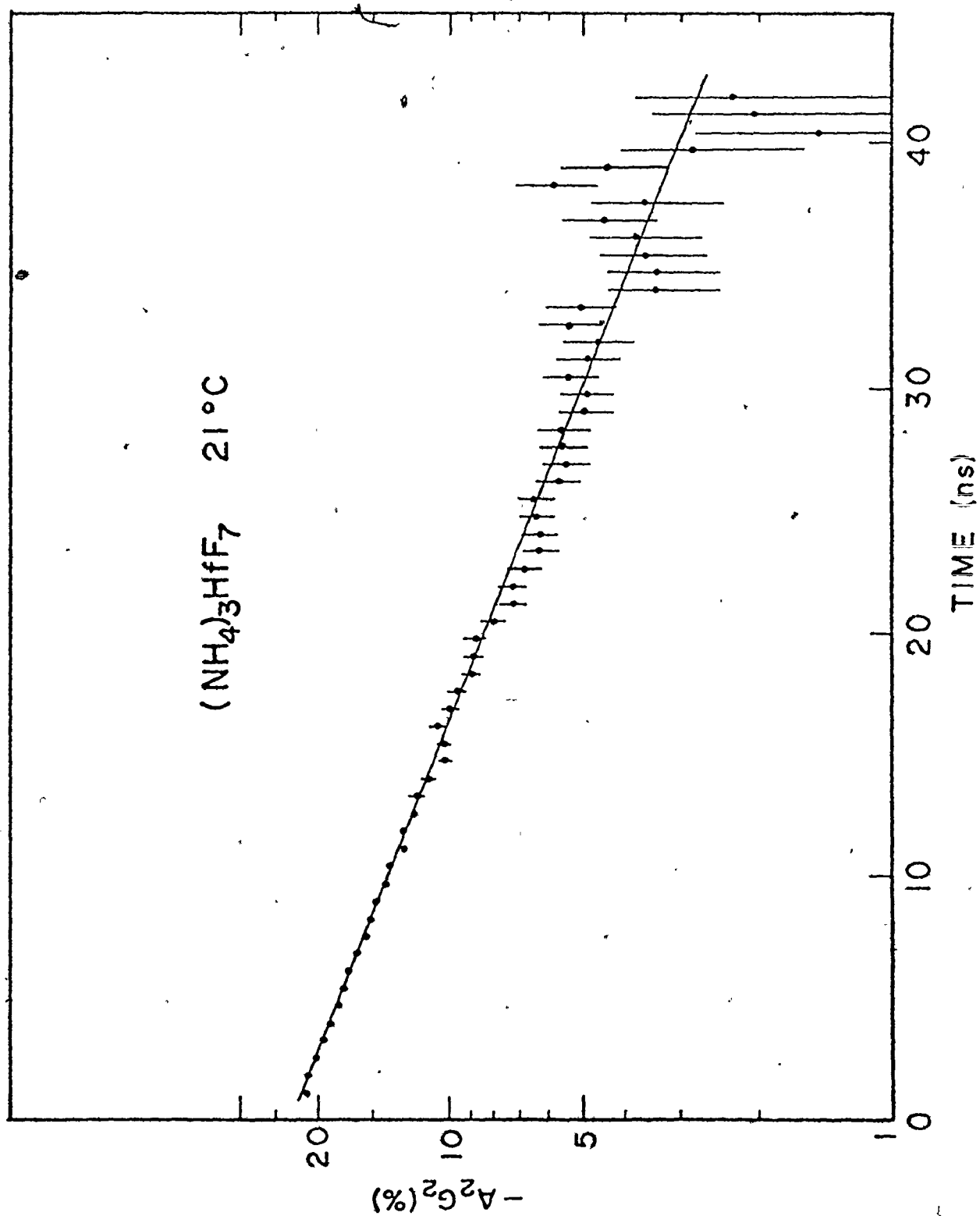
TABLE 7.2

Results for K_3HfF_7

	-196°C		0°C	21°C
	SITE 1	SITE 2		
Fundamental frequency ω_1 (Mrad/s)	416±8	780±20	289±6	281±7
symmetry parameter η	0.36±0.02	0.62±0.04	0.14±0.02	0.17±0.02
Gaussian frequency spread δ	0.13±0.02	0.06±0.02	0.13±0.02	0.12±0.02
interaction frequency ω_Q (Mrad/s)	61.2 ±1.4	96±4	47.2 ±1.0	45.4 ±1.2
ZZ ($\times 10^{17}$ V/cm^2)	6.4 ±0.4	10.1 ±0.7	5.0 ±0.3	4.8 ±0.3
Relaxation parameter λ (ns^{-1})	0	0	0.021 ±0.003	0.019±0.003
population probability	0.66±0.04	0.34±0.04	-	-

Figure 7.5

$A_2G_2(t)$ for K_3HfF_7 at $-196^{\circ}C$

K₃HfF₇ −196°C
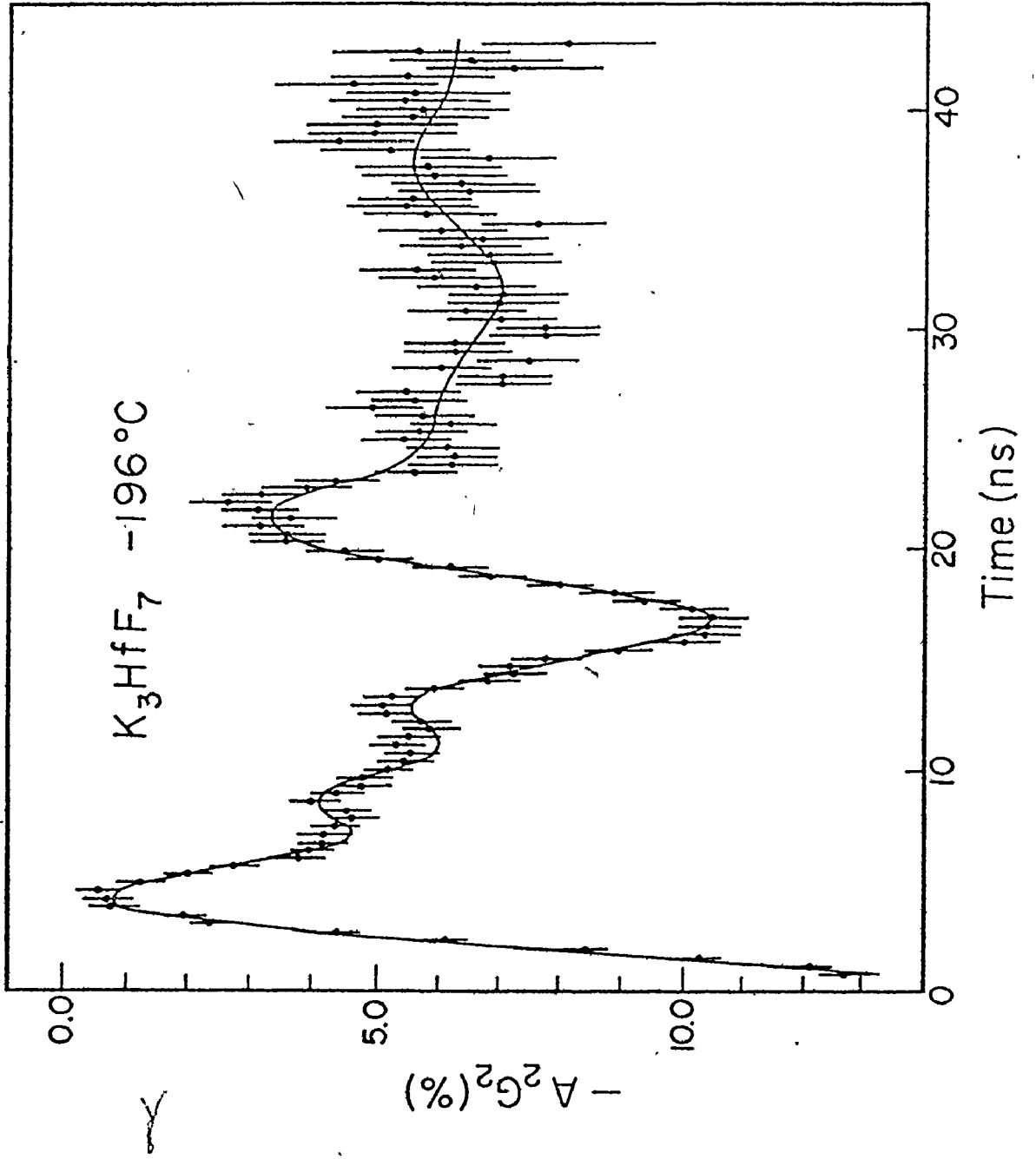
different for the two sites. The sites are also better

defined than the one site in the ammonium compound in that

they were fitted to Gaussian frequency distribution widths

of 13% and 6% as compared to 40% for $(NH_4)_3HfF_7$.

The measurement at room temperature (figure 7.6)

produced completely different results. This spectrum was

fitted to a static one site model multiplied by a small

exponential attenuation factor (Table 7.2) . The site

parameters differed from those of either of the two sites

found at liquid nitrogen temperature. A repeat of the liquid

nitrogen measurement reproduced the previous results thus con-

firming the stability of the sample throughout the experiments.

A measurement at $0^{\circ}C$ produced results that were similar to the

room temperature results within experimental error.

The change from a two site to a one site model is

further indicated by the power spectra of the perturbation

functions at these temperatures (Figure 7.7). The main peaks

correspond to the ω_1 fundamental frequencies of the sites as

calculated from the least squares fit analysis.

B. Discussion

The change in the environment of the ^{181}Ta probe nucleus

in $(NH_4)_3HfF_7$ from a static EFG to a time dependent one as the

temperature is increased is in direct contrast to the EFG in

Figure 7.6
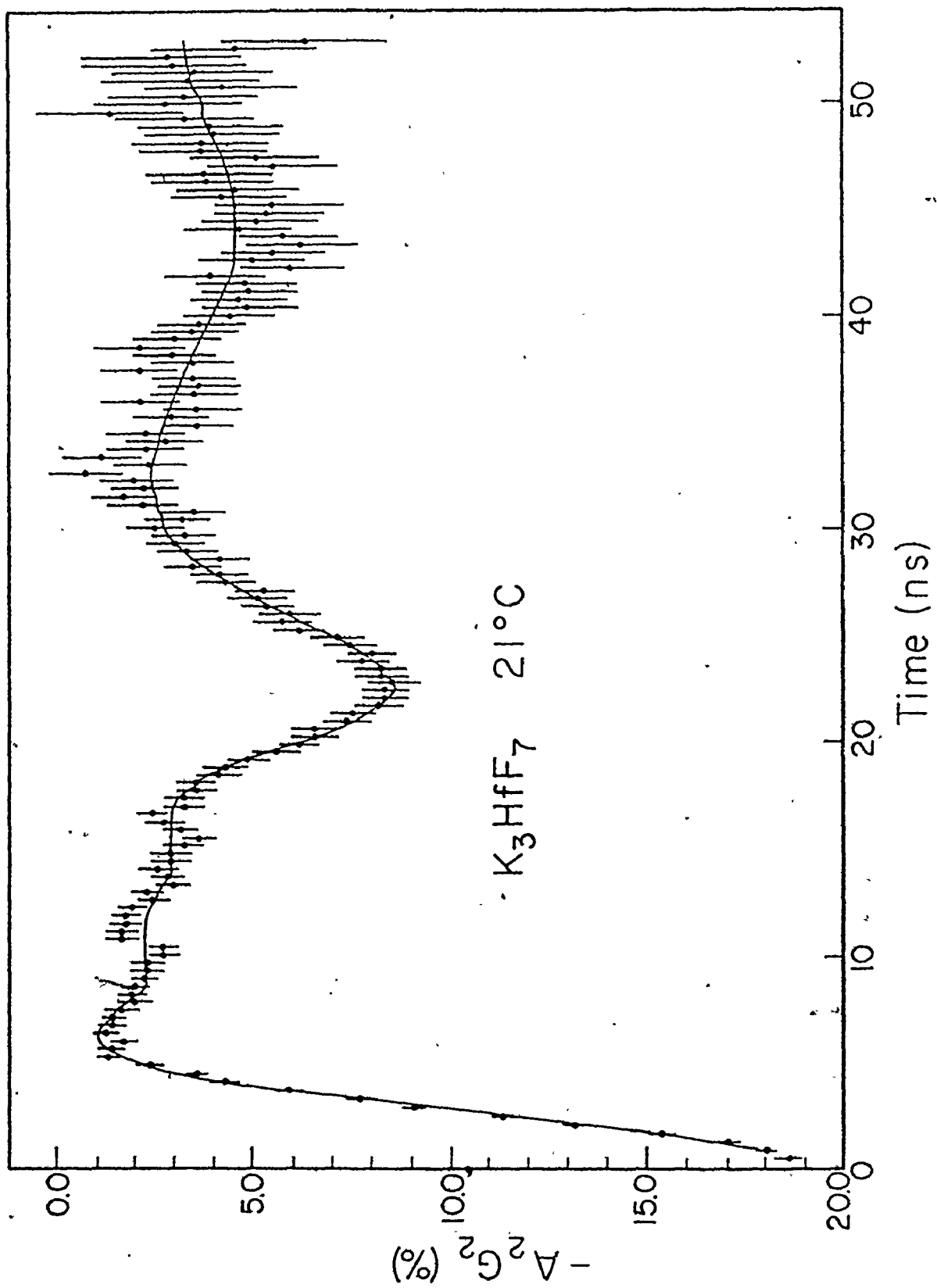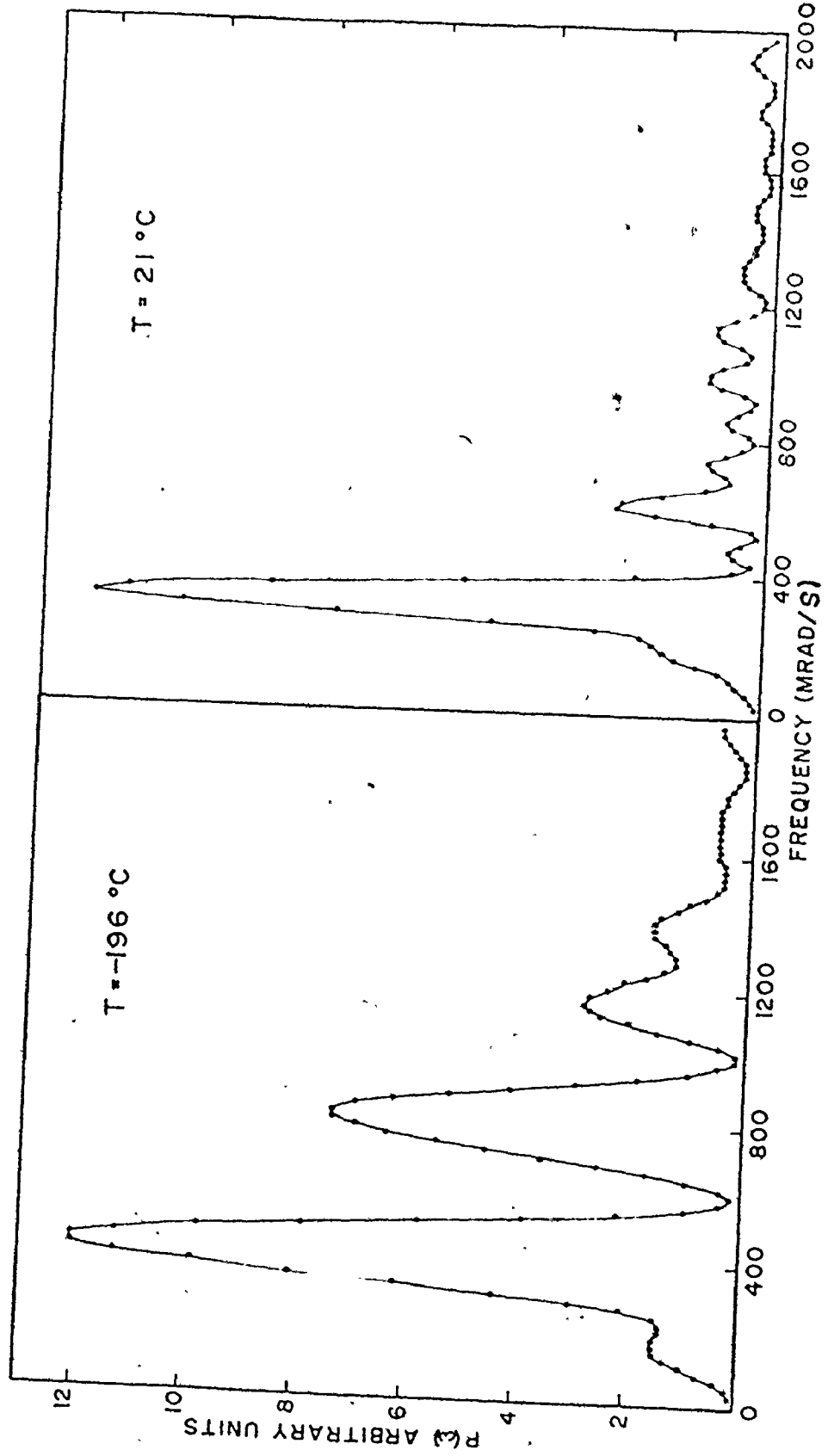
$A_2G_2(t)$ for K_3HfF_7 at $21^{\circ}C$

K₃HfF₇ 21°C

Figure 7.7

Fourier Power Spectra for K_3HfF_7

of the perturbation functions shown in figures 7.5 and 7.6 .

K_3HfF_7 which retains its static character up to as high as room temperature. The presence of the NH_4^+ ions obviously plays a large role in the dynamic nature of the HfF_7^{3-} ion.

The low temperature measurements on the ammonium compound are in general agreement with the results of Gerdau et al. (GE73) with only the quadrupole interaction frequency ω_Q being outside the experimental error overlap (Table 7.1). In light of the discussion of the calculation of DPAC parameters in the presence of large frequency distribution widths (section 6.4), the result for the asymmetry parameter should be considered as an average value. By using an EFG distribution width of $\dfrac{\Delta_{ZZ}}{V_{ZZ}} = 0.42$ as determined from the least squares fit , equations 6.8 and 6.12 give n = 0.34 which is close to the measured value of η = 0.40.

Gerdau et al. (GE73) saw a smooth transition from a static spectrum to pure exponential behaviour in the perturbation function above - 50°C. The present results show indications of a time dependent effect as low as - 78°C. These authors fitted their data by attributing this time dependence to rotations of the HfF_7^{3-} ion. .They visualized this as being due to the "jumping about" of the seventh fluorine atom around the faces of a six fluorine octahedron (figure 7.8). This model assumed the crystal structure of $(NH_4)_3HfF_7$ to be identical to that of

Figure 7.8

Possible Structures of the HfF_7^{3-} Ion

The octahedron + 1 model (A) was used by Gerdau et al. (GE73) in their analysis of $(NH_4)_3HfF_7$ while the pentagonal bipyramid (B) was suggested by Hurst and Taylor (HU70).

(A)

(B)

Hf^{4+} ●

F$^-$ ○
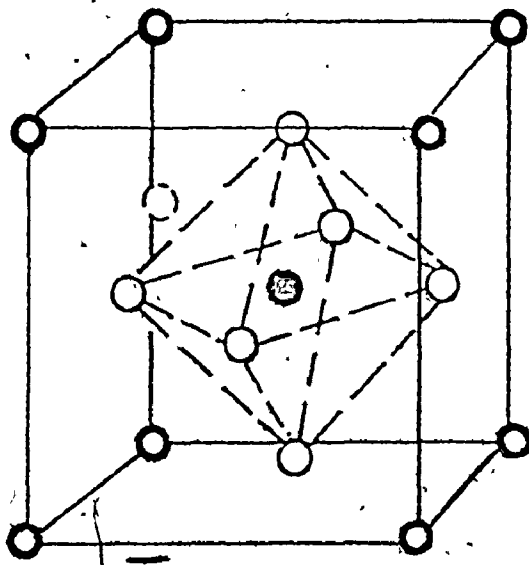
NH$_4^+$,K$^+$ ⭕

$(NH_4)_3A\ell F_6$ apart from the additional floating fluorine atom. The temperature dependence of this effect, considered to be an activation-like process, was found to be in agreement with NMR studies of the fluorine atoms. It should be noted that this model is in disagreement with X-ray s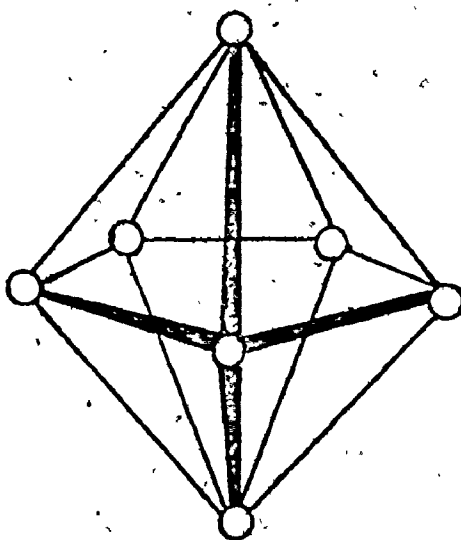tructure determination of Hurst and Taylor (HU70) who state that the ZrF_7^{3-} ion in $(NH_4)_3HfF_7$ is in the shape of a pentagonal bi-pyramid (figure 7.7) although slightly distorted.

The present study shows little evidence of a similar rotation of the HfF_7^{3-} ion in K_3HfF_7 over the same temperature range. The data were fitted to a static FFG even at room temperature at which only a small time dependent attenuation was required. The change from a two site to a one site environment for the Hf atom as the temperature is increased is in agreement with X-ray studies on K_3ZrF_7 by Buslaev et al. (BU71). They found a phase transition or structure transformation from a cubic lattice to an orthorhombic modification in going from room to liquid nitrogen temperature. Thus a one site to two site model change is possible over this temperature range. They also saw a similar phase transition in $(NH_4)_3ZrF_7$ but a two site model is not evident in the DPAC data at liquid nitrogen temperature. It is possible, however, for the two site model to remain undetected. For example, the two sites

could exhibit closely spaced interaction frequencies which, because of the frequency distribution widths, would overlap and would not be distinguished from a single broad interaction frequency.

The observed frequency spread of 0.12 at room temperature in K_3HfF_7 produces an average asymmetry of $\eta=0.10$ from an initial asymmetry of $\eta^o=o$ (figure 6.4). This accounts for a large fraction of the fitted value of $\eta=0.17$. This near symmetry is thus consistent with the D_{5h} symmetry of a pentagonal bipyramid which results in $\eta=o$ because of the equality of the X and Y axes in the pentagonal plane. The higher asymmetry values at liquid nitrogen temperature suggest a change from this D_{5h} symmetry.

The two site model for K_3HfF_7 can be compared to the NMR study of Tarasov and Buslaev (TA69) of the molecular motion and configuration of ZrF_7^{3-} in K_3ZrF_7. They explained the characteristics of their data by postulating that a decrease in temperature leads to a rearrangement of the lattice as a result of which the ZrF_7^{3-} ions occupy structurally nonequivalent positions. They estimated the population probability of the two groups to be in the ratio of 2 to 1 which is the same ratio as calculated from the present DPAC data.

These authors (TA69) found that one of the groupings of ZrF_7^{3-} ions was static and one was rotating. The DPAC data was fitted to two static sites. This apparent discrepancy can be understood if one considers the frequency of the perturbing interactions involved. As noted by Muetterties (MU65a), any comparison of structural data on nonrigid molecules must take into account the pertinent timescales of the measuring techniques. Should the timescale of the dynamics of a given molecule or ion be comparable to or longer than that of a laboratory observation, then the species under consideration must be considered static for the purposes of the experiment. Sharp et al. (SH70a), from NMR studies of fluorine in K_3ZrF_7, found that the correlation time governing the Zr-F ion orientation is given by

$$\tau_c = 7.1 \times 10^{-14} \exp (7700/RT)\,s$$

where R is the gas constant (1.98 cal mole^{-1} $^oK^{-1}$) and T is the absolute temperature. This gives

$$\tau_c \, (300\ ^oK) = 3 \times 10^{-8}\,s$$

This correlation time is comparable to the entire time range of the DPAC measurements ($\simeq$ 50ns) and thus the HfF_7^{3-} ion should be viewed as almost completely static under these

conditions. It is interesting to note that this correlation time is in rough agreement with the small relaxation parameter of $0.019ns^{-1}$ required to best fit the room temperature data since

$$\frac{1}{\tau_c} = 0.030ns^{-1} \ .$$

Mössbauer measurements (GE71) of the FFG at Hf sites in these heptafluorates have been performed. These give

$$\vec{V}_{ZZ} \text{ (in } (NH_4)_3HfF_7) = (7.2 \pm 0.3) \times 10^{17} \text{ V/cm}^2$$

$$V_{ZZ} \text{(in } K_3HfF_7) = (6.0 \pm 0.3) \times 10^{17} \text{ V/cm}^2$$

V_{ZZ} can be calculated from the DPAC experiments by using the ω_Q values and equation 2.7. This gives (Tables 7.1, 7.2).

$$V_{ZZ} \text{(in } (NH_4)_3HfF_7) = (3.1 \pm 0.2) \times 10^{17} \text{ V/cm}^2$$

$$V_{ZZ} \text{(in } K_3HfF_7) = (6.4 \pm 0.4) \times 10^{17} \text{ V/cm}^2 \quad \text{(site 1)}$$

$$= (10.1 \pm 0.7) \times 10^{17} \text{ V/cm}^2 \quad \text{(site 2)}$$

In comparing these results, it should be noted that the Mössbauer measurements are at Hf sites while the DPAC measurements are at Ta sites. This difference is theoretically accounted for by calculation of the Sternheimer antishielding factors. These factors measure the shielding (or enhancement)

of the EFG due to the polarization, caused by the lattice EFG, of the atomic shells of an atom or ion. However, these factors for Hf and Ta differ by only 10% (FF69) which is much smaller than the experimental differences (except for site 1 in K_3HfF_7). Similar comparisons of Mossbauer and DPAC data on $(NH_4)_3HfF_6$ (GE69) produce much better agreement. Any refined theoretical calculations of the EFG in the hepta-fluorates will have to consider these discrepancies.

The possible existence of different isomers in high coördination compounds is well known. For example, DPAC measurements on octocoordinated complexes of hafnium (BO72) have indicated the necessity of the two site model for the probe nucleus. The structure of compounds of coordination number 7 has been particularly confusing due to the lack of experimental data and the possibility of several competing shapes (MU67). Theoretical calculations have generally been based on 3 forms, one of which is the pentagonal bipyramid. The energy differences between these shapes in terms of which is most stable are quite small. Furthermore, since real compounds may exist only as distorted versions of these ideal-ized structures, the classification of such structures becomes somewhat difficult.

In summary, the heptafluorates $(NH_4)_3HfF_7$ and K_3HfF_7

which possess identical crystal structures (BU71) produce
vastly different EFG's at the site of the hafnium nucleus
as measured in the DPAC method. In particular, the dynamic
nature of the FFG in terms of the HfF_7^{3-} ion orientations
in $(NH_4)_3HfF_7$ is greatly influenced by the presence of
probable hydrogen bond effects from the reorienting NH_4^+
ions as no comparable dynamic effects are observed in K_3HfF_7.
Possibly this dynamic effect is due to the NH_4^+ ions alone
and not the reorientations of the HfF_7^{3-} ion. Studies of
these heptafluorates do present unique and difficult problems
but proper analysis of DPAC experiments can play a valuable
complementary role in the understanding of their nature.

2. Hafnium Acetylacetonate

A. Results

The calculated perturbation functions for both the
synthetic and commercial samples of Hf $(acac)_4$ are shown in
figure 6.2 (LO75). These exhibit strongly developed oscill-
ations, which for the sample synthesized after irradiation,
extend over seven cycles. For the commercial sample the
amplitude of the oscillations is significantly smaller but
the frequency is similar.

These data were best fitted to single site perturbation
functions with a Lorentzian distribution of interaction fre-
quencies. The results of the analysis are given in Table 7.3

TABLE 7.3

Results for $Hf(acac)_4$

	Synthetic sample (A)	Synthetic sample (B)
Fundamental frequency ω_1 (Mrad/s)	1085 ± 10	1084 ± 20
Asymmetry parameter η *	0.91 ± 0.05	1.00 ± 0.05
Lorentzian frequency spread δ	$0 \leq 0.02$	0.07 ± 0.02
Interaction frequency ω_Q (Mrad/s)	109 ± 4	102 ± 5
V_{zz} (10^{17} V/cm^2)	11.4 ± 1	10.7 ± 1

* The asymmetry parameter is constrained to have a maximum value of unity. The error quoted does not take this into account.

and the smooth curves in figure 6.2 are those which result using these parameters. Both the quadrupole interaction frequency and the asymmetry parameter are identical for both samples within the statistical uncertainty. In the limiting case of $\eta=1$, the two lowest frequency components ω_1 and ω_2 coalesce and this leads to a single component with the combined amplitude. The third component (from equation 2.13) is $\omega_3 = \omega_1 + \omega_2$ and in this limit would be twice the value of the fundamental component. This is in qualitative agreement with the observed power spectrum of the synthetic sample (figure 6.3) in which no field gradient distribution was indicated. The third component does not appear in the power spectrum of the commercial sample to which a best fit required a 7% spread in frequencies.

B. Discussion

The results indicate that both samples are characterized by the same average field gradient tensor, within experimental error. The only real difference is that the commercial sample exhibits a wider distribution in precession frequencies, which is consistent with the indication of poorer crystal quality in the X-ray results. Furthermore, there could be some radiation damage to this sample, the possibility of which will be discussed later.

According to Larsen (LA65), hafnium in the oxidation state four forms compounds which the central atom is surrounded by eight ligand bonds with either the square antiprism or dodecahedron arrangement. The former arrangement is shown in figure 7.9. In the acetylacetonate complex, the eight coordination bonds are provided by the 4 bidentate $CH_3COCHCOCH_3^-$ ligands and the bonding occurs at the oxygen sites. As discussed by Meutterties and Wright (MU65), there are 4 configurations to be expected for such octocoordinated hafnium complexes as shown in figure 7.10. In these diagrams, the oxygen sites are located at the corners and oxygen pairs common to a ligand are joined by a curved line.

The dodecahedral and square antiprism forms, with point group symmetries D_{2d} and D_4 respectively, are characterized by axially symmetric field gradients. Beraud et al. (BE69) incorrectly state that the D_{2d} symmetry requires a vanishing of the field gradient tensor and that D_2 symmetry requires $\eta=o$. In fact, D_{2d} requires $\eta=o$ while D_2 puts no restrictions on the value of η. A discussion of these symmetries is given in (LA58). The present results thus limit the possibilities to the square antiprismatic forms with D_2 and C_2 symmetry. In order to account for their results, Beraud et al. invoked the two site model based on the possible variation in configurations

Figure 7.9

Square Antiprismatic Structure of Hf(acac)$_4$

Figure 7.10
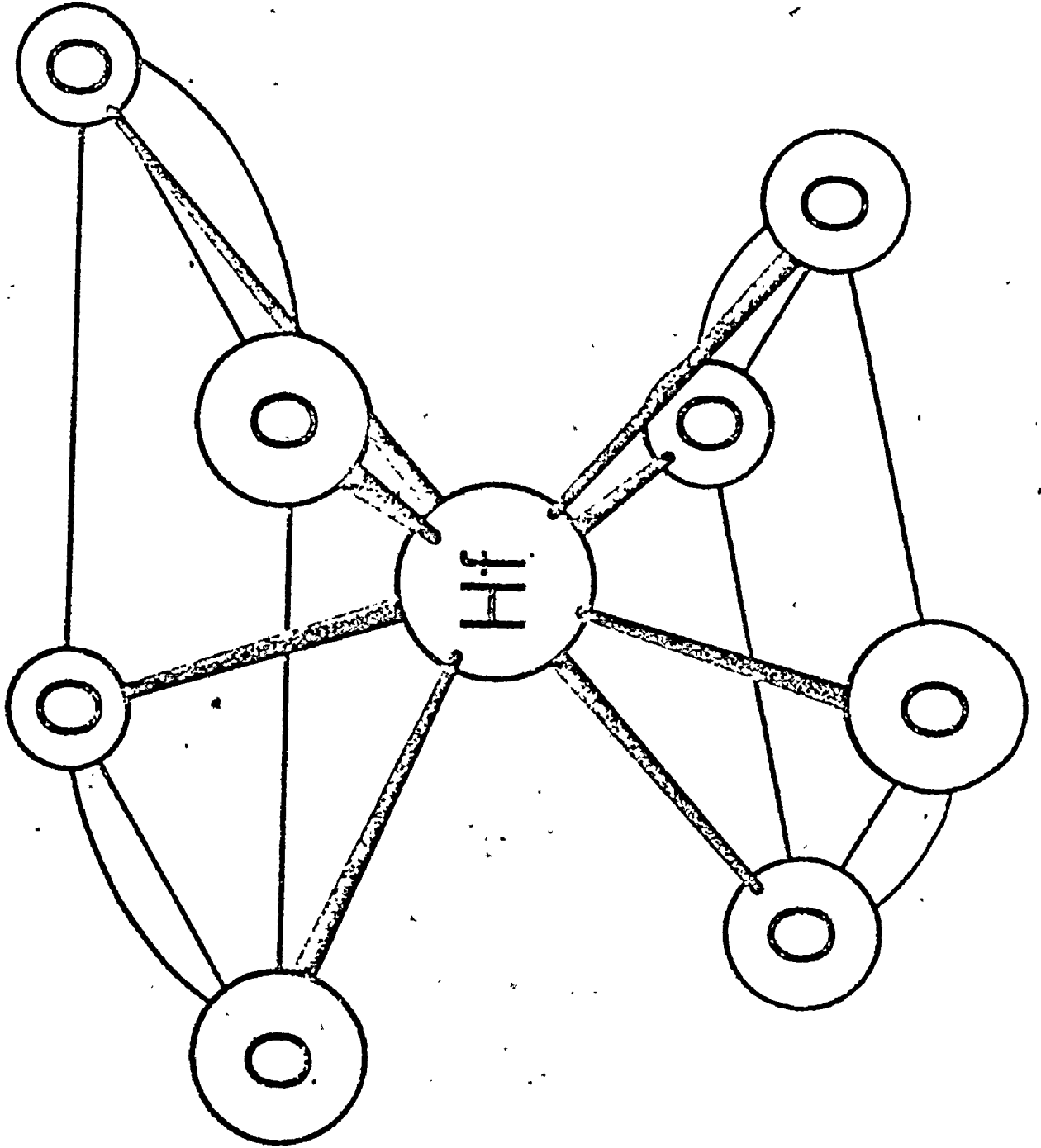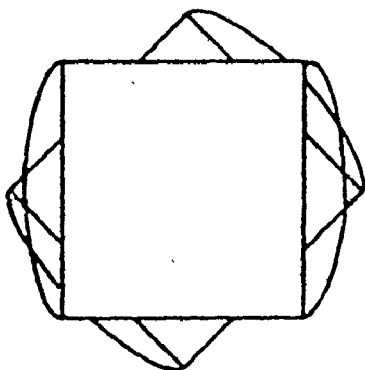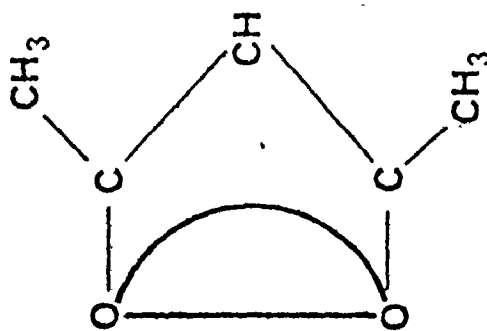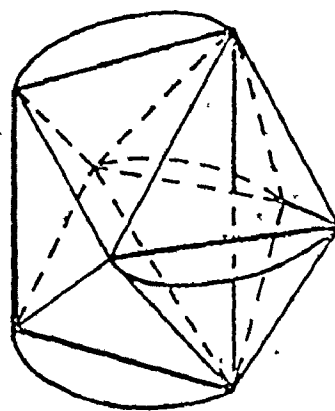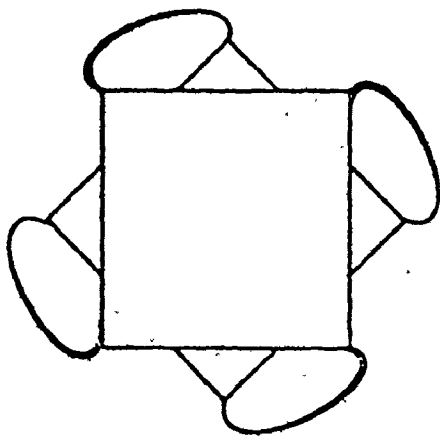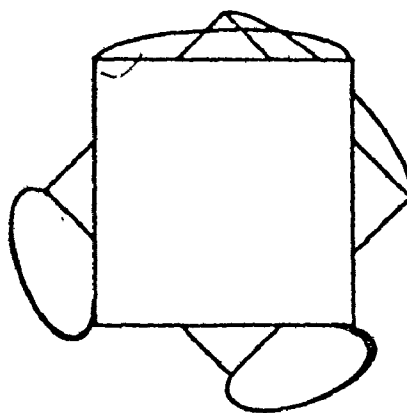
Possible Structures of an

Octocoordinated Hafnium Complex

D_2 square antiprism

D_{2d} dodecahedron

D_4 square antiprism

C_2 square antiprism

as discussed above. They assumed that the fundamental
frequencies of the two sites were identical because of
the similar frequency value measured by Vargas et al. (VA69)
for the $(BPH\Lambda)_4$ complex which presents a similar structure
for the hafnium atoms. This seems somewhat arbitrary since
the two sites are characterized by different asymmetry .
parameters. One site is near symmetry $\eta_1 = 0.1$ and the other
at maximum asymmetry $\eta_2 = 1$ and are populated with abundances
of 40% and 60% respectively. They apparently find a funda-
mental frequency that is some 30% lower than that observed
in this study. This comparison is somewhat uncertain however
since these authors state that $\omega_1 = 6\ \omega_Q$ which is incorrect
for $\eta \neq 0$.

The present data on both samples shows no evidence
for two sites of comparable contribution. Following the
method used to analyse the K_3HfF_7 data at liquid nitrogen
temperature, an attempt was made to fit the $Hf(acac)_4$ data
using a two site model but the best fit occurred when the
population of the second site was vanishingly small. This
is consistent with the observed Fourier spectrum which
indicates no contribution at other frequencies. This result
is also consistent with the X-ray structure analysis of

Silverton and Hoard (SI63) who definitively assign the D_2 square antiprismatic structure to this compound.

As noted earlier, there is the possibility of radiation damage to the irradiated commercial sample of Hf(acac)$_4$. After neutron capture in ^{180}Hf, 20% of the excited ^{181}Hf nuclei decay directly to the ground state by the emission of a 5.7 MeV γ-ray (AT74). This imparts a recoil energy of approximately 80 eV to the ^{181}Hf nucleus which is considerably larger than the approximately 25 eV displacement energy (SE56) of most solids. One would thus expect considerable damage to the crystalline structure. Such effects have been suggested to occur in the organic (BPHA)$_4$ hafnium complex by Vargas et al. (VA69) and also in Hf(acac)$_4$ by Beraud et al. (BE69). Both papers conclude that the (n,γ) recoil effect does not lead to a randomization of recoil sites but rather to the formation of different chemical species around the recoil nucleus.

The present results do not show to any significant degree any effects that can be directly attributed to radiation damage. The 7% frequency spread of the commercial sample, as compared to zero for the synthetic sample, might be a result of its initial poorer condition as indicated by the wider X-ray diffraction lines (chapter 5). This apparent lack of

radiation damage could stem from two reasons: too low a radiation dose and self-annealing. The commercial sample was irradiated for 2 h at a flux of 2.6×10^{12} n cm^{-2}s^{-1} as compared to 24 h at 4×10^{12} n cm^{-2}s^{-1} for the sample of Beraud et al. Secondly, they irradiated their sample at liquid nitrogen temperature whereas samples in the McMaster Nuclear Reactor reach typical temperatures of $\simeq 50^{\circ}$C. Since some effects have been observed which suggest that the damage recovery process is hastened by the irradiation itself (K155), irradiation at a low temperature might "freeze in" some damage. Furthermore, temperature plays a role in determining how long an interstitial atom and a vacancy, possibly produced by the irradiation, remain apart. The threshold energy for the migration of interstitials or vacancies is much lower than the approximately 25 eV required for the initial displacement (K155) and thus there is the possibility of self-annealing even at room temperature at which this experiment was performed. These effects would tend to reduce the overall radiation damage.

In conclusion, it is interesting to note that the result $\eta = 1$ shows that the EFG at the site of the hafnium nucleus is strongly anisotropic with one of the field gradient

components (V_{XX} or V_{YY}) vanishing completely. This is indicative of the ligand bonding in this octocoordinate complex since the immediate surroundings of the hafnium nucleus, formed by the square antiprismatic structure of the eight oxygen atoms, would not produce such a large anisotropy. This result represents a significant constraint which must be satisfied by any theories related to the molecular structure of the $Hf(acac)_4$ compound.

3. <u>Summary</u>

The quadrupole interaction of ^{181}Ta in the hepta-fluorates $(NH_4)_3HfF_7$ and K_3HfF_7 has been measured by means of the differential perturbed angular correlation technique. Although these compounds exhibit similar crystal structures, the electric field gradient at the site of the ^{181}Ta probe nucleus differs greatly in each compound. In particular, the dynamic nature of the EFG in the ammonium compound due to reorientations of the HfF_7^{3-} ion is not seen in the potassium compound over the same temperature range. The dynamics of the NH_4^+ ion obviously contributes much to this time-dependent effect. In addition, the hafnium atom in K_3HfF_7 can be situated in either of two sites at low temperatures with a

population probability ratio of 2 to 1 while the high temperature data indicate but one static site modified by a slight, time-dependent effect. These results are in agreement with other NMR and X-ray studies of these compounds.

The FFG at the metal site in hafnium acetylacetonate is quite dependent on the nature of the ligand bonding in this octocoordinated complex. The asymmetry of the FFG as determined from the DPAC measurements is indicative of the square antiprismatic structure of the environment of the hafnium atom. Evidence for the existence of two sites with different asymmetry parameters as suggested by a previous DPAC study was not found.

BIBLIOGRAPHY

AB53   A. Abragam and R.V. Pound, Phys. Rev. 92, 943 (1953)

AL64   K. Alder, R. Matthias, B. Olsen, W. Schneider and
        R.M. Steffen in Perturbed Angular Correlations (North
        Holland Publishing Co., Amsterdam, 1964), p. 247.

AN70   P. da R. Andrade, A. Vasquez, J.D. Rogers and E.R. Fraga,
        Phys. Rev. B1, 2912 (1970)

AS69   ASTM Powder Diffraction File (1969)

AT74   Atomic Data and Nuclear Data Tables 13, 262 (1974)

AV71   F.T. Avignonne III, J.H. Trueblood and Z.W. Grabowski,
        Nucl. Phys. A167, 129 (1971)

AZ58   L.V. Azaroff and M.J. Buerger, The Powder Method in X-Ray
        Crystallography (McGraw-Hill, New York, 1958) p. 49.

BA68   C.A. Baker, C.J. Batty and L.E. Williams, Nucl. Instr. and
        Meth. 59, 125 (1968)

BA79   H. Baker, J. Am. Chem. Soc. 35, 760 (1879)

BA74   R. Bauer, P. Limkilde and O. Glomset, Phys. Rev. Lett. 32,
        340 (1974)

BE60   R.E. Bell and M.H. Jorgensen, Can. J. Phys. 38, 652 (1960)

BE69   R. Beraud, I. Berkes, J. Daniere, G. Marest and R. Rougny,
        Nucl. Instr. and Meth. 69, 41 (1969)

BL67   W.W. Black and R.L. Heath, Nucl. Phys. A90, 650 (1967)

BL71   M. Blume, Nucl. Phys. A167, 81 (1971)

BO70   J.F. Boulter, W.V. Prestwich and T.J. Kennett, Nucl. Instr.
        and Meth. 77, 163 (1970)

BO71   J.F. Boulter, Ph.D. Thesis, McMaster University (1971)

BO71a   P.D. Bond, J.D. McGervey and S. Jha, Nucl. Phys. A163,
        571 (1971)

BO72   P. Boyer, A. Tissier, J.I. Vargas and P. Vulliet, Chem.
        Phys. Lett. 14, 601 (1972)

BU71   YU. A. Buslaev, V.I. Pachomov, V.P. Tarasov and
        V.N. Zege, Phys. Stat. Sol. b44, K13 (1971)

CO70   S. Cova and M. Bertolaccini, Nucl. Instr. and Meth. 77,
        269 (1970)

DA59   W.C. Davidon, A.E.C. Res. and Dev. Rep., ANL-5990
        (Rev.) (1959)

DI62   D. Dillenburg and Th. A.J. Maris, Nucl. Phys. 33, 208 (1962)

EV72   R.D. Evans, The Atomic Nucleus (McGraw-Hill, New York, 1972)
        p. 746.

FE69   F.D. Feoick and W.R. Johnson, Phys. Rev. 187, 39 (1969)

FL63   R.Fletcher and M.J.D. Powell, Comp. J. 6, 163 (1963)

FO73   M. Forker, Nucl. Instr. and Meth. 106, 121 (1973)

FR68   H. Frauenfelder and R.M. Steffen in Alpha-,Beta-, and
        Gamma-Ray Spectroscopy (North Holland Publishing Co.,
        Amsterdam, 1968) Chap. 19.

GA69   H. Gabriel, Phys. Rev. 181, 506 (1969)

GA69a   P. Gardner, Master Thesis, McMaster University (1969)

GE69   E. Gerdau, J. Wolf, H. Winkler and J. Braunsfurth, Proc.
        Roy. Soc. (London) A311, 197 (1969)

148

GE71   E. Gerdau, B. Scharnberg, and H. Winkler in

        Hyperfine Interactions in Excited Nuclei (Gordon and

        Breach, New York, 1971) p. 861.

GE73   F. Gerdau, J. Birke, H. Winkler, J. Braunsfurth,

        M. Forker and G. Netz, Z. Physik 263, 5 (1973)

GE75   E. Gerdau, private communication. (1975)

HA24   O. Hassel and H. Mark, Z. Physik 27, 89 (1924)

HA38   G. Hampson and L. Pauling, J. Am. Chem. Soc. 60, 2702

        (1938)

HA64   Harshaw Scintillation Phosphors (Harshaw Chemical Co.,

        Solon, Ohio, 1964) p. 11.

HO63   J.L. Hoard and J.V. Silverton, Inorg. Chem. 2, 235 (1963)

HU70   H.J. Hurst and J.C. Taylor, Acta Cryst. B26, 417 (1970)

IR66   J.L. Irigaray, J. Roturier and G.Y. Petit, Nucl. Instr.

        and Meth. 40, 221 (1966)

KI55   G. Kinchin and R. Pearse, Rep. on Prog. in Phys. 18, 21-

        (1955)

LA53   E.M. Larsen, G. Terry and J. Leddy, J. Am. Chem. Soc.

        75, 5107 (1953)

LA58   L.D. Landau and E.M. Lipshitz, Quantum Mechanics

        (Addison-Wesley Publishing Co., Reading, Mass. 1958)

        Chap. 12.

LA65   E.M. Larsen, _Transitional Elements_ (Benjamin Press, New York, 1965) p. 150.

LE68   C.M. Lederer, J.M. Hollander and I. Perlman, _Table of Isotopes_ (Wiley, New York, 1968)

LO72   L.M. Lowe, J.F. Poulter and W.V. Prestwich, Nucl. Instr. and Meth. $\underline{105}$, 461 (1972)

LO73   L.M. Lowe, H. Zmora and W.V. Prestwich, Can. J. Phys. $\underline{51}$, 1497 (1973)

LO75   L.M. Lowe, W.V. Prestwich and H. Zmora, Can. J. Phys. $\underline{53}$, 1327 (1975)

LY71   R.M. Lynden-Bell, Mol. Phys. $\underline{21}$, 891 (1971)

MA62   E. Matthias, W. Schneider and R.M. Steffen, Phys. Rev. $\underline{125}$, 261 (1962)

MA63   E. Matthias, W. Schneider and R.M. Steffen, Phys. Lett. $\underline{4}$, 41 (1963)

MA63a   E. Matthias, L. Bostrom, A. Maciel, M. Salomon and T. Lindqvist, Nucl. Phys. $\underline{40}$, 656 (1963)

MA71   M. Matoba, M. Hyakutake, H. Yamamoto and M. Sonoda, Nucl. Instr. and Meth. $\underline{94}$, 199 (1971)

MA72   A.G. Marshall and C.F. Meares, J. Chem. Phys. $\underline{56}$, 1226 (1972)

ME65   W. Meiling and F. Story, Nucl. Phys. $\underline{74}$, 113 (1965)

ME72   C.F. Meares and D.G. Westmoreland, Cold Spring Harbour Symp. Quant. Biol. $\underline{36}$, 511 (1972)

MU65   E.L. Meutterties and C.M. Wright, J.Am. Chem. Soc. 87, 4706 (1965)

MU65a   E.L. Meutterties, Inorg. Chem. 4, 769 (1965)

MU67   E.L. Meutterties and C.M. Wright, Quart. Rev. 21, 109 (1967)

NA61   T.D. Nainan, Phys. Rev. 123, 1751 (1961)

NE73   G. Netz and F. Bodenstedt, Nucl. Phys. A208, 503 (1973)

PI67   M. Pintar, G. Lahajnar and J. Slivnik, Mol. Phys. 12, 117 (1967)

RA75   R.L. Rasera and J.S. Vincent, Chem. Phys. Lett. 35, 95 (1975)

RO53   M.E. Rose, Phys. Rev. 91, 610 (1953)

SC68   H.J. Schuster, Nucl. Instr. and Meth. 63, 182 (1968)

SE56   F. Seitz and J. Koehler, Sol. S. Phys. 2, 305 (1956)

SH70   D.A. Shirley, J. Chem. Phys. 53, 465 (1970)

SH70a   A.R. Sharp, G. Lahajnar and M. Pintar, Phys. Stat. Sol. 37, 299 (1970)

SI63   J.V. Silverton and J.L. Hoard, Inorg. Chem. 2, 243 (1963)

TA69   V.P. Tarasov and YU.A.Buslaev, Zh. Strukt. Khim. 10, 816 (1969)

TH71   J.E. Thun in Angular Correlations in Nuclear Disintegration (Rotterdam University Press, The Netherlands, 1971) p. 78.

TU70   C.F. Turner, Nucl. Instr. and Meth. __87__, 45 (1970)

UH70   D.L. Uhrich, J.M. Wilson and W.A. Resch, Phys. Rev.
        Lett. __24__, 355 (1970)

VA69   J.I. Vargas, J. Berthier, J.C. Hocquengheim,
        J.J. Ribot and P. Boyer, Proc. Roy. Soc. (London) __A311__,
        191 (1969)

VA73   A. Vasquez, J.D. Rogers and A, Maciel, Phys. Lett.
        __45A__, 253 (1973)

WA69   H.F. Wagner and M. Forker, Nucl. Instr. and Meth. __69__,
        197 (1969)

WI73   H. Winkler and E. Gerdau, Z. Physik, __263__, 363 (1973)

YA65   M.J.L. Yates in Alpha-, Beta-, and Gamma-Ray Spectroscopy
        (North Holland Publishing Co., Amsterdam, 1965) p. 1691.

ZM73   H. Zmora, L.M. Lowe and W.V. Prestwich, Nucl. Instr. and
        Meth. __113__, 155 (1973)